Hamburg University of Applied Sciences

Faculty of Life Sciences

Master Thesis

Comparative analysis of UVA- and UVB-mediated DNA damage and repair in human dermal stem cells: Confocal imaging of skin biopsies

Vivien Rerich

Student ID: [redacted]

Supervisor: Prof. Dr. Julien Béthune (HAW Hamburg)
Supervisor: Dr. rer. nat. Beate Volkmer (Elbekliniken Stade-Buxtehude)

Department of Biotechnology

July 28, 2026

The master's thesis was carried out in collaboration with the Laboratory for Molecular Cell Biology at the Dermatological Centre of the Elbeklinikum Buxtehude under the supervision of Dr. rer. nat. Beate Volkmer and Dr. rer. nat. Mouna Mhamdi-Ghodbani.

Contents

List of Abbreviations v

List of Figures viii

List of Tables ix

1 Abstract 1

2 Introduction 2
2.1 Skin . . . 2
2.1.1 Keratinocytes . . . 3
2.1.2 Melanocytes . . . 3
2.1.3 Fibroblasts . . . 4
2.1.4 Stem Cells of the Skin . . . 5
2.1.4.1 Epidermal Stem Cells . . . 5
2.1.4.2 Dermal Stem Cells . . . 5
2.1.4.3 Dermal Stem Cell Markers . . . 6
2.2 UV Radiation . . . 6
2.2.1 UVB-induced DNA damage . . . 8
2.2.2 UVA-induced DNA damage . . . 8
2.2.3 DNA Repair . . . 9
2.3 Skincancer . . . 10
2.3.1 Non-Melanoma Skin Cancer . . . 10
2.3.2 Malignant Melanoma . . . 10
2.4 Aim of the Study . . . 11

3 Materials 13
3.1 Devices . . . 13
3.2 Consumables . . . 14
3.3 Chemicals and Reagents . . . 15
3.4 Buffers, Media and Solutions . . . 16
3.5 Antibodies . . . 17

4 Methods 18
4.1 Skin Preparation . . . 18
4.1.1 Foreskin Preparation . . . 18
4.1.2 Preparation of Adult Skin from Other Body Sites . . . 18
4.2 Irradiation . . . 18
4.3 Cryosectioning . . . 19
4.4 Immunofluorescence . . . 19
4.4.1 Staining of Different Cell-Type-Specific Proteins . . . 20
4.4.2 Staining of CPDs and NGFR p75 According to the DNase-I Protocol . . . 20

4.5 Microscopy 21
4.5.1 Fluorescence Microscopy 21
4.5.2 Confocal Microscopy 21

5 Results 23
5.1 Determination of the Specificity of the Secondary Antibodies 23
5.2 Evaluation of Markers for Identification Dermal Stem Cells and Dermal Structures . 24
5.2.1 Co-expression of SOX10 and NGFRp75 as a Marker Combination for Dermal Stem Cells 24
5.2.2 Co-expression of Nestin and NGFRp75 as a Marker Combination for Dermal Stem Cells 28
5.2.3 Assessment of βIII-Tubulin as a Neuronal Marker in NGFRp75-positive Dermal Stem Cells 31
5.3 Identification of Structures in the Dermis using Hematoxylin and Eosin Staining . . . 32
5.4 UV-induced DNA Damage in Different Skin Tissues 34
5.4.1 Assessment of Antibody Dilution Conditions 34
5.4.1.1 Reduction of False-Positive Signals 37
5.4.2 UV-induced DNA damage in NGFRp75-positive cells 38
5.4.2.1 UVA-induced DNA Damage 38
5.4.2.2 UVB-induced DNA Damage 43
5.4.2.3 DNA Damage Repair after 24 and 48 Hours 47

6 Discussion 55

Bibliography 61

Danksagung 66

Declaration on Oath / Eidesstaatliche Versicherung 67

List of Abbreviations

Abbreviation	Meaning
(6-4)PP	Pyrimidine (6-4) pyrimidine photoproduct
8-oxo-dG	8-Oxo-7,8-dihydro-2'-deoxyguanosine
BCC	Basal cell carcinoma
BER	Base excision repair
BSA	Bovine serum albumin
C	Cytosine
c	speed of light
CD95	Cluster of differentiation 95
CD95l	CD95-ligand
CPD	Cyclobutane pyrimidine dimer
DAPI	4',6-Diamidino-2-phenylindole
DDR	DNA damage response
DMEM	Dulbecco's Modified Eagle Medium
DNA	Deoxyribonucleic acid
DNase	Deoxyribonuclease
DSC	Dermal stem cell
E	Photon energy
ECM	Extracellular matrix
EpSC	Epidermal stem cell
FASl	FAS-ligand
FCS	Fetal calf serum
g	Gramm
G	Guanine
GGR	Global genome repair
h	Hour
h	Planck constant
H	Dose/ radiant exposure
HEPES	4-(2-Hydroxyethyl)-1-piperazineethansulfonic acid
HOX	Homeobox
I	Irradiance
IgG	Immunoglobulin G
J	Joule
λ	Wavelength
L	Litre
m	Meter

Abbreviation	Meaning
M	Molar, mol/L
MED	Minimal erythema dose
min	Minute
MM	Malignant melanoma
MMR	Mismatch repair
MSC	Mesenchymal stem cell
NER	Nucleotide excision repair
NGFRp75	p75 nerve growth factor receptor
NMSC	Non-melanoma skin cancer
PBS	Phosphate-buffered saline
PDGF	Platelet-derived growth factor
Pen/Strep	Penicillin – Streptomycin
PFA	Paraformaldehyde
ROS	Reactive oxygen species
s	second
SCC	Squamous cell carcinoma
SKP	Skin-derived precursor
SOX10	Sex determining region Y-box 10
t	Exposure time
T	Thymine
TAC	Transit-amplifying cell
TCR	Transcription-coupled repair
TGF-β	Transforming growth factor-β
Tris	Tris-(hydroxymethyl)-aminomethan
UV	Ultraviolet radiation (100 – 400 nm)
UVA	Ultraviolet A radiation (315 – 400 nm)
UVB	Ultraviolet B radiation (280 – 315 nm)
UVC	Ultraviolet C radiation (100 – 280 nm)
VH	Vorhaut (engl.: foreskin)
W	Watt
WNT	Wingless-related integration site

List of Figures

1 Anatomy of the skin. 2
2 Theories of melanoma development and the influence of UV radiation. 11

3 Secondary antibody staining control. 23
4 Dermal stem cell culture shows SOX10/NGFRp75 double-positive cells. 24
5 Axillary skin sections stained for SOX10 and NGFRp75, showing SOX10/NGFRp75 double-positive cells. 25
6 Juvenile foreskin sections stained for SOX10 and NGFRp75, showing SOX10/NGFRp75 double-positive cells. 26
7 Juvenile foreskin sections stained for SOX10 and NGFRp75. Images of the dermis. . 27
8 Dermal stem cell culture stained for Nestin and NGFRp75, showing co-expression of Nestin and NGFRp75 in all cells. 28
9 Juvenile foreskin section shows widespread Nestin expression and NGFRp75 staining. 30
10 Dermal stem cell culture stained for βIII-Tubulin and NGFRp75, showing co-expression of both markers in all cells. 31
11 Juvenile foreskin sections stained for βIII-Tubulin and NGFRp75, showing double-positive cells and βIII-Tubulin-positive cells. 32
12 H&E-staining of different skin biopsies showing eccrine sweat glands. 33
13 H&E-staining of skin biopsies showing various structures in the dermis. 33
14 Non-irradiated control samples stained with different CPD antibody dilutions, showing no background signal. 35
15 UVB-irradiated skin stained with different CPD antibody dilutions. 36
16 False-positive signals with the DNase-I treatment staining. 37
17 Optimization of the initial CPD and NGFRp75 staining protocol revealed no false-positive staining. 38
18 Axillary skin sections stained for CPD and NGFRp75 after 0 J/m^2 (control) and 140 kJ/m^2 UVA irradiation. 40
19 Thigh skin sections stained for CPDs and NGFRp75 after 0 J/m^2 (control) and 140 kJ/m^2 UVA irradiation. 41
20 Juvenile foreskin sections stained for CPDs and NGFRp75 after 0 J/m^2 (control) and 140 kJ/m^2 UVA irradiation. 42
21 Axillary skin sections stained for CPDs and NGFRp75 after 0 J/m^2 (control) and 1500 J/m^2 UVB irradiation. 44
22 Thigh skin sections stained for CPDs and NGFRp75 after 0 J/m^2 (control) and 1500 J/m^2 UVB irradiation. 45
23 Juvenile foreskin sections stained for CPDs and NGFRp75 after 0 J/m^2 (control) and 1500 J/m^2 UVB irradiation. 46
24 Axillary skin sections stained for CPDs and NGFRp75 at time points T0, T24, and T48 after UVA and UVB irradiation. 49

25 Thigh skin sections stained for CPDs and NGFRp75 at time points T0, T24, and T48 after UVA and UVB irradiation. 51
26 Foreskin sections stained for CPDs and NGFRp75 at time points T0 and T24 after UVA and UVB irradiation. 53

List of Tables

1 Devices and equipment used in the experiment setup. 13
2 Consumables used in the study. 14
3 Chemicals and reagents used in this study. 15
4 Buffers, media and solutions used in the study. 16
5 Primary antibodies used in the study. 17
6 Secondary antibodies used in the study. 17
7 Overview of the applied UV doses. 19

1 Abstract

Ultraviolet (UV) radiation from the sun is a major risk factor for skin cancer, including the malignant melanoma (MM). UVA and UVB radiation both reach the Earth's surface and are therefore of considerable biological relevance. They penetrate human skin to different depths and induce DNA damage. This thesis investigates UV-induced DNA damage in the form of cyclobutane pyrimidine dimers (CPDs) in human skin biopsies. Skin samples obtained from the thigh, axilla, and juvenile foreskin were irradiated with 140 kJ/m^2 UVA or 1500 J/m^2 UVB and analyzed immediately after irradiation as well as 24 and 48 hours later to assess CPD repair kinetics. The study focused on dermal stem cells (DSCs), which have been discussed as potential cells of origin for MM. Skin sections from all samples were analyzed by immunofluorescence staining following DNase-I digestion. CPDs were detected using the anti-CPD antibody TDM2, while the neural crest marker NGFRp75 was used to identify DSCs. In addition, SOX10, Nestin, and βIII-Tubulin were evaluated as potential DSC markers. Image acquisition was performed using confocal laser scanning microscopy. The results demonstrate that NGFRp75 was the most suitable marker for identifying DSCs in human skin sections in this study. Both UVA and UVB radiation efficiently induced CPDs in skin cells. UVB-irradiation also induced CPDs in NGFRp75-positive cells, which remained detectable for up to 48 hours. These findings suggest that although UVA-radiation represents a substantial risk to DSCs because of its longer wavelength and deeper tissue penetration, UVB can induce persistent DNA damage in dermal NGFRp75-positive cells and may thereby contribute to mutational events involved in MM development.

2 Introduction

2.1 Skin

The skin, with a surface area of 1.6 – 2 m^2, is the largest organ of the human body [1]. It is the first barrier between the organism and the environment and is therefore constantly exposed to various external influences, including temperature, pollutants, microorganisms, and solar radiation [2]. The primary function of this organ is to protect the body against diverse environmental stressors. In addition, the skin plays a crucial role in the regulation of body temperature [3]. Human skin consists of a multilayered structure that differ in morphology and functions. It can be divided into three main layers. The outermost layer is the epidermis, followed by the dermis and, finally, the subcutaneous tissue (subcutis) (Figure 1).

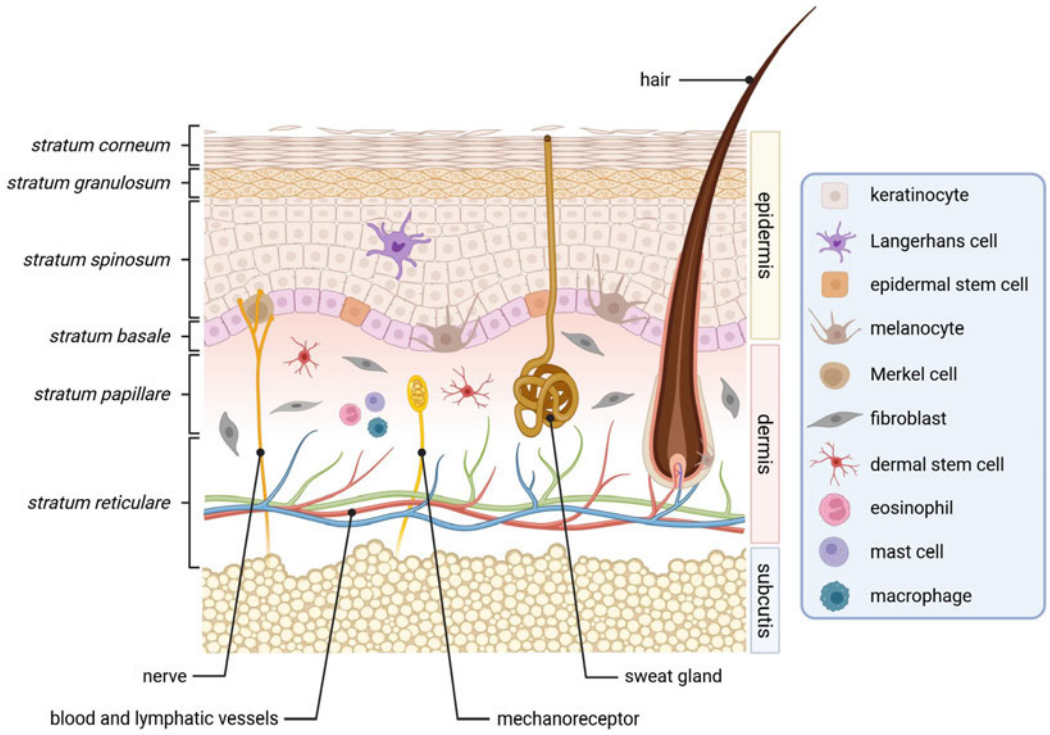


Figure 1. Anatomy of the skin. Cross-sectional illustration of human skin showing the epidermis, dermis, and subcutis, as well as the major cell types and anatomical structures, including hair follicles, sweat glands, blood and lymphatic vessels, nerves, and sensory receptors. Created with BioRender by Christin Starzonek.

The epidermis itself is made up of several layers. It mainly consists of keratinocytes, which determine the structural organization of the epidermis. These cells are connected through various types of cell junctions that are responsible for mechanical adhesion, biochemical communication, and signaling interactions between neighboring cells. Keratinocytes make up more than 90% of epidermal cells, whereas melanocytes, Merkel cells, and Langerhans cells together account for approximately 10% throughout the epidermis. The epidermis itself does not contain any blood vessels and is therefore supplied by the underlying dermis. In contrast to the epidermis, the dermis contains numerous blood and lymphatic vessels [1]. Furthermore, the abundance of collagen and elastic fibers in the dermis makes it a highly elastic and mechanically resistant tissue. The dermal projections extending

into the epidermis, known as the dermal papillae, contribute to the stability of the skin and increase the exchange of nutrients between the dermis and epidermis. This upper region of the dermis is referred to as the papillary dermis. It is characterized by a relatively loose fiber structure, whereas the underlying reticular dermis contains a denser and more organized extracellular fiber network [4]. This dense extracellular matrix is primarily synthesized by fibroblasts located within the dermis and provides the structural environment for various additional components, including nerve fibers, bundles of smooth muscle cells, sebaceous and sweat glands, hair follicles, and various other cells (Figure 1). The deepest layer of the skin is the subcutis, which consists mainly of adipose tissue and loose connective tissue. The predominant cells within this layer are the adipocytes [1]. These cells function as cushioning structures and energy storage units. The primary function of the subcutis is the maintenance of the body temperature through thermal insulation [5].

2.1.1 Keratinocytes

Keratinocytes are the predominant cell population of the multilayered epidermis, accounting for more than 90% of all epidermal cells [4]. They originate from stem cells located in the deepest layer of the epidermis, the basal layer (stratum basale), and undergo a process of differentiation and keratinization as they migrate towards the skin surface. During this process, keratinocytes form a stable structural network by producing keratin filaments and forming cell-cell junctions, which provide the skin with mechanical strength. The terminally differentiated and dead corneocytes within the outermost layer, the stratum corneum, ultimately form the primary protective and water-retaining barrier of the epidermis. At this step, the nucleus-free and fully keratinized keratinocytes are shed from the skin surface. The complete process of keratinocyte maturation and turnover takes approximately four weeks [4, 6]. In addition to their central role in maintaining the skin barrier, keratinocytes are involved in functional interactions with other epidermal cell types. Particularly, their interaction with melanocytes plays a crucial role in protecting the skin against ultraviolet (UV) radiation. UV radiation induces the expression of proteins in keratinocytes that stimulate melanin production and contribute to the regulation of pigmentation responses. On average, a single melanocyte supplies approximately 30 – 40 keratinocytes with melanin [7]. This functional unit between melanocytes and keratinocytes is referred to as the epidermal melanin unit [4, 8]. Keratinocytes represent the predominantly affected cell population upon UV exposure and can contribute to the development of epithelial skin tumors through the accumulation of insufficiently repaired UV-induced DNA damage [8].

2.1.2 Melanocytes

Within the skin, melanocytes are primarily located in the basal layer of the epidermis where they are evenly distributed among keratinocytes. The average ratio of melanocyte to keratinocyte in the basal layer is reported to be 1:7, although it varies between different anatomical sites [9]. They originate from the neural crest and are found not only in the skin but also in hair follicles, the iris, and several other tissues throughout the body [10]. Their primary function is the synthesis of melanin, which is responsible for skin pigmentation. Melanin fulfills several important functions. It covers the cell nuclei of the keratinocytes, thereby effectively reducing the penetration of UV radiation and protecting DNA from UV-induced damage. In addition, melanin has antioxidant properties as it neutralizes reactive oxygen species (ROS) and other free radicals within the skin. The dendritic processes of

melanocytes remain in close contact with neighboring keratinocytes. Consequently, although keratinocytes are unable to synthesize melanin themselves, they contain large amounts of melanin. This transfer is mediated by melanin-containing organelles known as melanosomes [4, 8]. Melanosomes contain a mixture of different types of melanin. The two major forms are eumelanin and pheomelanin. Eumelanin is responsible for brown to black pigmentation, whereas pheomelanin produces yellow to reddish pigmentation. The synthesis of these two melanin types depends on the available precursor molecules as well as the activity of the enzymes involved in melanin production. Compared with pheomelanin, eumelanin provides significantly greater protection against UV radiation. It is more resistant to degradation processes and more effective at neutralizing ROS [10]. In contrast, additionally to its lower photoprotective quality, it has been suggested that pheomelanin promotes the formation of ROS due to its pro-oxidative properties and the depletion of cellular antioxidants and thereby potentially contributing to the development of skin cancer [11, 12].

2.1.3 Fibroblasts

Fibroblasts are the predominant cells of the dermis. They are mesenchymal cells embedded within an extracellular matrix (ECM) that they synthesize themselves. The ECM consists mainly of collagen fibers, elastic fibers, and other components such as elastin, fibronectin, microfibrillar proteins and laminins. This ECM provides the skin with mechanical strength, elasticity, and tensile resistance, and thereby protecting it against external stresses [13, 14]. Fibroblasts typically show an elongated spindle-shaped morphology, whereas activated fibroblasts often adopt a stellate morphology [15]. The dermis contains various fibroblast subpopulations that are capable of actively remodel the ECM. Depending on their anatomical location, fibroblasts synthesize region-specific ECM compositions, thus adapting to the mechanical and functional requirements of the individual anatomical sites [13]. The composition of the ECM is in part regulated by the expression of genes controlled by the homeobox (HOX) transcription factors of the fibroblasts. This means that distinct fibroblast populations possess characteristic HOX gene expression patterns that determine their positional identity. In addition, HOX transcription factors regulate the expression of numerous other genes, causing fibroblasts to secrete signaling molecules that are transmitted to neighboring cells [13]. Through the secretion of growth factors, cytokines, and other signaling molecules, fibroblasts form an essential component of stem cell niches, where they regulate activation, self-renewal, and differentiation [13]. In adult tissues, fibroblasts remain predominantly in a quiescent state. However, tissue damage or mechanical stress trigger signaling cascades that induce fibroblast activation, proliferation, and functional reprogramming [13]. These processes can be regulated by several signaling pathways, including transforming growth factor-β (TGF-β), WNT, and platelet-derived growth factor (PDGF) signaling, and can additionally be triggered by pro-inflammatory cytokines [13]. Among these pathways, TGF-β is the central regulator of myofibroblast differentiation, whereas WNT signaling contributes to fibroblast activation, cell fate determination, and tissue repair [16, 17]. Myofibroblasts are key effector cells during wound healing, as they synthesize and remodel ECM components [13]. Dysregulation of these signaling pathways may result in sustained myofibroblast activation and excessive ECM production, leading to fibrosis [18]. Furthermore, the persistently activated fibroblasts and the resulting altered tissue microenvironment can promote tumor development and formation [19]. In addition to defective signaling, environmental factors such as UV radiation can affect fibroblast function. Chronic

UV exposure compromises the mechanical integrity of the dermis through ECM degradation and thus contributes to accelerated skin aging, also referred to as photoaging [20].

2.1.4 Stem Cells of the Skin

The skin contains, in addition to the predominant cell types, several distinct stem cell populations. Although these cells make up only a small fraction of the total cell population of the skin, they are essential for numerous functions. They possess the ability for self-renewal, a high proliferative potential, and the capacity to differentiate into other cell types. That means they are crucial for skin regeneration, wound healing, and maintenance of tissue homeostasis [21]. These cells remain in a quiescent state and are activated by intrinsic and extrinsic signals derived from the microenvironment [22].

2.1.4.1 Epidermal Stem Cells

The epidermis is characterized by a high rate of cellular turnover, making the maintenance of tissue homeostasis one of the crucial functions of epidermal stem cells (EpScs) [23]. As dead Keratinocytes are constantly shed from the skin surface, they must be replaced. EpScs are located within the basal layer of the epidermis to ensure this renewal while also contributing to hair regeneration and wound healing. The EpSc division can be categorized in either symmetrically or asymmetrically division. During asymmetric division, a stem cell generates one daughter stem cell and one so-called transit-amplifying cell (TAC), which subsequently after further differentiation differentiates into a keratinocyte [21, 24].

2.1.4.2 Dermal Stem Cells

In addition to EpScs, several stem cell populations have been identified within the dermis. These populations are considerably less well characterized. The mesenchymal stem cell population (MSCs) is one of the best studied group. MSCs have been described primarily within the mesenchymal compartments of the hair follicle, where they are mainly located in the connective tissue sheath and the dermal papilla. These cells contribute to processes such as hair growth, angiogenesis, and wound healing by differentiating to the mesodermal cell types required for these functions, including fibroblasts and endothelial cells [21, 25]. Besides MSCs, skin-derived precursors (SKPs) represent another population of stem cells found in the skin. Although these multipotent stem cells are also found in the dermal papilla of the hair follicle, they are not restricted to this region. The successful isolation of SKPs from interfollicular skin suggests the existence of an additional niche within the dermis. Besides differentiating into mesodermal cell types like MSCs, SKPs can differentiate into neuronal cell types, including neurons and Schwann cells [26]. The dermal stem cells (DSCs) investigated in the present study appear to represent a distinct stem cell population within the dermis. They can be distinguished from SKPs primarily by their expression of the neural crest marker NGFRp75, supporting the hypothesis that DSCs originate from the neural crest [27]. Like other stem cell populations, DSCs possess the capacity for self-renewal and, owing to their multipotency, can differentiate into melanocytes, neuronal cells, smooth muscle cells, adipocytes, chondrocytes, and Schwann cells [28]. Their precise localization within the dermis and the characteristics of their stem cell niche have not yet been suffi-

ciently investigated. However, several studies suggest that the extrafollicular dermis may serve as an additional reservoir for epidermal melanocytes [27, 28]. Using a three-dimensional skin reconstruction model, it was demonstrated for the first time that DSCs can differentiate into melanocytes and subsequently migrate from the dermis into the basal layer of the epidermis [29]. During melanocytic differentiation, DSCs continued to express the marker NGFRp75, while also acquiring the expression of melanocyte-specific markers. However, NGFRp75 expression was lost following their integration into the epidermis, suggesting that complete melanocytic differentiation into melanocytes may only occur after contact with the epidermal microenvironment. Despite these results the molecular mechanisms underlying the commitment of DSCs to the melanocytic lineage remain largely unresolved. It has been proposed that activation of the WNT signaling pathway contributes to melanocytic lineage commitment [29]. A better understanding of these mechanisms may provide valuable insights into melanocyte regeneration but also improve the understanding of the development of malignant melanoma (MM) and could contribute to the identification of novel therapeutic strategies.

2.1.4.3 Dermal Stem Cell Markers

Various markers have been reported to be expressed by DSCs. One marker that distinguishes DSCs from other dermal stem cell populations is the neural crest marker NGFRp75 [27]. NGFRp75 is a cell surface receptor for nerve growth factor (NGF) that is predominantly expressed on the surface of undifferentiated cells and is mainly found in cells derived from the neural crest [29, 30]. Another marker associated with DSCs is Nestin, a class VI intermediate filament protein originally identified in neural stem and progenitor cells. Although Nestin is not specific for DSCs, it is frequently used in combination with other markers to identify DSC populations [27, 31]. SOX10 is another marker that is not only expressed by melanocytes and Schwann cells but also by DSCs [32]. Therefore, SOX10 is of limited value as a standalone marker for the identification of DSCs but in combination with NGFRp75 can contribute to the identification of distinct DSCs. To distinguish DSCs from other NGFRp75 expressing cell types, exclusion markers can be of use. βIII-tubulin is a component of the microtubule cytoskeleton and is reported to primarily express in neurons and nerve fibers, so that it was chosen to serve as an exclusion marker [33].

In summary, the identification of DSCs cannot be achieved using only a single, exclusively expressed marker, but instead requires a combination of markers and the exclusion of other neural crest derived and mesenchymal cell populations. In this context NGFRp75, Nestin, and SOX10 are best regarded complementary markers whose co-expression, together with the absence of lineage specific differentiation markers such as βIII-Tubulin, allows for a more reliable delineation of DSCs within human skin.

2.2 UV Radiation

Solar radiation consists of three main spectral regions, ultraviolet (UV) radiation, visible light, and infrared radiation. In the electromagnetic spectrum, UV radiation is located directly below the visible light range. It can be divided into three segments, UVA, UVB, and UVC. UVA photons have the longest wavelength, ranging from 315 – 400 nm, and therefore the lowest photon energy. UVB photons have wavelengths between 280 – 315 nm, while UVC radiation has the shortest wavelength

range of 100 – 280 nm and consequently the highest photon energy [8].

The photon energy is inversely proportional to the wavelength (2.1).

$$E = \frac{h \cdot c}{\lambda} \tag{2.1}$$

With:

- E: photon energy in J
- c: speed of light ($2.998 \cdot 10^8$ m/s)
- h: Planck constant ($6.626 \cdot 10^{-34}$ Js)
- λ: wavelength in m

This means that shorter wavelengths correspond to higher photon energies. Consequently, UVB-radiation has a higher photon energy than UVA-radiation. The UV dose applied in studies or UV-based therapies can be determined by irradiance, which describes the energy delivered per unit area, and the exposure time (2.2).

$$H = I \cdot t \tag{2.2}$$

with:

- H: UV dose (J/m^2)
- I: irradiance (W/m^2)
- t: exposure time (s)

The extent of DNA damage depends on the applied UV radiation dose. However, the resulting damage is strongly influenced by the individual characteristics of the irradiated skin. In particular, skin pigmentation, skin thickness, and genetic factors play important roles [34, 35]. A quantitative approach exists to determine the UV-dose required to induce erythema, so skin redness and sunburn, or swelling, 24 – 48 hours after UV exposure. The minimum required UV-dose to cause erythema is referred to as the minimal erythema dose (MED). This value is particularly low in individuals with very fair skin due to their lower eumelanin content. Therefore, lighter skin types are associated with a narrower MED range and a higher risk of developing skin cancer [8, 35].

Although solar UV radiation makes up for only approximately 10% of the total solar radiation, it has considerable biological relevance. It is responsible for numerous harmful effects on human skin, which in the worst case can lead to skin cancer [36]. Therefore, it is classified as carcinogenic by several international organizations [37, 38]. Most of the UV radiation reaching the Earth's surface consists of UVA, accounting for approximately 95%, whereas UVB represents 5% of the incoming UV radiation [39]. The quality and quantity of UV radiation reaching the Earth's surface depend on various factors. These include the solar altitude, which is influenced by geographical location as well as the time of day and season. The intensity changes with the angle of the sun and depends on the atmosphere, as UV radiation must pass through it before reaching the Earth's surface [8, 40]. UVB

and UVC radiation possess higher energy and shorter wavelengths than UVA radiation, which leads to a partial absorption of UVB and a total absorption of UVC by the ozone layer and the Earth's atmosphere [34, 36]. The penetration depth of UV radiation that reaches the Earth's surface into the skin is also largely determined by the wavelength. In this context, longer wavelengths have a greater penetration depth than shorter wavelengths. The DNA has a maximum UV radiation absorption rate at 260 nm. So due to its high absorption rate by DNA, UVB radiation is predominantly absorbed in the epidermis and primarily causes direct DNA damage and erythema, so sunburn. In contrast, UVA-radiation has a considerably lower absorption by DNA, allowing it to penetrate the dermis of the skin. There, it contributes particularly to the damage of collagen and elastin as well as to photoinduced skin aging by forming ROS [8, 41]. Due to the different wavelengths of UV radiation, they have different effects on human tissue and its cells [34]. In general, UV radiation leads to DNA damage, immune suppression of the skin, and oxidative stress [42]. All of these factors promote the development of skin cancer.

2.2.1 UVB-induced DNA damage

UVB radiation is one of the most important causes of DNA damage in the skin and plays a central role in the development of skin cancer. DNA efficiently absorbs UV radiation, particularly within the wavelength range of approximately 245 – 290 nm, which means that DNA can effectively absorb UVB radiation [8, 43]. The most common UVB-induced DNA lesions are cyclobutane pyrimidine dimers (CPDs). These lesions are characterized by the formation of a cyclobutane ring between two neighbouring pyrimidine bases, which are primarily thymine or cytosine. Among these lesions, thymine-thymine (TT) dimers occur most frequently, followed by thymine-cytosine (TC), cytosine-thymine (CT), and cytosine-cytosine (CC) dimers, which are the least frequent [44]. In addition to CPDs, pyrimidine (6-4) photoproducts ((6-4)PPs) are also formed but occur at a significantly lower frequency. The frequency of CPD and (6-4)PP formation is influenced by the wavelength and dose of the applied UV radiation [45]. CPDs are formed approximately three times more frequently than (6-4)PPs and represent the main part of UV-induced DNA lesions. Both types of damage are classified as so-called bulky DNA lesions because they significantly alter the local structure of the DNA double helix [45]. These structural alterations can lead to incorrect replication and therefore mutations, for example, in tumor suppressor genes such as TP53 [44]. CPDs frequently result in 'UV signature mutations' that contribute to the development of skin tumors, such as basal cell carcinoma (BCC), squamous cell carcinoma (SCC) and MM [8, 34, 43].

2.2.2 UVA-induced DNA damage

In contrast to UVB radiation, UVA radiation is only weakly absorbed directly by DNA. Nevertheless, CPDs are considered the most frequent DNA lesions induced by UVA irradiation [44]. In addition to the directly induced CPDs, UVA also causes DNA damage through indirect mechanisms. Excitation of specific photosensitizers leads to the formation of ROS, which can induce oxidative damage to DNA bases. The most important UVA-induced oxidative DNA lesion is 8-oxo-7,8-dihydro-2'-deoxyguanosine (8-oxodG). This oxidized guanine base can form mismatches with adenine during DNA replication, causing predominantly G→T transversions. Such oxidative mutations have been detected in skin tumors and indicate the involvement of UVA-induced DNA damage in skin car-

cinogenesis [8, 43]. Additionally, UVA-radiation can induce oxidative processes involving melanin, leading to the formation of excited molecules that can damage DNA even after irradiation has stopped. Due to their delayed formation, these lesions are referred to as “dark CPDs” and have been observed primarily in melanocytes [44, 46].

2.2.3 DNA Repair

Following the formation of UV-induced DNA damage, cells activate a complex DNA damage response (DDR), which serves to recognize, repair, and, if necessary, eliminate damaged cells. Depending on the type of DNA lesion, distinct repair mechanisms are activated including nucleotide excision repair (NER) for bulky UV-induced photoproducts and base excision repair (BER) and mismatch repair (MMR) for non-bulky base damage and replication-associated errors. In addition, cells possess antioxidant defense mechanisms that neutralize ROS and thereby limit oxidative damage to DNA and other cellular components. Oxidatively modified bases generated by ROS are repaired predominantly by BER, which therefore plays a central role in the repair of both UV- and ROS-induced non-bulky base lesions [8]. For UV-induced DNA lesions such as CPDs, NER represents the most important repair mechanism. NER recognizes DNA lesions based on the structural distortions caused by the damage. Following recognition, the damaged DNA region is excised and removed from the affected strand. Subsequently, the DNA is resynthesized and the resulting gap is filled using the complementary strand as a template [47]. NER can be divided into two main pathways, the global genome repair (GGR) and the transcription-coupled repair (TCR). GGR repairs DNA damage throughout the genome, whereas TCR specifically repairs lesions in actively transcribed genes [34, 47]. The efficiency of repairing UV-induced lesions strongly influences genome stability and therefore the risk of mutation accumulation, particularly in resting cells. CPDs are removed relatively slowly by NER and may contribute to mutation formation if repair remains incomplete or incorrect. Furthermore, the tumor suppressor protein p53 plays a central role in the DNA damage response. Following UV-induced DNA damage, p53 can induce cell cycle arrest, allowing DNA repair mechanisms to take place [34]. When DNA damage exceeds a certain level or can no longer be successfully repaired, a protective mechanism, the apoptosis of the damaged cells, is activated. Severely damaged cells are specifically eliminated to prevent the transmission of potentially mutagenic alterations. UV-induced apoptosis can be initiated through intrinsic signaling pathways involving mitochondria and extrinsic signaling pathways. The intrinsic pathway leads to the release of cytochrome c, resulting in the formation of a protein complex called the apoptosome, which subsequently activates a caspase cascade. This cascade initiates the controlled apoptosis of the damaged cell [34, 48]. In contrast, the extrinsic apoptotic pathway promotes the expression of death receptors, such as FAS/CD95, which bind to the ligand FASL/CD95L. This interaction leads to the activation of another caspase signaling pathway, which initiates cell apoptosis [49, 50]. A classical example of UV-induced apoptosis in the skin are so-called sunburn cells. These are apoptotic keratinocytes after strong UV exposure. In order to prevent the transmission of mutations, these severely damaged cells must be removed. Therefore, apoptosis represents an important final protective barrier against tumor cell development after UV-induced DNA damage [34, 48].

2.3 Skincancer

Skin tumors are generally divided into two main groups: non melanoma skin cancers (NMSC), which include basal cell carcinoma (BCC) and cutaneous squamous cell carcinoma (SCC), and melanoma [8]. Together, these entities rank among the most frequently diagnosed malignancies worldwide, with several million new cases estimated each year when NMSCs are included (GLOBOCAN, International Agency for Research on Cancer, Global Cancer Observatory) [51]. The most important environmental factor contributing to the development of skin cancer is exposure to UV radiation, while genetic predisposition and individual skin pigmentation also significantly modulate skin cancer risk [35]. The development of both NMSC and melanoma is closely associated with the accumulation of UV-induced DNA damage, which may give rise to mutations and, over time, drive skin carcinogenesis.

2.3.1 Non-Melanoma Skin Cancer

Non-melanoma skin cancers (NMSC) are among the most common malignant tumors in humans and account for approximately 20% of all malignant tumor diseases [42]. The most important types of non-melanoma skin cancer include basal cell carcinoma (BCC) and squamous cell carcinoma (SCC), both of which originate from epidermal keratinocytes. BCC represents the most common type of skin cancer in humans. The most important shared risk factor for the development of NMSC is long-term and repeated exposure to UV radiation. Therefore, these tumors mainly occur in chronically sun-exposed areas of the skin, such as the head, neck, dorsal surfaces of the hands, or other frequently UV-exposed body regions [8, 42]. Despite their high incidence, NMSCs generally have a very good prognosis when diagnosed early and treated appropriately. Both BCCs and SCCs can be successfully treated in most cases, with early detection being very important [42].

2.3.2 Malignant Melanoma

Malignant melanoma (MM) represents the most aggressive and deadliest form of skin cancer. Although it accounts for less than 5% of all skin cancer cases, it is responsible for the majority of skin cancer-related deaths due to its high metastatic potential [27, 42]. The development of MM is determined by the interaction between genetic factors and environmental influences [34]. The most important environmental factor is chronic exposure to UV radiation, with particularly intense sun exposure and repeated sunburns during childhood increasing the risk of developing MM [34].

MM is generally considered to originate from cells of the melanocytic lineage, but the precise cell of origin that first accumulates the oncogenic alterations required for tumor formation is still unclear. Increasing evidence suggests that neural crest-derived DSCs may be involved in the development of UV-induced MM [27]. Currently, two theories are of scientific relevance (Figure 1).

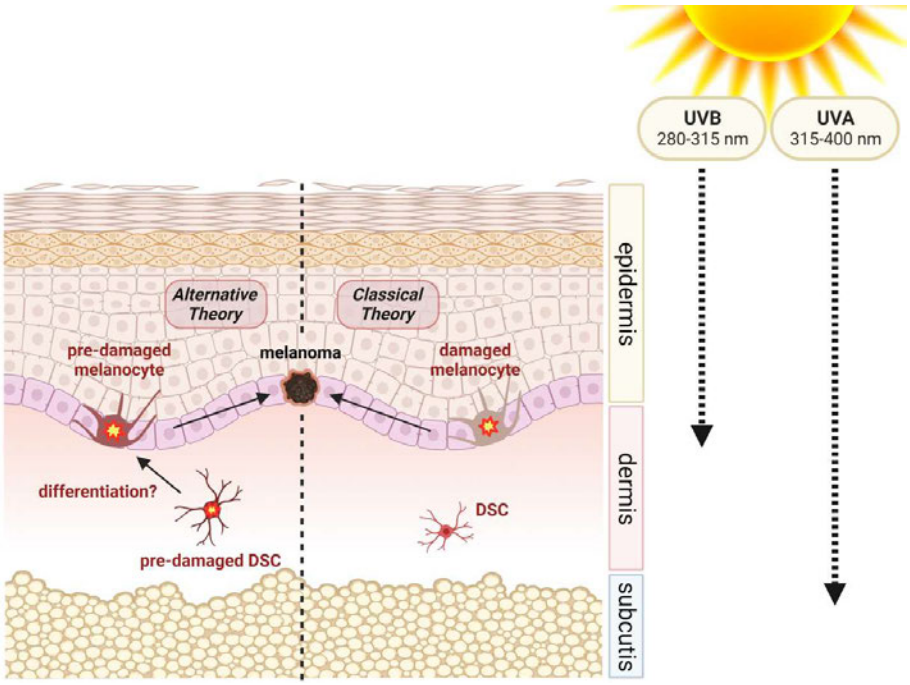


Figure 2. Theories of melanoma development and the influence of UV radiation. Illustration of the classical and alternative theories of melanomagenesis. UVA and UVB radiation demonstrate their different penetration depths within the skin. Created with BioRender by Christin Starzonek.

For the development of MM, the melanomagenesis, the classical theory is currently the most widely accepted. According to this concept, MM arises through the accumulation of mutations in mature epidermal melanocytes [27]. However, the exact cell of origin from which MM develops remains not fully understood. The alternative hypothesis proposes that less mature melanocyte precursor cells, particularly neural crest-derived DSCs, may contribute to the initiation of melanomagenesis [27]. The model of the alternative theory of melanomagenesis proposed by Hoerter et al. [52] assumes that extrafollicular dermal melanocyte stem cells are repeatedly exposed to UV radiation throughout life and can accumulate genetic alterations. Due to their presumed deeper localization within the dermis, UVA radiation may play a particularly relevant role. UVA can cause oxidative DNA damage in these cells, primarily through the formation of ROS and thereby contributing to genomic instability. Due to their self-renewal capacity, these cells may be particularly susceptible to the long-term accumulation of DNA damage. If damaged cells are not efficiently corrected by DNA repair mechanisms or eliminated through apoptosis, additional genetic alterations may accumulate over time [52]. According to this model, melanoma does not develop exclusively from damage occurring in fully differentiated melanocytes but may instead result from alterations occurring at different stages of melanocyte development [27, 52].

2.4 Aim of the Study

The aim of this study was to detect UV-induced CPDs in DSCs of human skin. Since DSCs are discussed as potential cells of origin for MM, this study aimed to investigate whether UV-induced DNA damage can be detected in this cell population within human skin. Furthermore, the repair kinetics of CPDs were analyzed at 0, 24, and 48 hours after UVA and UVB irradiation. For this purpose, different human skin samples from three body sites were examined, and potential DSCs

were identified based on the markers NGFRp75, SOX10, and Nestin. To distinguish these cells from neuronal cells, an additional βIII-tubulin co-staining was performed.

3 Materials

3.1 Devices

An overview of all devices employed in the experiments is provided in Table 1.

Table 1. Devices and equipment used in the experiment setup.

Device	Model	Manufacturer
Analytical scale	870-61	Kern & Sohn (Balingen-Frommen, Germany)
Camera	DX40C-285FW	Kappa opto-electronics GmbH (Gleichen, Germany)
Centrifuge	Mikro 200	Hettich Zentrifugen (Tuttlingen, Germany)
Confocal microscope	Stellaris 5	Leica (Wetzlar, Germany)
Cryostat	CryoStarTM NX50	Thermo Fisher Scientific (Waltham, MA, USA)
Fluorescence microscope	DMRB	Leica (Wetzlar, Germany)
Freezer (-20 °C)	Comfort 461724	Liebherr (Bulle, Switzerland)
Freezer (-72 °C)	MDF-U73V	Sanyo (Moriguchi, Japan)
Fridge	MKv 3910	Liebherr (Bulle, Switzerland)
Hazardous materials cabinet	20960-VBF.196.120-G+	Asecos GmbH (Gründau, Germany)
Hybridisation oven	Hybri 6/12	LTF Labortechnik GmbH (Wasserburg, Germany)
Incubator	CB 210	Binder GmbH (Tuttlingen, Germany)
Laminar flow cabinet	BSB-4A	Gelaire Flow Laboratories (Bremen, Deutschland)
Magnetic stirrer	IKAMAG RH	IKA-Labortechnik (Staufen, Germany)
Microscope	CKX53	Olympus (Hamburg, Germany)
pH-meter	766 Calimatic	Knick Elektronische Messgeräte GmbH (Berlin, Germany)
Pipette (1000 µl, 200 µl, 10 µl)	Research plus	Eppendorf (Hamburg, Germany)
Pipette controller	Pipetus-Accu	Hirschmann (Eberstadt, Germany)

Device	Model	Manufacturer
Radiation source	KAUVIR	KAUVIR-Konsortium (Technische Universität Darmstadt)
Vortex mixer	Vibrofix VF2	IKA-Labortechnik (Staufen, Germany)

3.2 Consumables

The consumables used in this study are listed in Table 2.

Table 2. Consumables used in the study.

Product	Manufacturer
Biopsy punch (6 mm, 8mm)	KAI Europe GmbH (Solingen, Germany)
Cardboard folder	
Coverslips	VWR (Radnor, PA, USA)
Coverglass	Karl Hecht GmbH (Sondheim v.d. Röhn, Germany)
Cryovial	Greiner Bio-One GmbH (Frickenhausen, Germany)
Falcon tube (15 ml, 50 ml)	Greiner Bio-One GmbH (Frickenhausen, Germany)
Gloves	Medline Industries, Inc. (Northfield, IL,USA)
Hydrophobic barrier marker	Agilent technologies (Santa Clara, CA, USA)
Petridish (various sizes)	Greiner Bio-One GmbH (Frickenhausen, Germany)
Pipette tips (1000 µl, 200 µl)	Ratiolab GmbH (Dreieich, Germany)
Pipette tips (10 µl)	Sorenson Bioscience Inc. (Murray, UT, USA)
Slides Starfrost	Engelbrecht Medizin- und Labortechnik GmbH (Edermünde, Germany)
Tubes	Greiner Bio-One GmbH (Frickenhausen, Germany)
Well-plate (12 wells)	Greiner Bio-One GmbH (Frickenhausen, Germany)

3.3 Chemicals and Reagents

All chemicals and reagents used in the experiment are summarized in Table 3.

Table 3. Chemicals and reagents used in this study.

Reagent	Manufacturer
Aqua dest.	Carl Roth GMBH (Karlsruhe, Germany)
Bovine Serum Albumin (BSA)	Carl Roth GMBH (Karlsruhe, Germany)
Calcium chloride $CaCl_2$	Carl Roth GMBH (Karlsruhe, Germany)
4',6-Diamidino-2-phenylindole (DAPI)	Sigma-Aldrich (Taufkirchen, Germany)
Dulbecco's Modified Eagle Medium (DMEM)	Gibco Life Technologies (Carlsbad, CA, USA)
Desoxyribonuclease I from Bovine Pancreas (DNase-I)	SERVA Electrophoresis GmbH (Heidelberg, Germany)
Fetal calf serum (FCS)	PeproTech (Hamburg, Germany)
Gentamycin	Carl Roth GmbH (Karlsruhe, Germany)
Glycerol	Carl Roth GmbH (Karlsruhe, Germany)
Goat serum	Dako (Glastrup, Denmark)
Hydrochloric acid HCl	Carl Roth GmbH (Karlsruhe, Germany)
Hepes powder	Carl Roth GmbH (Karlsruhe, Germany)
Kanamycin	Carl Roth GmbH (Karlsruhe, Germany)
Magnesium chloride hexahydrate $MgCl_2$x6 H_2O	Carl Roth GmbH (Karlsruhe, Germany)
Mowiol 4-88	Carl Roth GmbH (Karlsruhe, Germany)
Sodium chloride NaCl	Carl Roth GmbH (Karlsruhe, Germany)
Sodium hydrogen carbonate $NaHCO_3$	Carl Roth GmbH (Karlsruhe, Germany)
OCT	CellPath (Newton, United Kingdom)
Paraformaldehyde (PFA)	SERVA Electrophoresis GmbH (Heidelberg, Germany)
PBS-tablets	Gibco Life Technologies (Carlsbad, CA, USA)
Penicillin – streptomycin (Pen/Strep), 10,000 U/mL penicillin, 10,000 µg/mL streptomycin	Gibco Life Technologies (Carlsbad, CA, USA)
Tris hydrochloride C4H11NO3 x HCL	Carl Roth GmbH (Karlsruhe, Germany)
Triton X-100	Sigma-Aldrich (Taufkirchen, Germany)
Tween20	Carl Roth GmbH (Karlsruhe, Germany)
Water, nuclease-free, sterile-filtered, double-distilled	Carl Roth GmbH (Karlsruhe, Germany)

3.4 Buffers, Media and Solutions

The compositions of buffers, media and solutions used in this study are listed in Table 4.

Table 4. Buffers, media and solutions used in the study.

Name	Composition
Blocking buffer	20% FCS in PBS
BSA 1%	10 g/L BSA in $PBS^{+/+}$
BSA 3%	30 g/L BSA in $PBS^{+/+}$
BSA 10%	100 g/L BSA in $PBS^{+/+}$
DAPI	1 µg/mL in distilled water
DMEM (Transportation medium)	6.78 g of DMEM powder, 2.979 g of HEPES powder, penicillin (100 U/mL), streptomycin (100 µg/mL), gentamycin (100 µg/mL), kanamycin (100 µg/mL) in distilled water; pH 7.0
DMEM + 10% FCS	13.38 g/L DMEM powder, streptomycin (100 g/µL), penicillin (100 U/mL), 3.7 g/L $NaHCO_3$ and 10% FCS in distilled water; pH 7.3
DNase-I (20 000 U/mL)	25 mg DNase-I, 3.75 mL 0.15 M NaCl
DNase-I-buffer 10x	100 mM Tris-HCL, 25 mM $MgCl_2$ and 5 mM $CaCl_2$ in RNase-free water
Goat serum 5%	500 µL goat serum, 9.5 mL $PBS^{-/-}$
Mowiol mounting medium	Mowiol 4-88, 6 g glycerol, 6 mL distilled water, 12 mL of 0.2 M Tris-HCL (pH 8.5)
NaCl 0.15 M	58.44 g/L NaCl in distilled water
Paraformaldehyd 4%	8 g PFA, 200 mL PBS
$PBS^{+/+}$	100 mg/L $MgCl_2$x6 H_2O, 132 mg/L $CaCl_2$ in PBS; pH7.3
$PBS^{-/-}$	PBS; pH 7.3
Triton X-100 0.7%	0.35 mL Triton X-100 in 50 mL PBS
Tween-20 0.02%	200 µL Tween-20, 1 L distilled water

3.5 Antibodies

The primary antibodies used in this study are listed in Table 5.

Table 5. Primary antibodies used in the study.

Antibody	Species	Clone	Manufacturer
β-III-Tubulin	Mouse	TU-20	abcam (Cambridge, United Kingdom)
CD271 (LNGFR)	Mouse	REA 844 | ME20.4-1.H4	Miltenyi Biotec B.V. Co. KG (Bergisch Gladbach, Germany)
CPD	Mouse	TDM2	Cosmo Bio CO., LTD (Tokyo, Japan)
CPD	Mouse	KTM53	Kamiya Biomedical Company (Seattle, WA, USA)
Nestin	Rabbit	polyclonal	Sigma-Aldrich (St. Louis, MO, USA)
NGFRp75	Rabbit	EP1039Y	abcam (Cambridge, United Kingdom)
Sox10	Rabbit	D5V9L	Cell Signaling Technology (Danvers, MA, USA)

The secondary antibodies used in this study are listed in Table 6.

Table 6. Secondary antibodies used in the study.

Antibody	Manufacturer
Goat Anti Mouse Alexa 488	Invitrogen (Carlsbad, CA, USA)
Goat Anti Mouse Alexa 594	Invitrogen (Carlsbad, CA, USA)
Goat Anti Rabbit Alexa 488	Invitrogen (Carlsbad, CA, USA)
Goat Anti Rabbit Alexa 594	Invitrogen (Carlsbad, CA, USA)

4 Methods

4.1 Skin Preparation

4.1.1 Foreskin Preparation

Foreskin samples were obtained from donors at a pediatric clinic and transported in DMEM transport medium. Upon arrival, the foreskin biopsies were documented. Subsequently, further processing of the skin tissue biopsies was performed. Tissue preparation was carried out under sterile conditions in a clean bench using autoclaved or dry heat sterilized materials and instruments, as well as sterile-filtered solutions. The skin biopsies were removed from the transportation medium and then washed by rinsing with PBS, incubation in 70% ethanol for 30 seconds, and afterwards rinsing again with PBS. The washed foreskin tissue was then cut horizontally to obtain a flat tissue surface. For the preparation of biopsies, the foreskin tissue was cut into circular segments. For this purpose, the tissue was placed on a cutting board and cut using 8 mm biopsy punches. The resulting tissue punches were then distributed into small Petri dishes and covered with 1.0 – 1.5 mL $PBS^{+/+}$.

4.1.2 Preparation of Adult Skin from Other Body Sites

The first step in the preparation of the thigh and axillary skin was the removal of the subcutaneous adipose tissue. Afterwards, the skin samples were prepared in the same manner as the foreskin samples.

4.2 Irradiation

Irradiation of the tissue biopsies was performed under non-sterile conditions using a patented solar simulation device (patent application no. 10 2022 102 915.8). The device, referred to as the KAUVIR source, stands for 'Kombination statt Addition UV-bis IR-Strahlung'(engl.: 'Combination instead of Addition of UV to IR radiation') and consists of four different radiation sources. These sources can be combined and include infrared radiation, UVA, UVB and visible light [53]. The applied irradiation intensities were adjusted to approximate natural solar irradiation levels in order to obtain physiologically relevant conditions. To maintain a constant temperature of 35 °C during irradiation, the device was equipped with a heated Peltier element on which the samples were placed. In the experiments conducted in this study only the UVA and the UVB sources were used. Depending on the desired dose, the skin biopsies were irradiated for a defined period of time using the corresponding lamp. For UVA irradiation, a dose of 140 kJ/m^2 was applied, resulting in an irradiation time of 54 min and 59 s. UVB irradiation was performed for 38 min 38 s corresponding to a dose of 1500 J/m^2. To establish conditions comparable to those during irradiation, the control samples were incubated in an oven at 35 °C for the same period of time. The treatment conditions of all skin biopsies are summarized in Table 7.

Table 7. Overview of the applied UV doses. The foreskin biopsies were irradiated with either UVA or UVB. Biopsies obtained from the thigh or axillary skin were each exposed once to UVA and once to UVB irradiation. The irradiation doses were identical for all samples. Control samples were incubated in $PBS^{+/+}$ at 37 °C for the corresponding duration. At the designated time points of 0 h, 24 h, and 48 h, one punch biopsy from each skin sample was frozen and stored at -80 °C until cryosectioning.

Donor	Treatment	Dose	Irradiation time
H01/25, H01/26, VH11/25, VH12/25, VH14/25, VH20/25, VH21/25, VH22/25	Control	$PBS^{+/+}$ at 37 °C	-
H01/25, H01/26, VH14/25, VH20/25, VH21/25	UVA	140 kJ/m^2	54 min 59 sec
H01/25, H01/26, VH11/25, VH12/25, VH22/25	UVB	1500 J/m^2	38 min 38 sec

To assess the damage induced directly by irradiation, samples assigned to the T0 time point were transferred into tubes immediately after irradiation and stored at –80 °C. The remaining samples were incubated in DMEM supplemented with 10% FCS at 37 °C under 5% CO2 and 95% humidity until the respective post-irradiation time points (24 h and 48 h) and subsequently frozen at –80 °C.

4.3 Cryosectioning

A cryostat was used for the preparation of tissue sections. The working temperature was set to –23 °C. The frozen skin biopsies were briefly thawed and embedded upright in embedding medium (Optimal Cutting Temperature OCT compound) to provide structural support during cryosectioning. After the embedding medium had solidified, the tissue was trimmed in the cryostat until an appropriate cutting surface was visible under the microscope. Afterwards, 4 to 5 skin sections of the desired thickness were arranged in a row onto a microscope slide. The slides were labeled with donor ID, freezing time point, and irradiation condition and then stored again at –80 °C until staining. For these experiments, all tissue sections were cut to a thickness of 7 µm.

4.4 Immunofluorescence

To visualize the induced damage and identify the different cell types, an indirect immunofluorescence staining approach was used. In this method, an unconjugated primary antibody was applied to the skin sections, where it bound specifically to the target proteins. Subsequently, a fluorophore-conjugated antibody was used to detect the primary antibody by binding to the IgG molecule of the species in which the primary antibody had been raised. All staining procedures were performed according to an established and optimized protocol routinely used in the laboratory.

4.4.1 Staining of Different Cell-Type-Specific Proteins

For the detection of different proteins and cell types, an immunofluorescence protocol was used. In each staining procedure, two target proteins were labeled simultaneously. The tissue sections were first rehydrated in PBS for 5 min. Afterwards, the sections were fixed with 1.6% paraformaldehyde for 10 min at room temperature and then washed twice with PBS for 5 min each. Permeabilization was subsequently performed on ice using cold 0.5% triton X-100 in PBS for 5 min. To complete the fixation and permeabilization procedure, the slides were washed twice more with PBS. The sections were then incubated in 20% FCS/PBS for 30 min to block non-specific binding sites. Following a 5 min wash with PBS, the primary antibodies were applied. Depending on the staining the following primary antibodies were used: rabbit anti-SOX10, rabbit anti-Nestin and mouse anti-βIII-Tubulin. The staining was always combined with either rabbit anti-NGFRp75 or the conjugated mouse anti-CD271 (NGFRp75) antibody as a marker for dermal stem cells. When the conjugated anti-CD271 (NGFRp75) antibody was included in the primary antibody solution, all subsequent staining steps were carried out under minimized light exposure. Primary antibodies were diluted in 3% BSA/PBS and incubated overnight at 4 °C in a humidified chamber. All primary antibodies were used at a dilution of 1:100, except for anti-NGFRp75, which was applied at a dilution of 1:300. On the following day, the slides were washed three times for 10 min with PBS. Secondary antibodies were diluted 1:500 in 3% BSA/PBS and then applied and incubated for 30 min at 37 °C in a humidified chamber. Depending on the staining protocol and antibody combination, the following four secondary antibodies were used: anti-mouse Alexa Fluor 488, anti-mouse Alexa Fluor 594, anti-rabbit Alexa Fluor 488, and anti-rabbit Alexa Fluor 594. After incubation the slides were washed again three times for 10 min with PBS. The nuclear staining was then performed using DAPI (0.1 µg/mL) for 5 min and subsequently washed twice more with PBS and mounted using Mowiol mounting medium.

As a positive control for the staining procedures, especially for the detection of DSC markers, coverslips seeded with purified DSCs were used. These cells were cultured and enriched according to the protocol described by Starzonek et al. [27].

4.4.2 Staining of CPDs and NGFR p75 According to the DNase-I Protocol

The following staining protocol was performed and optimized based on a protocol established in a previous bachelor's thesis conducted in the laboratory [54]. The first step of the DNase-I-based staining protocol consisted of fixation and permeabilization. The slides containing the tissue sections were initially rehydrated in PBS for 5 min. Fixation was performed using 4% paraformaldehyde (PFA) for 15 min at room temperature under gentle agitation. Subsequently, the section were washed twice with PBS for 5 min each. Permeabilization was carried out using cold 0.7% Triton X-100 for 15 min at room temperature, followed by washing with PBS to remove residual detergent. DNA denaturation was then performed by incubating the sections with a DNase-I solution for 15 min at room temperature. The DNase-I solution was used at a concentration of 2000 U/mL. Prior to the blocking step, the sections were washed twice for 5 min with PBS. To saturate non-specific binding sites, the slides were incubated with 1% BSA/PBS for 30 min. Afterwards, the primary antibodies were applied and incubated overnight at 4 °C. For the detection of the UV-induced in form of CPDs the mouse anti-CPD antibody was used at a dilution of 1:500. For the detection of DSCs the rabbit anti-NGFRp75 was used at a dilution of 1:300. All primary antibodies were diluted in 3% BSA/PBS.

The washing steps after the incubation of the primary antibodies were performed using 0.02% Tween-20/PBS. Residual antibodies were removed by washing the sections five times for 2 min each. This was followed by a second blocking step with 5% goat serum for 30 min to prevent unspecific binding of the secondary antibodies. The secondary antibodies anti-mouse Alexa Fluor 488 and anti-rabbit Alexa Fluor 594 were diluted 1:500 in 1% BSA/PBS and incubated for 1 h at room temperature in a humidified chamber. From this step onwards, all staining procedures were carried out under minimal light exposure. Following the removal of unbound secondary antibodies by washing three times for 5 min with 0.02% Tween-20/PBS, the staining was stabilized with 1% paraformaldehyde for 10 min. The sections were then washed again two times for 5 min with 0.02% Tween-20/PBS. The final step consisted of nuclear staining with 1 µg/mL DAPI for 15 min, followed by washing with 0.02% Tween-20/PBS. Finally, the slides were mounted using Mowiol mounting medium and stored until analysis.

The second blocking step with 5% goat serum was included, after finding a lot of background signals at the initial staining with the anti-CPD antibody.

4.5 Microscopy

Two different microscopy techniques were used for image acquisition. Confocal laser scanning microscopy was employed as the primary imaging method for the main part of this work.

4.5.1 Fluorescence Microscopy

At the beginning of the study, the analysis of the stained skin sections was partly performed using a Leica DRMB fluorescence microscope equipped with various filter sets. Images were acquired using a DX40C-285FW camera in combination with the Kappa Camera Control software. The tissue sections were examined using 40× / 63× objectives. For image acquisition with the 63× objective, immersion oil was applied. The acquired images were subsequently processed and analyzed using Fiji (ImageJ 1.54p).

4.5.2 Confocal Microscopy

Image acquisition was primarily performed using a Leica Stellaris 5 confocal laser scanning microscope operating with the Leica LAS X software. The images were acquired using a 20× dry objective with a numerical aperture of 0.75. DAPI was excited using a 405 nm diode laser, whereas Alexa Fluor 488, Alexa Fluor 594 and APC were excited using the white-light laser. All laser lines were operated at an intensity of 2.00%. Reference wavelengths were set to 499 nm for Alexa Fluor 488, 590 nm for Alexa Fluor 594, and 655 nm for APC. To ensure comparability between samples, all images belonging to the same experiment were acquired using identical laser power and detector gain settings. The overview images were generally taken using a zoom factor of 1. For selected regions of interest, additional high-magnification images were obtained using a digital zoom factor of 3. For each staining, representative regions of the epidermis and dermis were selected and imaged under identical acquisition conditions. As the tissue sections naturally do not lie perfectly flat on the microscope slide, the focal plane was adjusted individually for each field of view prior to image acquisition. Images were acquired at the z-position exhibiting the strongest and most distinct fluorescence signal.

Afterwards, image processing was performed using Fiji (ImageJ 1.54p). Scale bars with a size of 50 µm were added and images were rotated when necessary for presentation purposes. In addition, brightness, contrast and Gaussian blur adjustments were applied to improve image visualization. For all comparative analyses, identical image-processing parameters were used for all images within the same experiment.

5 Results

The main objective of this study was to identify DSCs, which are regarded as precursor cells of melanocytes, and to investigate the extent of UV-induced DNA damage within this cell population. DNA damage was assessed by the detection of CPDs, which represent characteristic lesions formed after UV exposure. The following section summarizes the results obtained from the immunofluorescence analysis of juvenile foreskin, axillary skin, and thigh skin biopsies. Initially, different markers were evaluated for the identification of DSCs. Afterwards, the staining conditions were optimized, and the established protocols were applied to investigate UV-induced DNA damage by CPD detection.

5.1 Determination of the Specificity of the Secondary Antibodies

To assess the specificity of the secondary antibodies and to exclude them as a source of nonspecific background staining, the skin sections were incubated with the secondary antibodies alone, as shown in Figure 3.

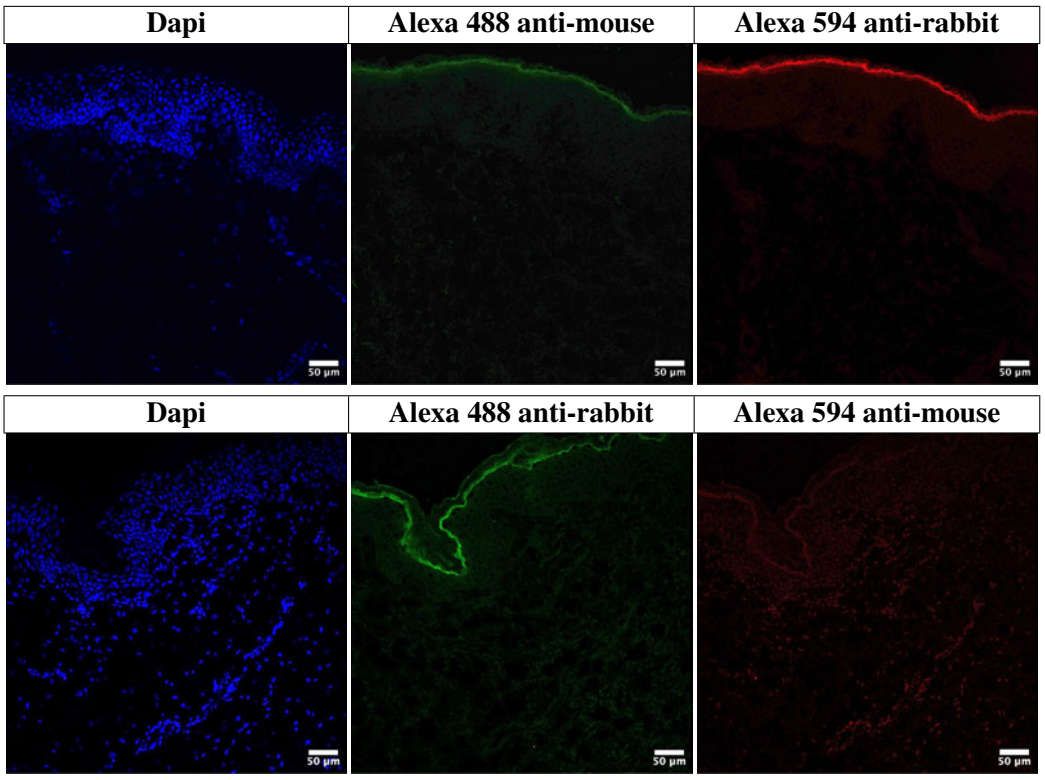


Figure 3. Secondary antibody staining control. Cell nuclei were stained with DAPI. The secondary antibodies used in the experiments, Alexa Fluor 488- and Alexa Fluor 594-conjugated anti-mouse and anti-rabbit antibodies, were applied. The detector gain settings were kept constant. The images were acquired using a confocal laser scanning microscope using a 20× dry objective.

The secondary antibodies primarily produced background staining in the stratum corneum. In contrast, little to no fluorescence signal was detected within the dermis.

5.2 Evaluation of Markers for Identification Dermal Stem Cells and Dermal Structures

To identify DSCs in the skin, different markers were used. After staining with anti-NGFRp75, it was observed that the marker also labeled numerous structures within the dermis. Consequently, additional stem cell markers, including SOX10, Nestin and βIII-Tubulin, were used to more precisely identify DSCs.

5.2.1 Co-expression of SOX10 and NGFRp75 as a Marker Combination for Dermal Stem Cells

SOX10 is a marker commonly used for the identification of stem cells. As both the anti-SOX10 primary antibody and the originally used anti-NGFRp75 primary antibody were raised in rabbits and would therefore require detection with the same anti-rabbit secondary antibody, the NGFRp75-APC conjugated antibody was used for a double staining. In addition to the skin sections, coverslips containing purified DSC cultures were stained as positive controls. The corresponding results are presented in Figure 4.

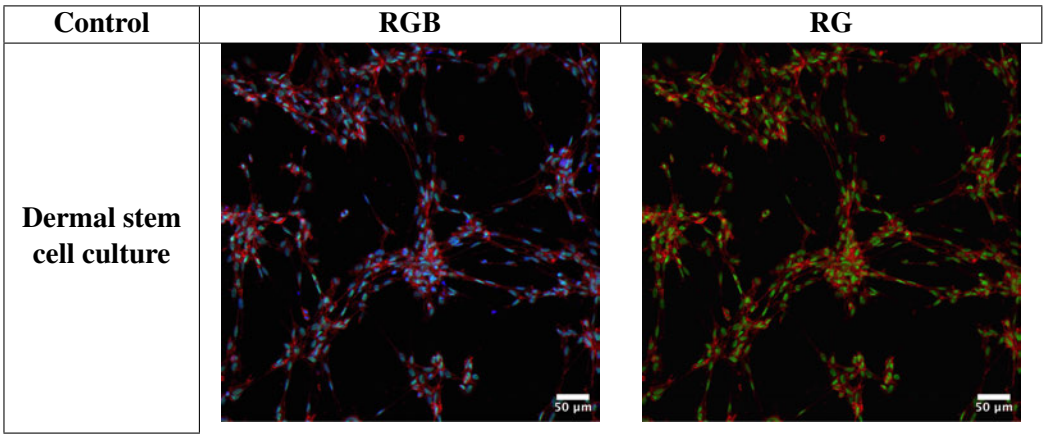


Figure 4. Dermal stem cell culture shows SOX10/NGFRp75 double-positive cells. Representative image of DSCs grown on coverslips following immunofluorescence staining for SOX10 and NGFRp75. DAPI is shown in blue, SOX10 in green, and NGFRp75 in red. The RG image represents the merged red and green channels, while the RGB image shows the overlay of all three channels (red, green and blue). All cells showed co-expression of SOX10 and NGFRp75.

Figure 4 demonstrates that all DSCs on the coverslips are double-positive for both SOX10 and NGFRp75. This indicates that each DSC expresses both markers. Thus, dermal cells, expressing SOX10 as well as NGFRp75 in the skin biopsies represented potentially DSCs. The same staining was performed on axillary skin and juvenile foreskin tissue. The results are shown in Figures 5 – 7.

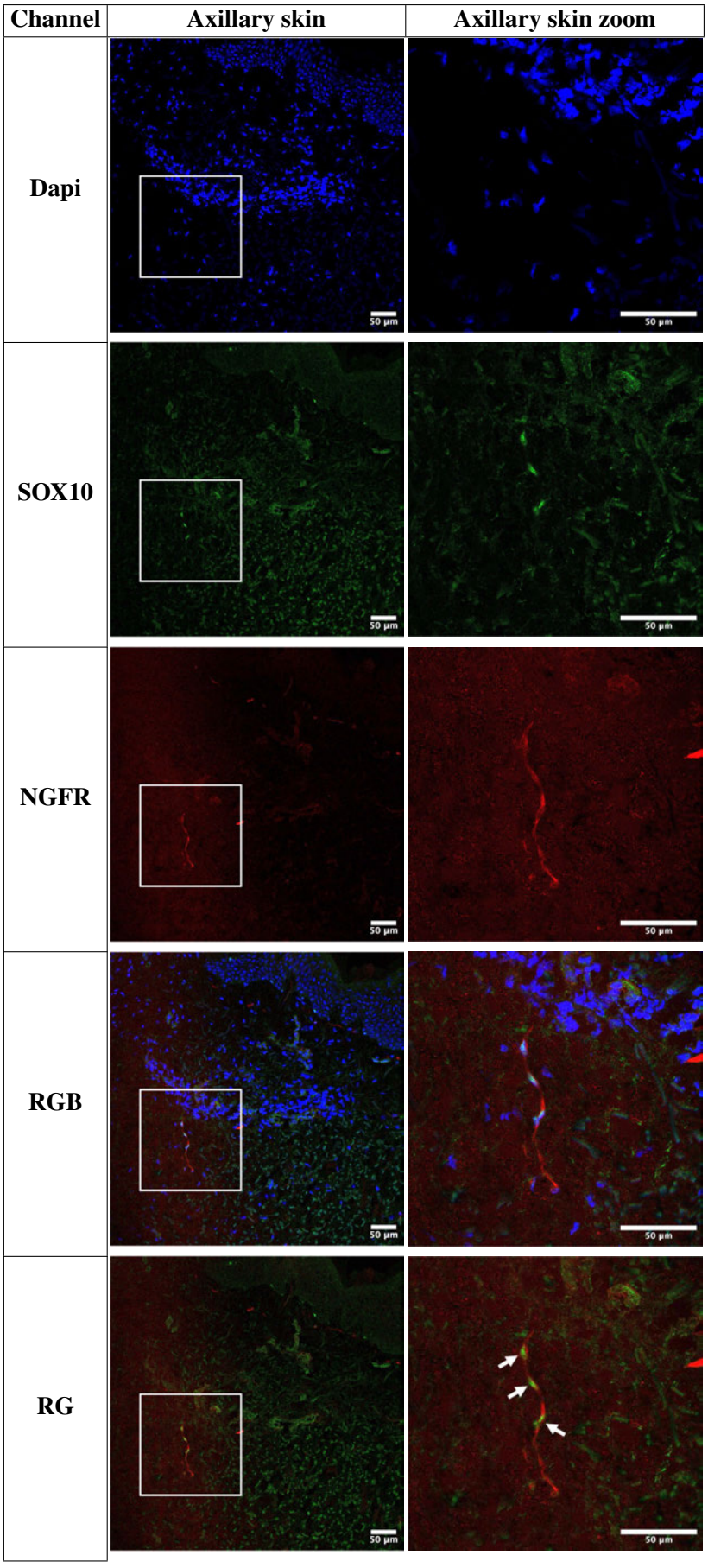


Figure 5. Axillary skin sections stained for SOX10 and NGFRp75, showing SOX10/NGFRp75 double-positive cells. Representative images of axillary skin following immunofluorescence staining for SOX10 and NGFRp75. Nuclei were stained with DAPI which is shown in blue, SOX10 is shown in green, and NGFRp75 is shown in red. The RG image represents the merged red and green channels, while the RGB image shows the overlay of all three channels (red, green and blue). Arrow = SOX10- and NGFRp75-positive cells.

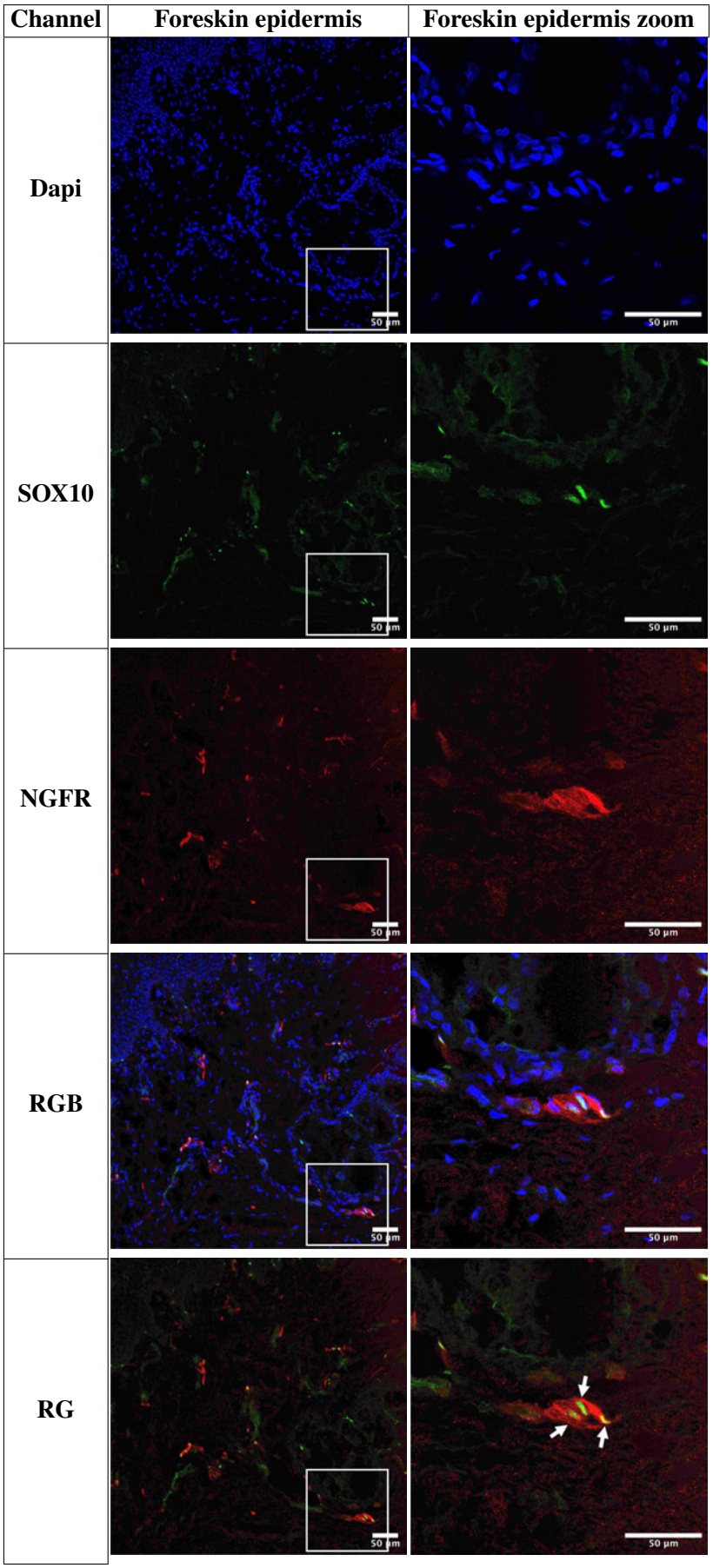


Figure 6. Juvenile foreskin sections stained for SOX10 and NGFRp75, showing SOX10/NGFRp75 double-positive cells. Representative images of juvenile foreskin following immunofluorescence staining for SOX10 and NGFRp75. Nuclei were stained with DAPI which is shown in blue, SOX10 is shown in green, and NGFRp75 is shown in red. The RG image represents the merged red and green channels, while the RGB image shows the overlay of all three channels (red, green and blue). Arrow = SOX10- and NGFRp75-positive cells.

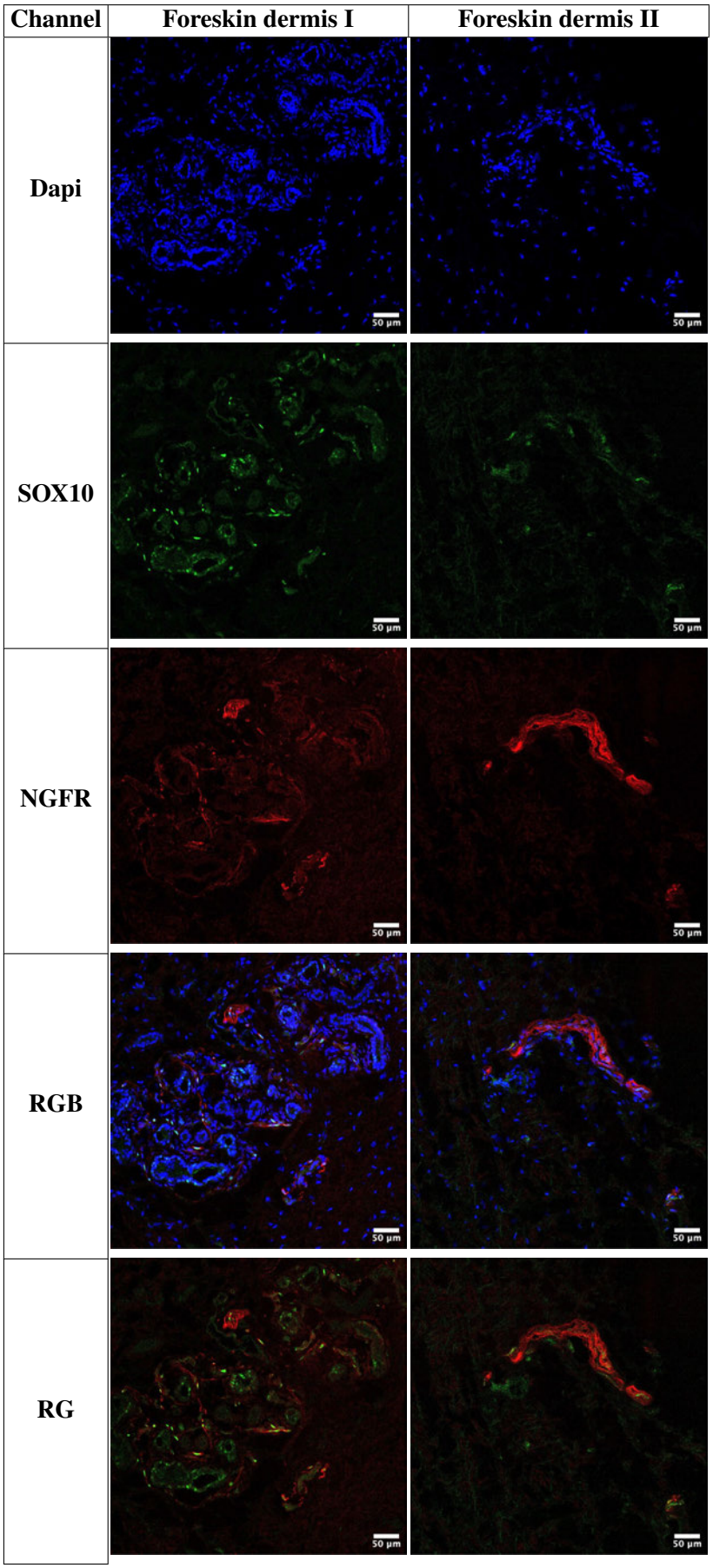


Figure 7. Juvenile foreskin sections stained for SOX10 and NGFRp75. Images of the dermis. Representative images of two different areas of the dermis of juvenile foreskin following immunofluorescence staining for SOX10 and NGFRp75. Nuclei were stained with DAPI which is shown in blue, SOX10 is shown in green, and NGFRp75 is shown in red. The RG image represents the merged red and green channels, while the RGB image shows the overlay of all three channels (red, green and blue).

In the axillary skin sample, NGFRp75-positive cells located directly in the dermis were also positive for SOX10 (Figure 5, arrow). This co-expression is particularly evident in the magnified image. These cells are therefore double-positive for both markers. Based on their localization these cells are likely to represent DSCs. In general, several double-positive cells with comparable localization were observed throughout the axillary tissue sections. In the juvenile foreskin biopsy, multiple NGFRp75-positive cells can be observed immediately beneath the epidermis. Whenever the nuclei of NGFRp75-positive cells were visible, they also show SOX10 positivity (Figure 6). Figure 7 ('Foreskin dermis I') shows a distinct arrangement of nuclei which form elongated, enclosed luminal structures. These structures may correspond to sweat glands as shown in 5.3. Notably, several cells appear to be NGFRp75-positive, as indicated by a strong red signal. In addition, SOX10-positive nuclei are also observed within the surrounding tissue. These double-positive cells are predominantly located between individual structures. Their marker expression pattern suggests that they may represent neural crest derived cells. In contrast, Figure 7 'Foreskin Dermis II' contains a structure that clearly shows NGFRp75-positive cells. However, SOX10 staining is weak or absent. This finding suggests that these NGFRp75-positive cells are unlikely to be neural crest–derived DSCs and therefore are not expected to represent precursor cells of the melanocytic lineage. In both samples, SOX10 expression was additionally observed in a subset of cells located within the basal layer that did not express NGFRp75. Based on their location and the established role of SOX10 as a melanocytic marker, these cells most likely represent melanocytes.

5.2.2 Co-expression of Nestin and NGFRp75 as a Marker Combination for Dermal Stem Cells

For double staining, an APC conjugated NGFRp75 antibody was used together with an anti-Nestin antibody to identify double positive DSCs in cultured DSCs and skin sections. As with the previous staining, double-positive cells were identified using anti-Nestin together with anti-NGFRp75-APC primary antibody. Cultured DSCs were included as a positive control. The corresponding results are shown in Figure 8.

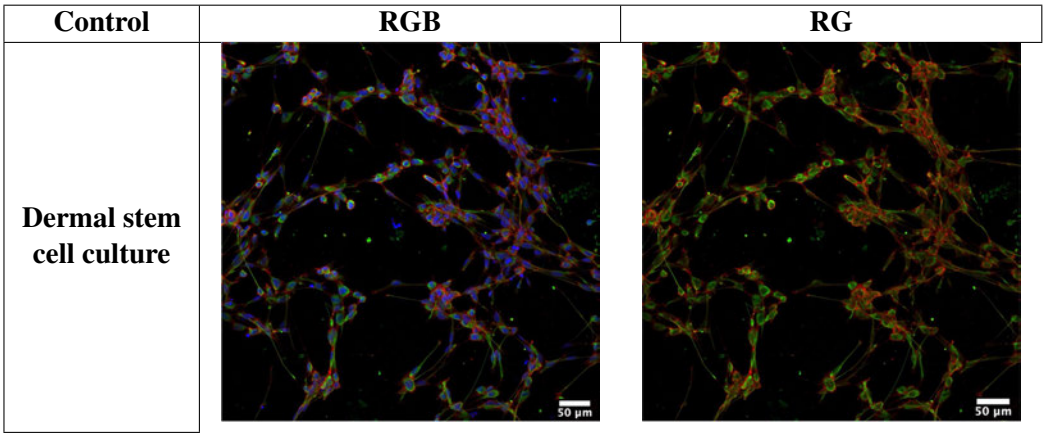


Figure 8. Dermal stem cell culture stained for Nestin and NGFRp75, showing co-expression of Nestin and NGFRp75 in all cells. Representative image of DSCs on coverslips following immunofluorescence staining for Nestin and NGFRp75. DAPI is shown in blue, Nestin in green, and NGFRp75 in red. The RG image represents the merged red and green channels, while the RGB image shows the overlay of all three channels (red, green and blue).

Like NGFRp75, Nestin is not located in the nucleus. It is an intermediate filament protein and is

therefore localized within the cytoplasm of the cell. In the positive control shown in Figure 8, all DSCs show a double-positive staining for Nestin and NGFRp75. However, the results of the double staining in the skin sections that are shown in Figure 9 indicate that, in addition to DSCs, Nestin is also expressed by other cell types in the skin.

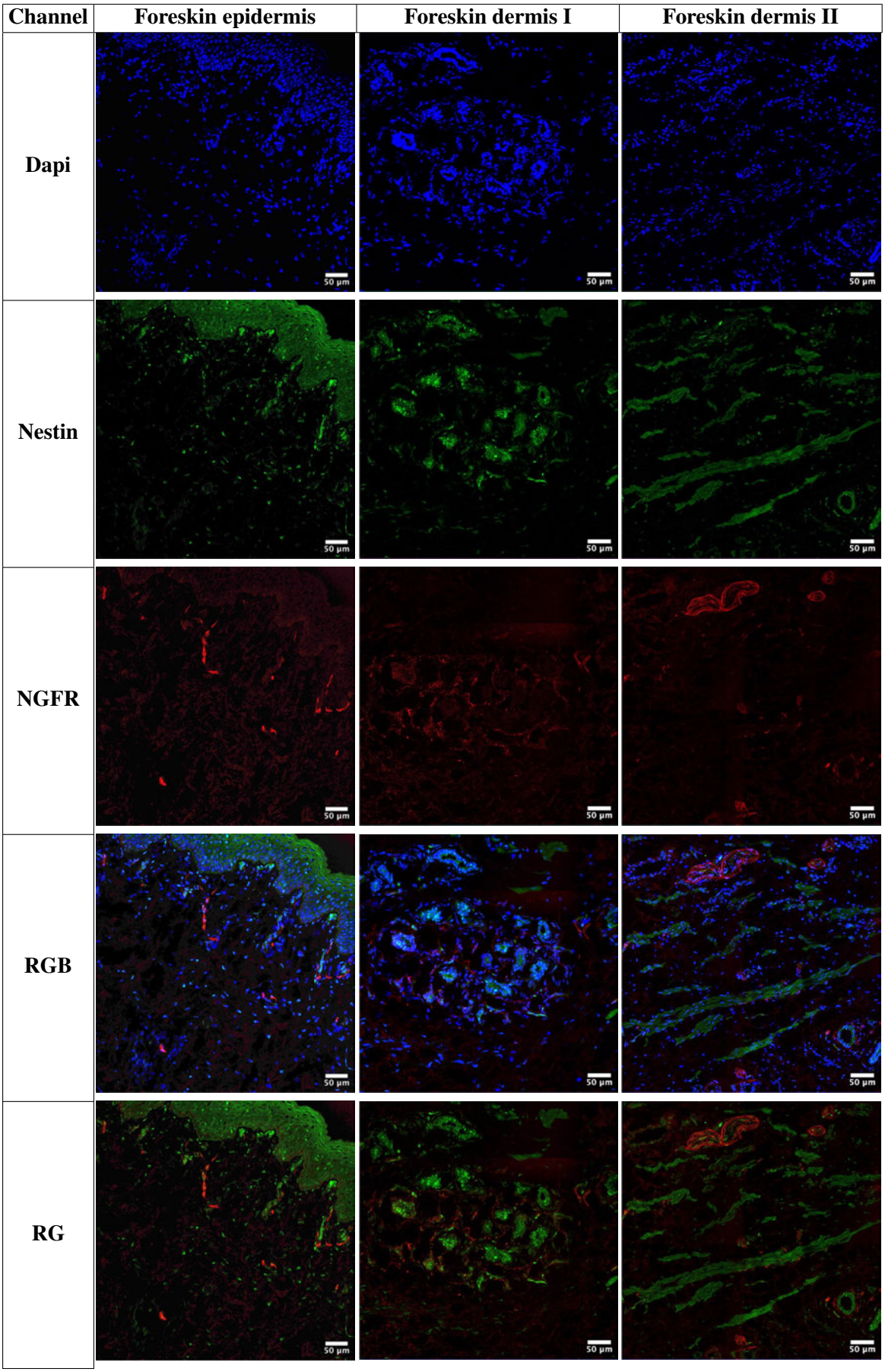


Figure 9. Juvenile foreskin section shows widespread Nestin expression and NGFRp75 staining. Representative images of juvenile foreskin skin following immunofluorescence staining for Nestin and NGFRp75. Nuclei were stained with DAPI which is shown in blue, Nestin is shown in green, and NGFRp75 is shown in red. The RG image represents the merged red and green channels, while the RGB image shows the overlay of all three channels (red, green and blue).

In all skin sections, an extensive Nestin signal was observed. In addition, Nestin-positive signals were detected not only in the cytoplasm but also within the nuclei of certain cells. While the NGFRp75-positive cells were generally double-positive for both NGFRp75 and Nestin, numerous additional cell populations showed Nestin positivity in the absence of detectable NGFRp75 expression. Particularly prominent Nestin staining was observed in elongated, enclosed luminal structures as observed in Figure 9 'Foreskin Dermis II', where strong green signals were detected. These structures may correspond to eccrine sweat glands, as shown in 5.3..

5.2.3 Assessment of βIII-Tubulin as a Neuronal Marker in NGFRp75-positive Dermal Stem Cells

The βIII-Tubulin antibody was used to visualize neuronal structures within the skin and to distinguish peripheral nerve cells from NGFRp75-positive DSCs. As in previous experiments, cultured DSCs were included as positive controls (Figure 10).

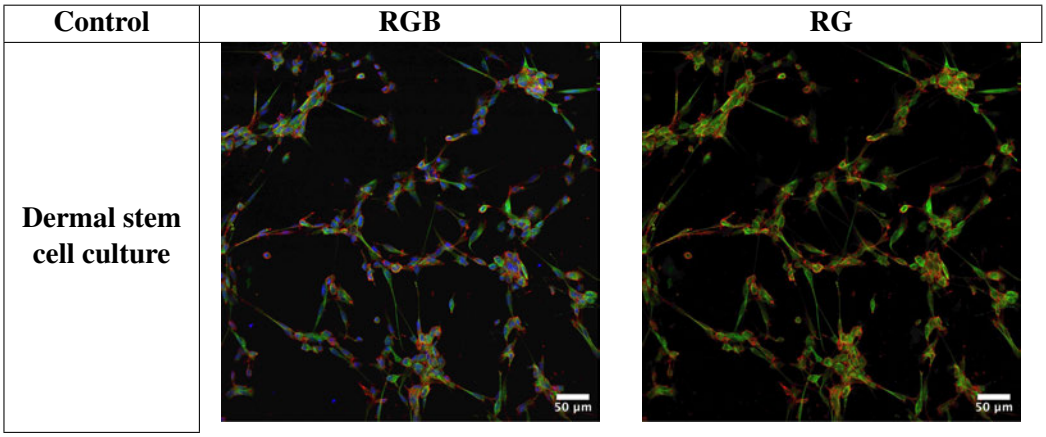


Figure 10. Dermal stem cell culture stained for βIII-Tubulin and NGFRp75, showing co-expression of both markers in all cells. Representative image of DSCs grown on coverslips following immunofluorescence staining for βIII-Tubulin and NGFRp75. DAPI is shown in blue, β-III-Tubulin in green, and NGFRp75 in red. The RG image represents the merged red and green channels, while the RGB image shows the overlay of all three channels (red, green and blue).

The control staining for βIII-Tubulin and NGFRp75 shown in Figure 10 also demonstrates a double-positive signal in all DSCs. The corresponding skin section staining is shown in Figure 11.

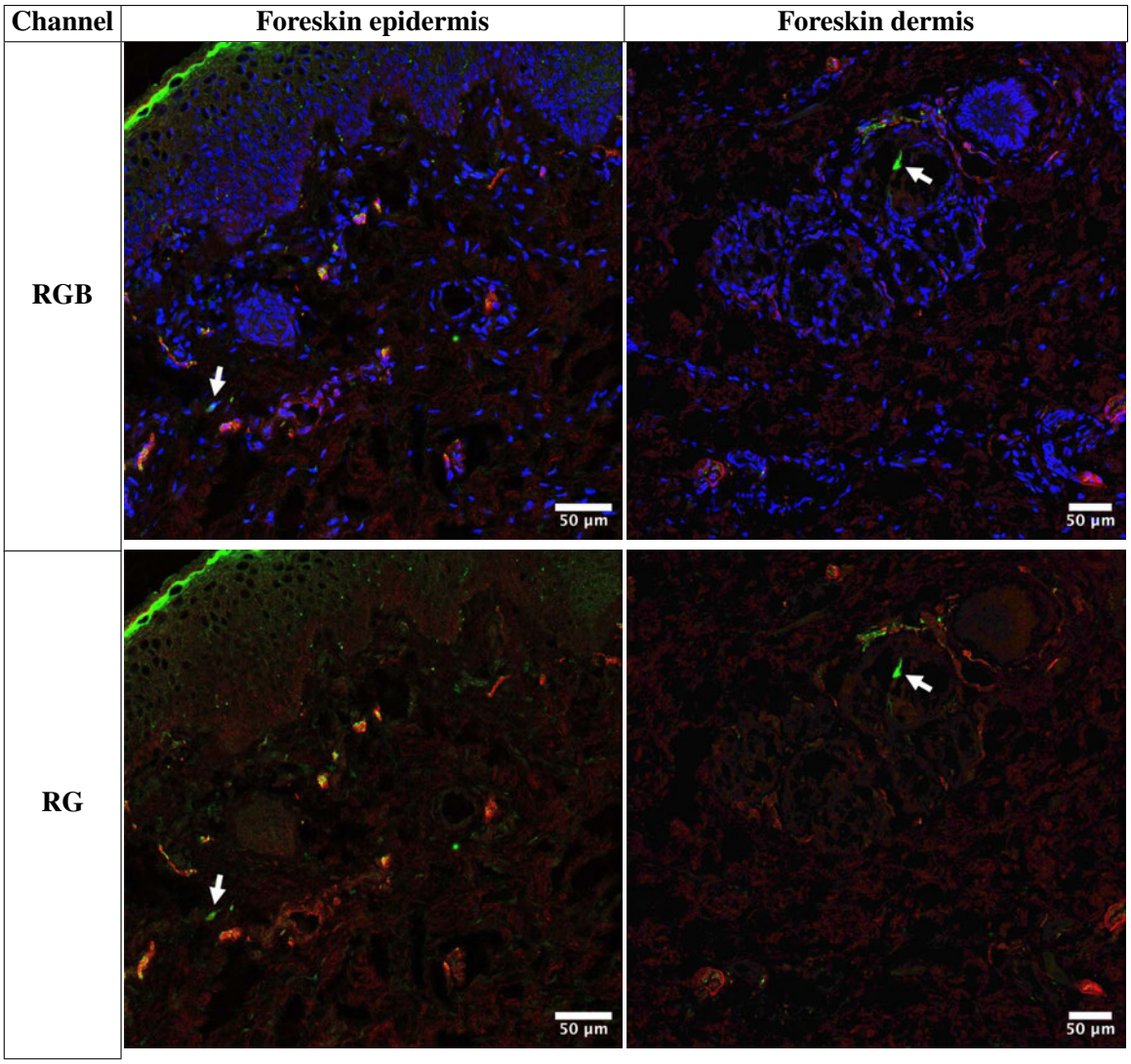


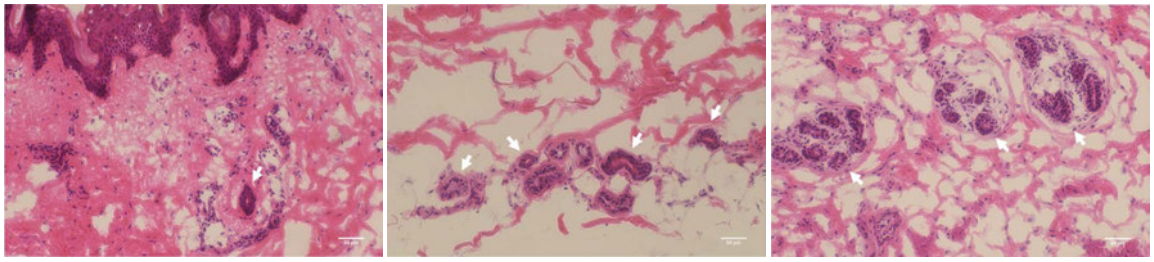
Figure 11. Juvenile foreskin sections stained for βIII-Tubulin and NGFRp75, showing double-positive cells and βIII-Tubulin-positive cells. Representative images of juvenile foreskin skin following immunofluorescence staining for βIII-Tubulin and NGFRp75. Nuclei were stained with DAPI which is shown in blue, βIII-Tubulin is shown in green, and NGFRp75 is shown in red. The RG image represents the merged red and green channels, while the RGB image shows the overlay of all three channels (red, green and blue). Arrow = βIII-Tubulin-positive/NGFRp75-negative cell.

Figure 11 shows images of a foreskin tissue section. NGFRp75-positive cells are observed both in the upper dermis (Figure 11 'Foreskin epidermis') and in the deeper dermis (Figure 11 'Foreskin dermis'). These NGFRp75-positive cells also showed βIII-Tubulin positivity. However, there are βIII-Tubulin-positive cells that do not express NGFRp75 (arrows).

5.3 Identification of Structures in the Dermis using Hematoxylin and Eosin Staining

To identify and gain a better understanding of the structures found during immunofluorescence staining in human skin, a hematoxylin and eosin (H&E) staining was performed. For this purpose, three different skin biopsies were used: thigh skin, adult foreskin and juvenile foreskin. After consultation with a histopathologist, several skin structures could be identified. The corresponding structures are

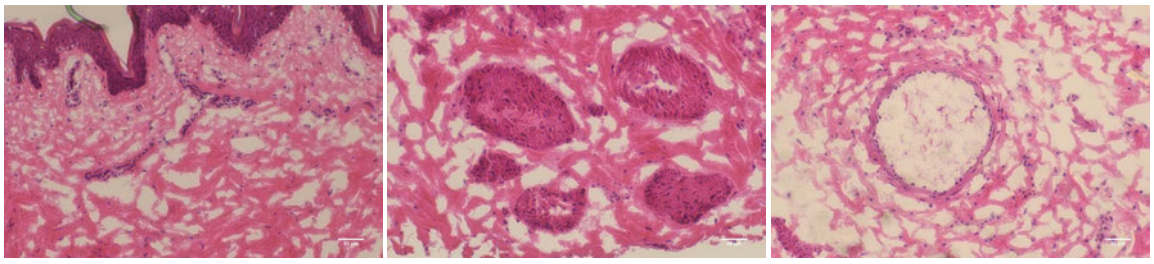
shown in Figures 12 and 13.



A. Thigh skin B. Thigh skin C. Juvenile foreskin

Figure 12. HE-staining of different skin biopsies with eccrine sweat glands. Representative images of eccrine sweat gland ducts and secretory end pieces in different skin biopsies. A) Eccrine sweat gland in an adult thigh skin sample beneath the epidermis. B) Multiple eccrine sweat glands in an adult thigh skin deep in the dermis. C) Multiple eccrine sweat glands in juvenile foreskin in the dermis. Images were acquired using a microscope with a dry 10× objective. Arrow = eccrine sweat glands. Scale bar = 50 µm.

Figure 12 shows representative images of different structural components of eccrine sweat glands in different skin samples. Figure 12A depicts a sweat gland duct located immediately beneath the epidermis, while the remaining images (Figure 12B and 12C) of the sweat glands were obtained from structures situated deeper within the dermis. The sweat gland ducts are characterized by a bilayered epithelial lining, whereas the secretory end pieces are lined by a single layer of epithelial cells. In addition, the secretory units are surrounded by spindle-shaped myoepithelial cells.



A. Thigh skin B. Adult foreskin C. Juvenile foreskin

Figure 13. HE-staining of skin biopsies with various structures in the dermis. Representative images of various structures in different skin biopsies. A) Blood vessels in an adult thigh skin sample beneath the epidermis. B) Multiple smooth muscle bundles in an adult foreskin in the dermis. C) Multiple large lumen in juvenile foreskin in the dermis. The images were acquired using a microscope with a dry 10× objective. Scale bar = 50 µm.

Figure 13 shows several distinct structures within the dermis. In Figure 13A, branches of blood vessels are visible located directly beneath the epidermis. These vessels are primarily lined by endothelial cells and are surrounded by various dermal cell types. In Figure 13B, structures lacking a discernible lumen can be observed. These structures are composed predominantly of spindle-shaped cells, a characteristic feature of smooth muscle bundles. Such bundles are commonly found in the foreskin, where they contribute to its elasticity and functional adaptability, enabling adaptation to mechanical demands and environmental temperature changes [55]. Figure 13C shows a structure with a comparatively large lumen. Due to the absence of intraluminal contents, its precise identity cannot be determined with certainty. However, based on its morphological appearance, the structure most likely represents a vein.

5.4 UV-induced DNA Damage in Different Skin Tissues

To evaluate the extent of UV-induced DNA damage in different skin tissues, the formation of CPDs was analyzed. CPDs were detected using the anti-CPD (TDM-2) antibody according to the established staining protocol (see Methods 4.4.2). To identify DSCs within the tissue sections, co-staining with an anti-NGFRp75 antibody was performed. Juvenile foreskin, thigh skin, and axillary skin biopsies were irradiated and subsequently analyzed.

5.4.1 Assessment of Antibody Dilution Conditions

The initial dilution of the CPD antibody was 1:200. During the initial staining, it became evident that the antibody exhibited a markedly higher sensitivity than expected. Therefore, an antibody dilution series was performed to determine the optimal staining conditions. Dilutions of 1:500, 1:1000, 1:2500, 1:5000 and 1:10000 were tested. Figure 14 shows control skin biopsy samples that were not irradiated and served as a negative control. Figure 15 presents the irradiated skin biopsy sample.

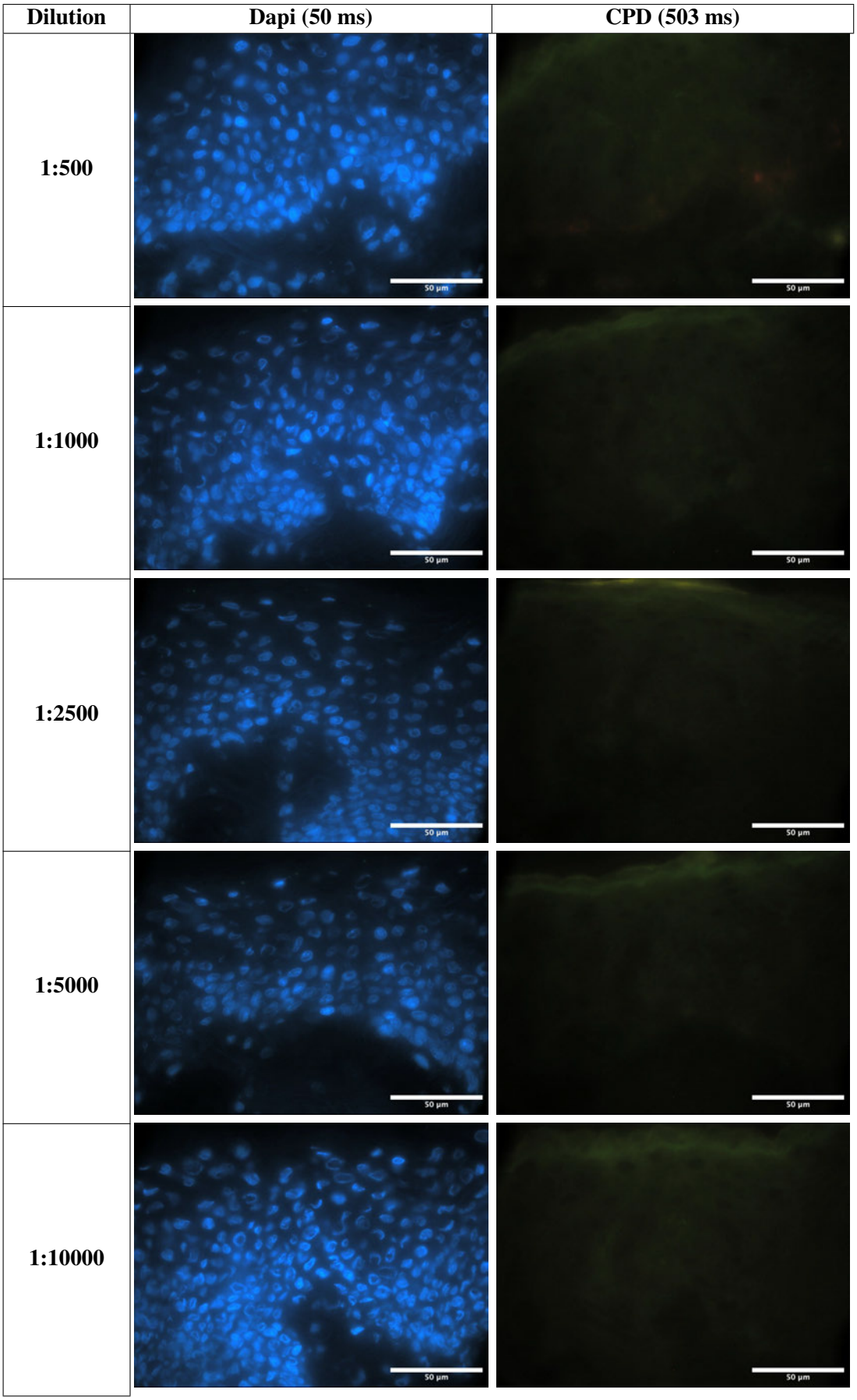


Figure 14. Non-irradiated control samples stained with different CPD antibody dilutions, showing no background signal. Representative images of the CPD-negative control foreskin biopsy samples stained with five different antibody dilutions from 1:500 to 1:10000. CPD antibody dilutions. Nuclei were stained with DAPI (blue) and acquired with an exposure time of 50 ms. CPDs (green) were acquired with an exposure time of 503 ms. The images were acquired using a fluorescence microscope with a 63× oil-immersion objective.

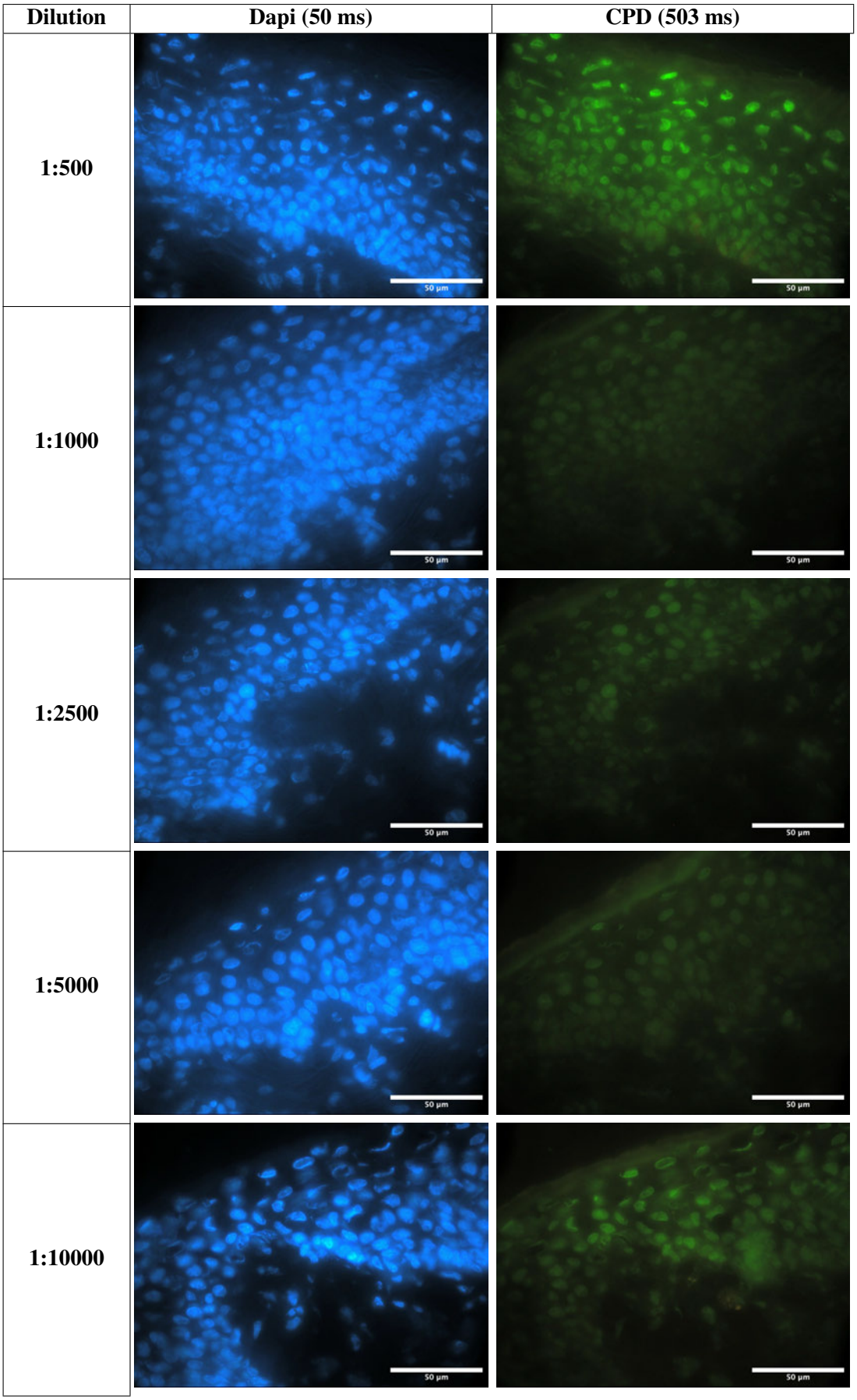


Figure 15. UVB-irradiated skin stained with different CPD antibody dilutions. Representative images of the UVB-irradiated (1500 J/m^2) foreskin biopsy samples with five different antibody dilutions from 1:500 to 1:10000. CPD antibody dilutions. Nuclei were stained with DAPI (blue) and acquired with an exposure time of 50 ms. CPDs (green) were acquired with an exposure time of 503 ms. The images were acquired using a fluorescence microscope with a 63× oil-immersion objective lens.

The control samples in Figure 14 showed no unusual signals. So, based on the results in Figure 15 a dilution of 1:500 was selected, as it provided a strong and uniform staining signal. A successful staining shows a distinct green fluorescence of the cell nuclei, while the surrounding tissue appears dark and exhibits only low autofluorescence. Although higher dilutions also produced detectable signals, the staining was not consistent across the entire tissue section. This approach reduced antibody consumption while still yielding reliable staining quality.

5.4.1.1 Reduction of False-Positive Signals

During the staining with the anti-CPD antibody, a signal was detected in the non-irradiated control samples that visually resembles specific CPD staining. However, since these samples were not exposed to UV radiation, CPD formation is not expected, and thus any true CPD-specific signal should be absent (as shown for the control in Figure 14). Figure 16 shows CPD-positive staining in the lower epidermis, the basal layer and the upper dermis. Given the localization and the fact that this sample served as the non-irradiated control, the observed staining is unlikely to represent UV-induced DNA damage and does not match the expected pattern of UV-induced CPD formation, which would primarily occur in directly exposed epidermal cell layers.

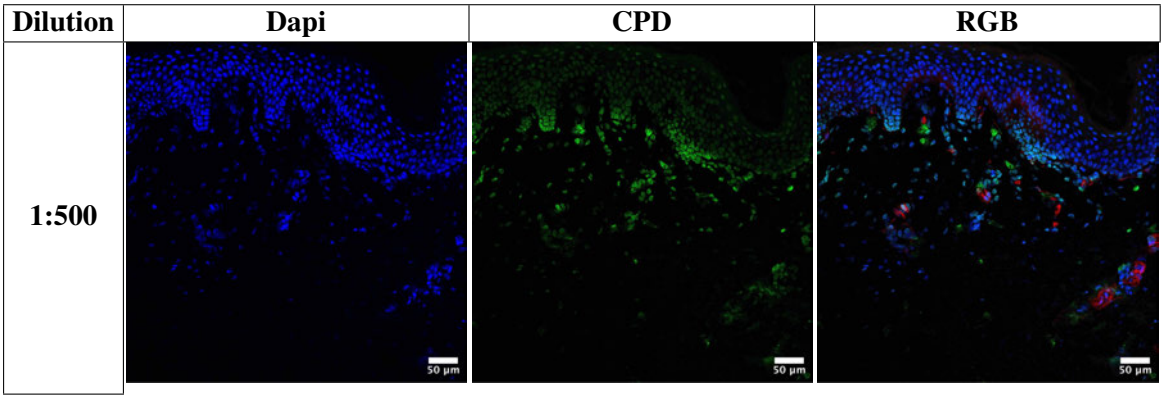


Figure 16. False-positive signals with the DNase-I treatment staining. Representative images of a non-irradiated control foreskin biopsy following immunofluorescence staining for CPD and NGFRp75. Nuclei were stained with DAPI which is shown in blue, CPDs are shown in green, and NGFRp75 is shown in red. The RGB image shows the overlay of all three channels (red, green and blue).

To address this issue, an additional optimization experiment was conducted. Two modifications to the standard staining protocol were evaluated. In the first experiment an additional blocking step with 5% goat serum was introduced to the initial protocol. In the second experiment the additional blocking step was combined with an increased dilution of the secondary antibody to further reduce potential nonspecific binding. The results obtained from the control skin samples is shown in Figure 17.

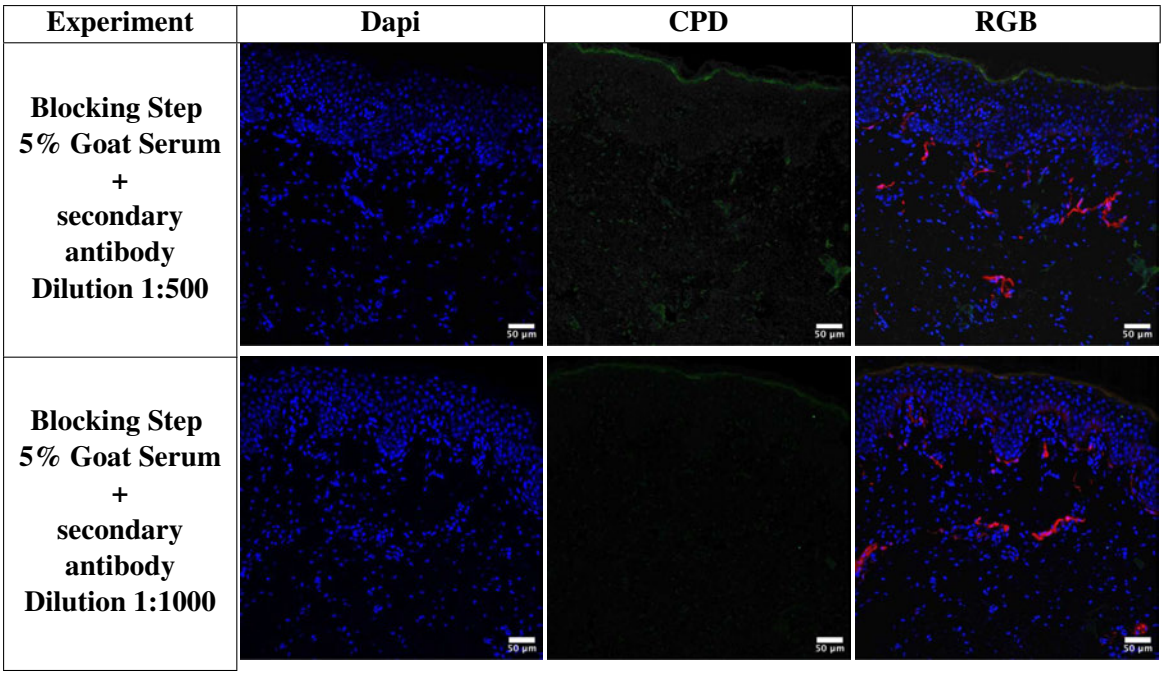


Figure 17. Optimization of the initial CPD and NGFRp75 staining protocol revealed no false-positive staining. Representative images of the non-irradiated control foreskin biopsy following immunofluorescence staining for CPD and NGFRp75. An additional blocking step with 5% goat serum was performed (row 1). And in addition to that the secondary antibody was diluted 1:1000 instead of 1:500 (row 2). Nuclei were stained with DAPI which is shown in blue, CPD is shown in green, and NGFRp75 is shown in red. The RGB image shows the overlay of all three channels (red, green and blue).

Figure 17 shows that the control foreskin samples no longer exhibited the false-positive signals observed in Figure 16. This finding was consistent throughout the entire tissue sections. Based on these results, the protocol was modified by incorporating the additional blocking step immediately before incubation with the secondary antibodies. However, increasing the dilution of the secondary antibody did not provide a significant improvement compared with the use of the additional blocking step alone. Thus, all subsequent staining procedures were performed with only an additional blocking step and the initial secondary antibody dilution of 1:500.

5.4.2 UV-induced DNA damage in NGFRp75-positive cells

The modified DNase-I staining protocol was applied to skin biopsies obtained from three different anatomical sites: juvenile foreskin, adult axillary and thigh skin. For each skin sample, both a non-irradiated control and a UV-irradiated sample were analyzed. The staining was performed to determine whether UV irradiation induces CPD formation in DSCs and to compare the effects of UVA and UVB irradiation on CPD induction. In particular, differences in the extent, distribution, and persistence of UV-induced DNA damage between both irradiation conditions were assessed. To access DNA repair over time, samples were collected and frozen at different time points (0 h, 24 h, 48 h) following irradiation.

5.4.2.1 UVA-induced DNA Damage

The skin biopsy samples were irradiated with a UVA dose of 140 kJ/m^2. All skin samples were exposed to the same irradiation dose. Control samples were incubated for the same duration and

under comparable temperature conditions as the irradiated samples but were not exposed to UVA radiation. The results obtained from the axillary skin, the thigh skin and the juvenile foreskin biopsies are presented in Figures 18 – 20.

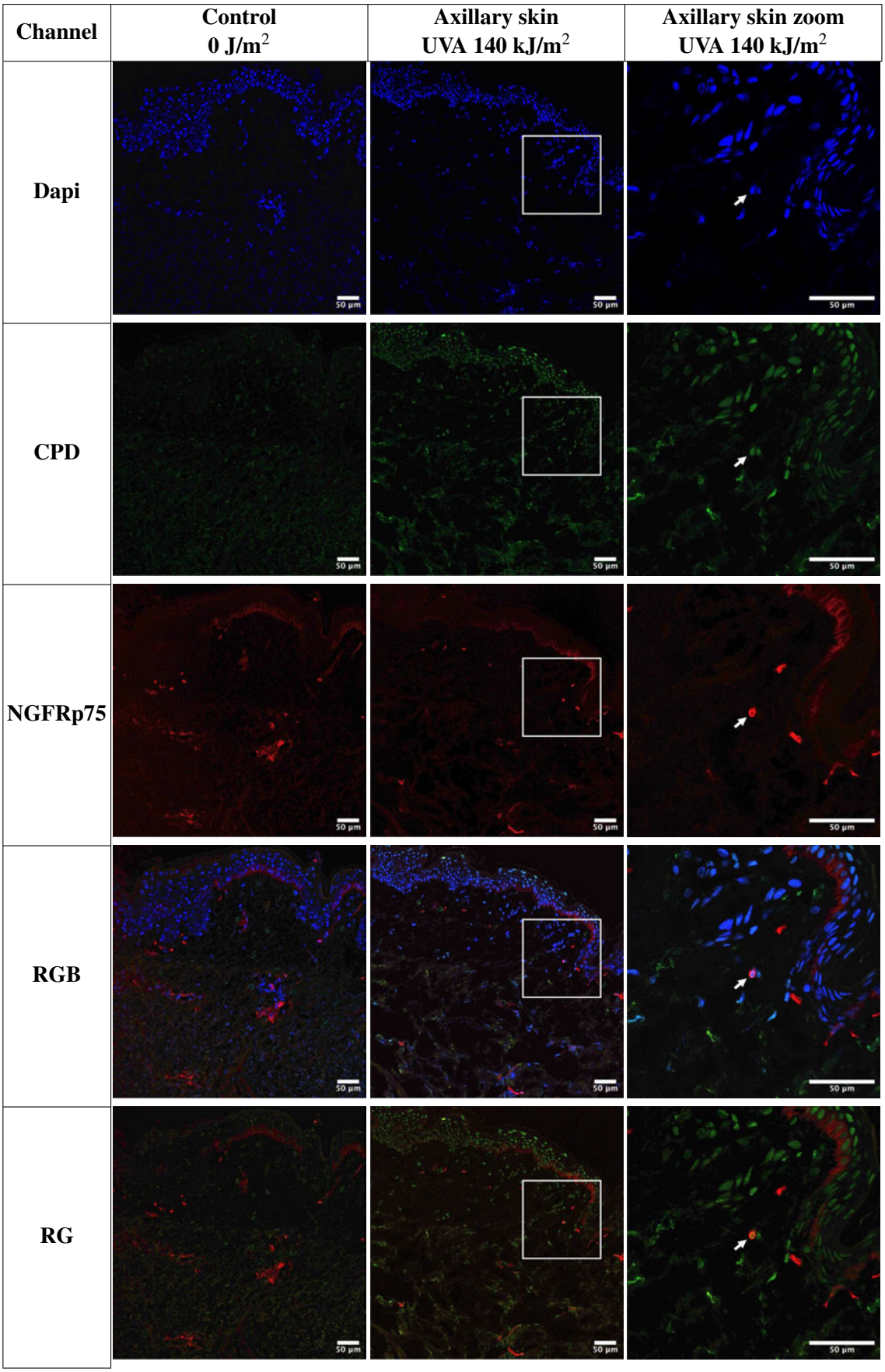


Figure 18. Axillary skin sections stained for CPD and NGFRp75 after 0 J/m^2 (control) and 140 kJ/m^2 UVA irradiation. Representative images of axillary skin following immunofluorescence staining for CPDs and NGFRp75, showing a double-positive cell. Nuclei were stained with DAPI, which is shown in blue, CPDs are shown in green, and NGFRp75 is shown in red. The RG image represents the merged red and green channels, while the RGB image shows the overlay of all three channels (red, green and blue). Arrow = CPD- and NGFRp75-positive cell.

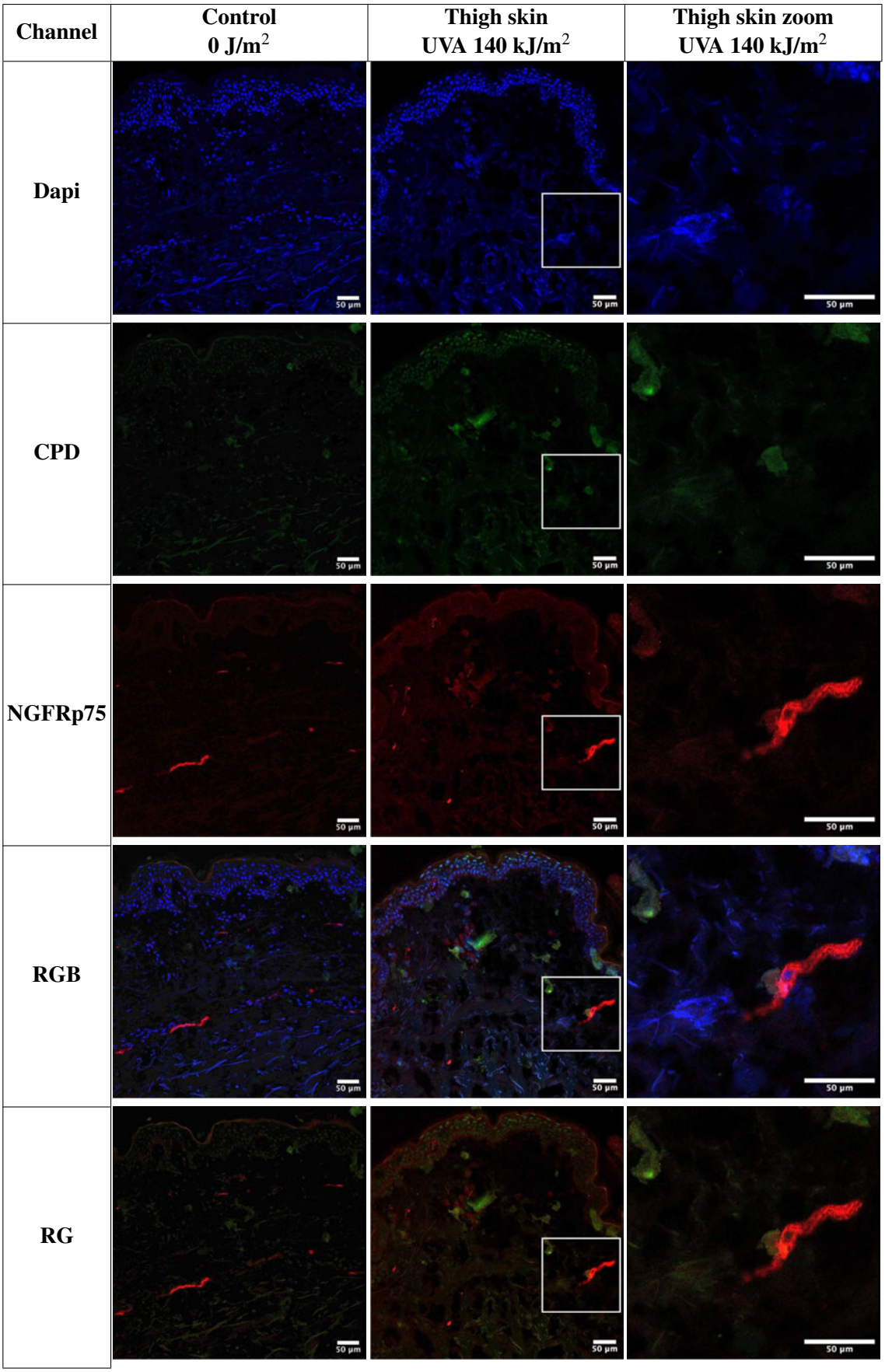


Figure 19. Thigh skin sections stained for CPDs and NGFRp75 after after 0 J/m^2 (control) and 140 kJ/m^2 UVA irradiation. Representative images of thigh skin following immunofluorescence staining for CPD and NGFRp75. Nuclei were stained with DAPI, which is shown in blue, CPDs are shown in green, and NGFRp75 is shown in red. The RG image represents the merged red and green channels, while the RGB image shows the overlay of all three channels (red, green and blue).

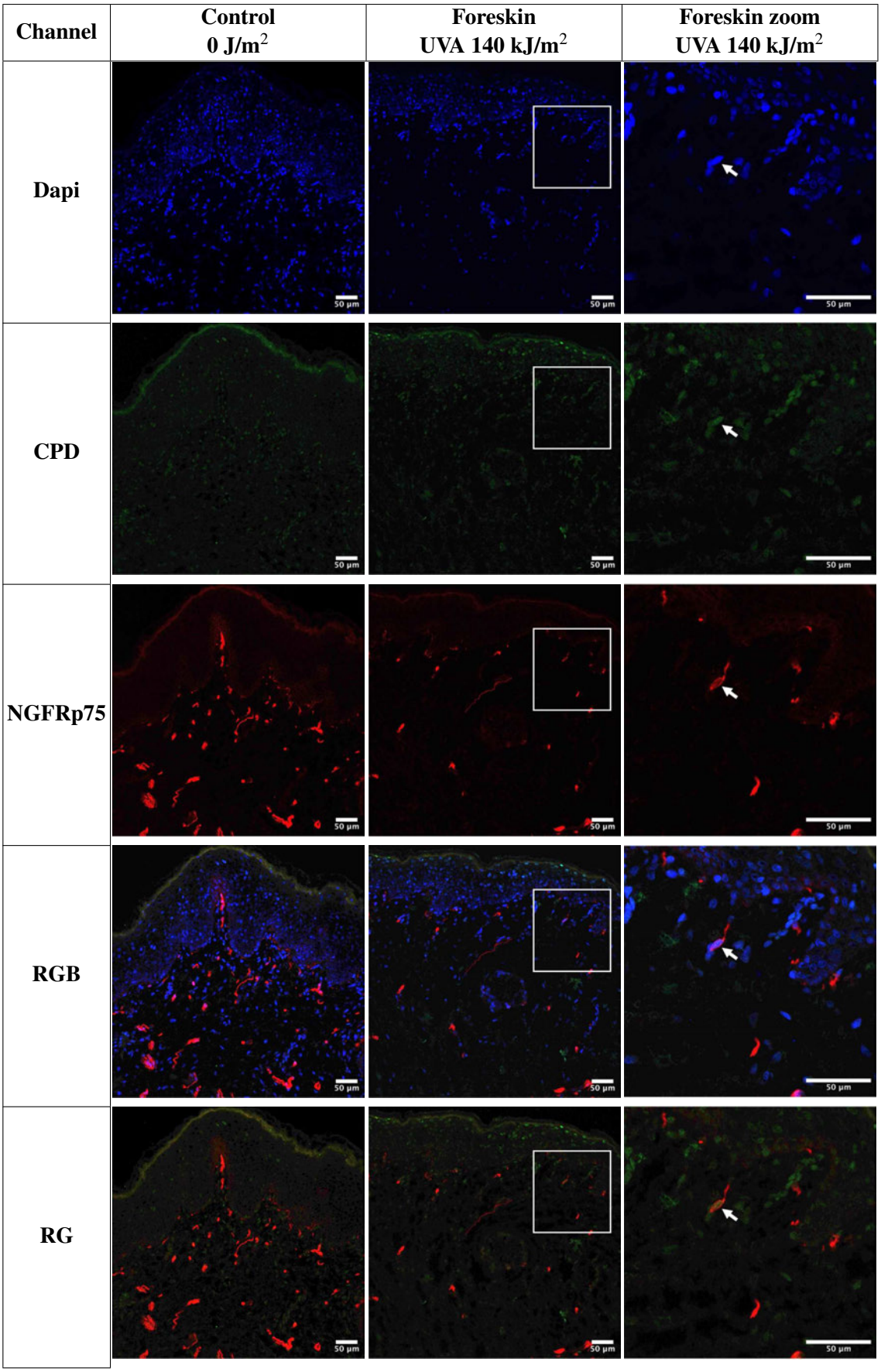


Figure 20. Juvenile foreskin sections stained for CPDs and NGFRp75 after 0 J/m^2 (control) and 140 kJ/m^2 UVA irradiation. Representative images of juvenile foreskin following immunofluorescence staining for CPD and NGFRp75, shwowing a double-positive cell. Nuclei were stained with DAPI which is shown in blue, CPD is shown in green, and NGFRp75 is shown in red. The RG image represents the merged red and green channels, while the RGB image shows the overlay of all three channels (red, green and blue). Arrow = CPD- and NGFRp75-positive cell.

The skin biopsy shown in Figure 18 was obtained from adult axillary skin. The non-irradiated control sample did not show any unusual staining signals. DAPI nuclear staining was successful, allowing clear visualization of cellular nuclei throughout the tissue section. In the irradiated sample, UVA exposure induced DNA damage primarily in the upper epidermis, with occasional CPD-positive nuclei also observed in the upper dermis. The CPD signal was clearly detectable and distinguishable from the background staining. In addition, NGFRp75 staining was successful, revealing several NGFRp75-positive cells within the tissue section. In a magnified view of the image, an NGFRp75-positive cell showed a detectable CPD signal, indicating UVA-induced DNA damage in this cell (Figure 18, 'Axillary skin zoom', arrow).

Figure 19 presents the results obtained from adult thigh skin biopsies. DAPI Nuclear staining was successful in all tissue sections, allowing clear visualization of cellular nuclei. In the non-irradiated control sample, several NGFRp75-positive cells were observed within the dermis. The CPD staining revealed a small number of artifacts that were also labeled by the secondary antibody. In addition, collagen and other dermal fibers within the dermis showed autofluorescence. As these signals were not localized to cell nuclei, they were not considered indicative of CPD formation. In the irradiated sample, CPD-positive nuclei were detected mainly in the upper layers of the epidermis, similar to the pattern observed in the axillary skin sample. The staining artifacts were also present in the irradiated tissue sections but could be readily distinguished from the specific nuclear CPD signal. NGFRp75-positive cells were likewise identified within this tissue section. However, none of the observed NGFRp75-positive cells showed detectable CPD staining.

Figure 20 shows the immunofluorescence staining of DAPI, CPDs and NGFRp75 in juvenile foreskin tissue sections. DAPI staining was successful in all sections and provided clear visualization of cellular nuclei. In the non-irradiated control sample, a weak CPD-positive background signal was observed, which was evenly distributed throughout the entire section. Numerous NGFRp75-positive cells were detected in the foreskin tissue, particularly in the control sample. These cells were located beneath the basement membrane and within the dermis. NGFRp75-positive cells were also observed in the irradiated sample. Although UVA-induced CPDs were mainly confined to the upper epidermal layers, a cell positive for NGFRp75 and CPD was observed (Figure 20, arrow).

5.4.2.2 UVB-induced DNA Damage

The same skin biopsy samples were also irradiated with a UVB dose of 1500 J/m^2. For each irradiated sample, a corresponding non-irradiated control sample was included. Control samples were incubated for the same duration and under comparable temperature conditions as the irradiated samples but were not exposed to the UVB radiation. The results obtained after the immunofluorescence staining of axillary skin, thigh skin and juvenile foreskin samples are presented in Figures 21 – 23.

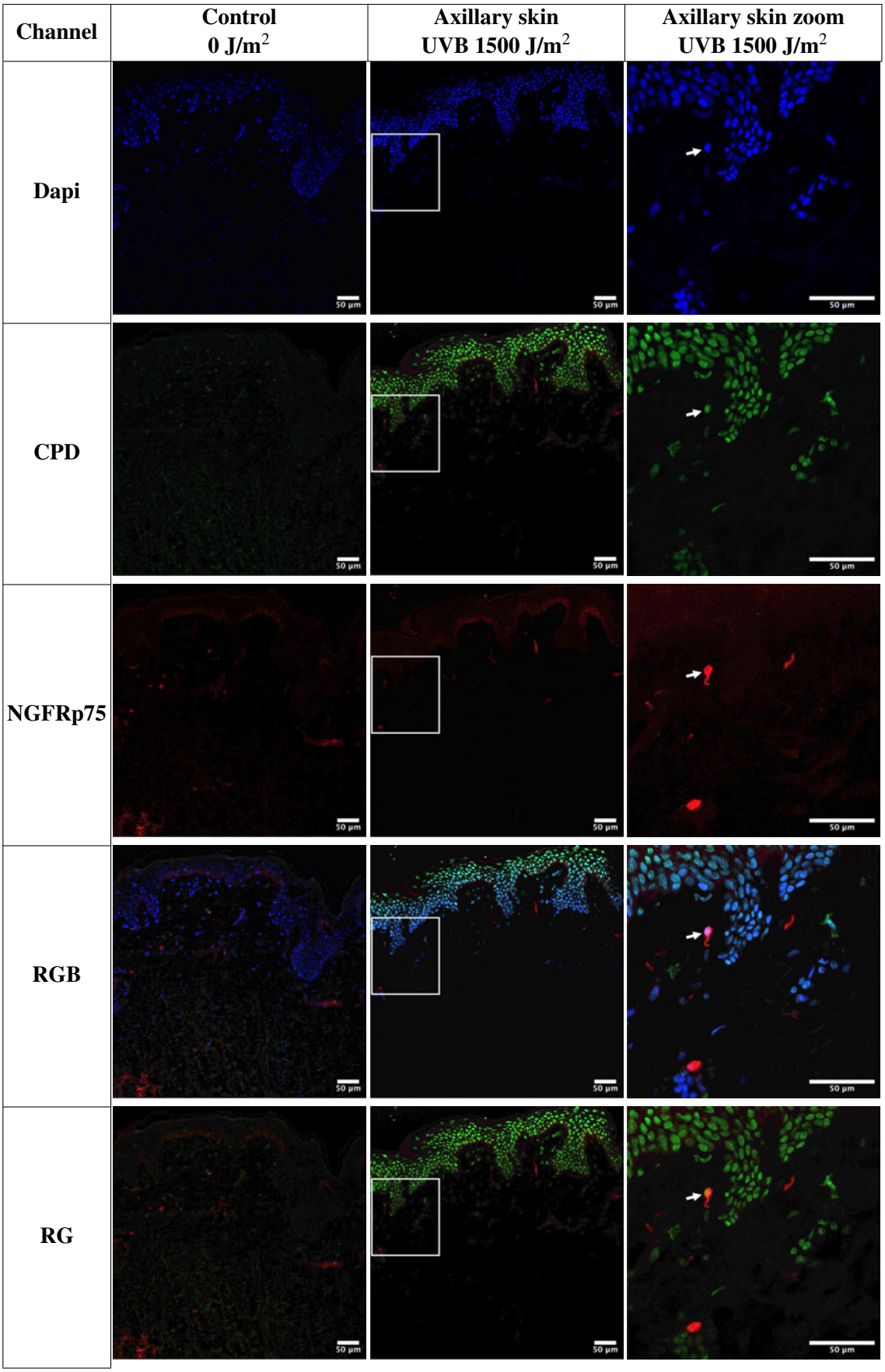


Figure 21. Axillary skin sections stained for CPDs and NGFRp75 after 0 J/m^2 (control) and 1500 J/m^2 UVB irradiation. Representative images of axillary skin following immunofluorescence staining for CPDs and NGFRp75, showing a double-positive cell. Nuclei were stained with DAPI, which is shown in blue, CPDs are shown in green, and NGFRp75 is shown in red. The RG image represents the merged red and green channels, while the RGB image shows the overlay of all three channels (red, green and blue). Arrow = CPD- and NGFRp75-positive cell.

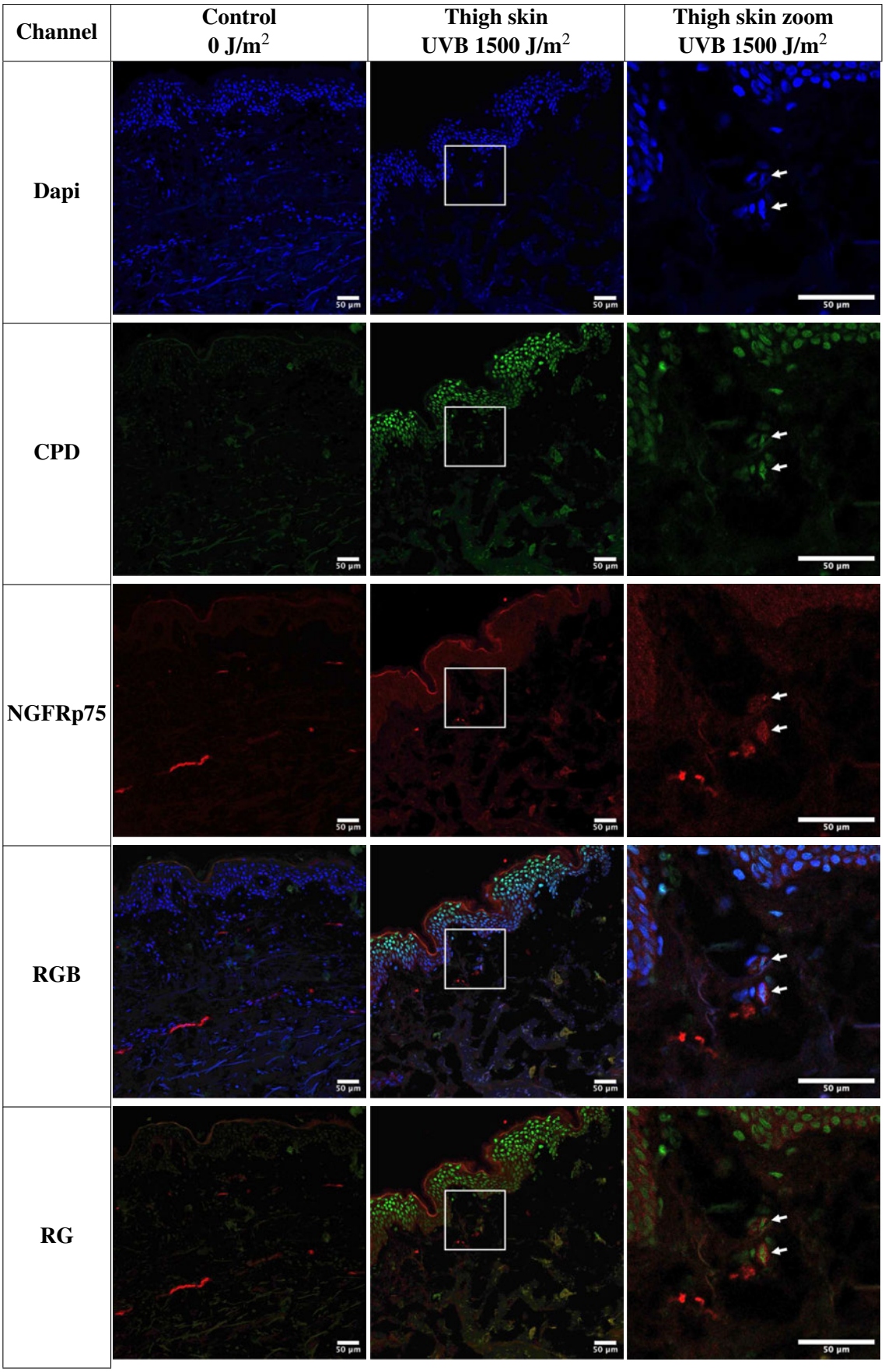


Figure 22. Thigh skin sections stained for CPDs and NGFRp75 after 0 J/m^2 (control) and 1500 J/m^2 UVB irradiation. Representative images of thigh skin following immunofluorescence staining for CPDs and NGFRp75, showing double-positive cells. Nuclei were stained with DAPI, which is shown in blue, CPDs are shown in green, and NGFRp75 is shown in red. The RG image represents the merged red and green channels, while the RGB image shows the overlay of all three channels (red, green and blue). Arrow = CPD- and NGFRp75-positive cell.

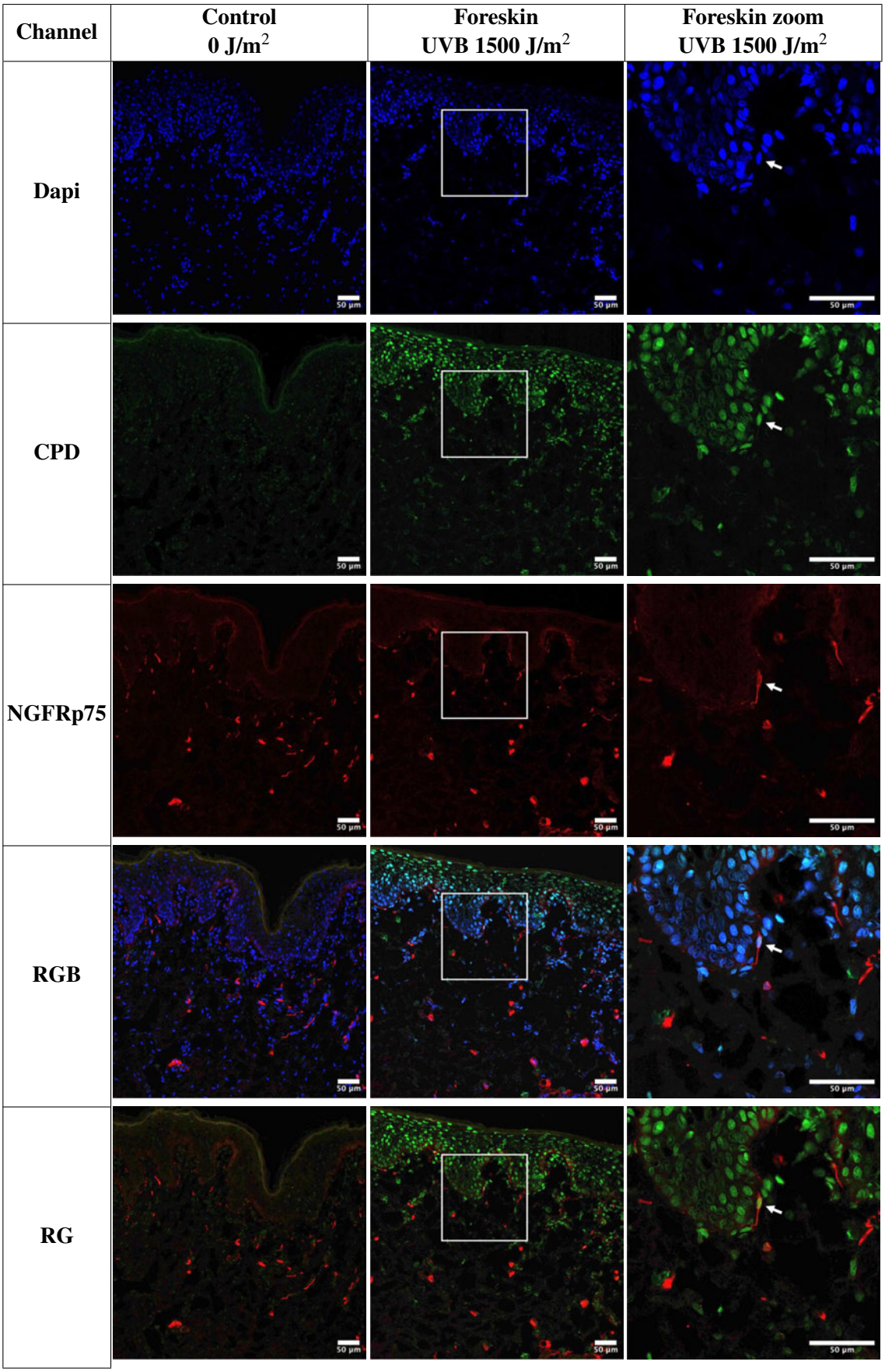


Figure 23. Juvenile foreskin sections stained for CPDs and NGFRp75 after 0 J/m^2 (control) and 1500 J/m^2 UVB irradiation. Representative images of juvenile foreskin following immunofluorescence staining for CPDs and NGFRp75, showing a double-positive cell. Nuclei were stained with DAPI, which is shown in blue, CPDs are shown in green, and NGFRp75 is shown in red. The RG image represents the merged red and green channels, while the RGB image shows the overlay of all three channels (red, green and blue). Arrow = CPD-and NGFRp75-positive cell.

Figure 21 presents the control sample and the UVB-irradiated axillary skin sample following immunofluorescence staining. As expected, NGFRp75-positive cells were detected within the dermis with additional staining in parts of the basal layer. In the irradiated sample strong CPD signals extended from the epidermis into the upper dermis with signal intensity gradually decreasing towards the deeper tissue layers. Most nuclei within the exposed region displayed detectable CPD staining. Several NGFRp75-positive cells were located directly beneath the epidermis. In the magnified view, a cell was double-positive for NGFRp75 and CPDs (Figure 21, 'Axillary skin zoom', arrow). NGFRp75-positive cells in close proximity to the basal layer showed distinct CPD-positive signals.

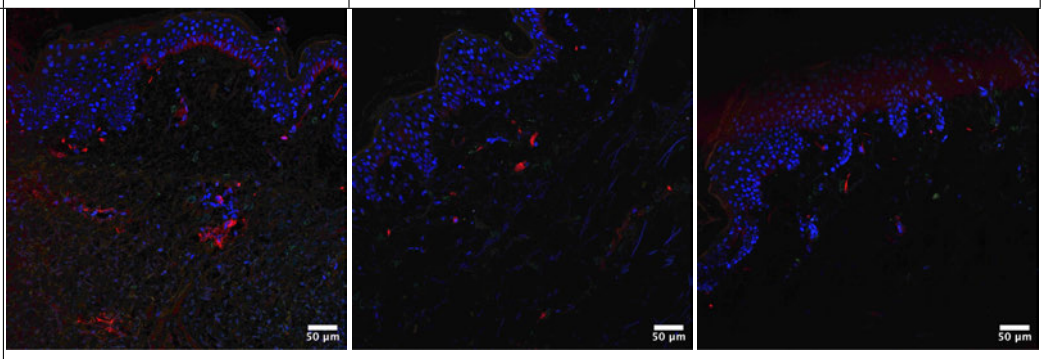
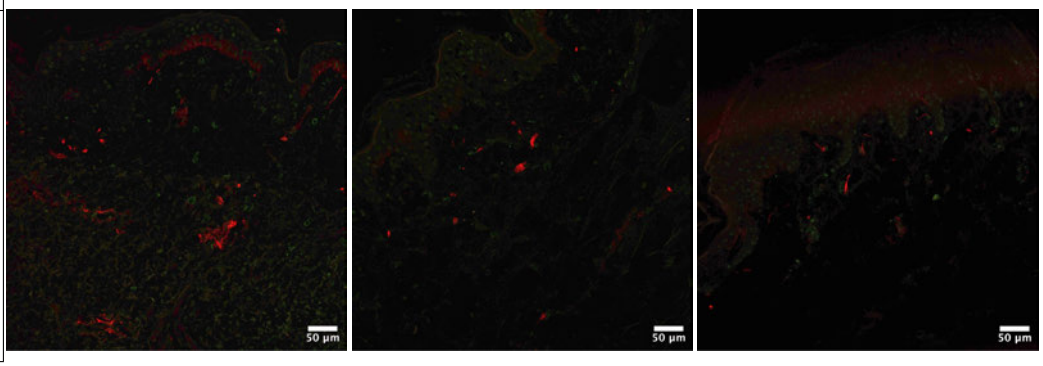
Similar observations were made in the adult thigh skin sample shown in Figure 22. However, skin sections contained several artifacts outside the cell nuclei that were labeled by the secondary antibodies and were therefore excluded from further analysis. Dermal fibers were also clearly visible due to their intrinsic autofluorescence. As observed in axillary skin, CPD signal intensity gradually decreased towards the deeper tissue layers with the strongest CPD signal detected in the superficial epidermal layers and progressively diminishing towards the dermis. Regions located within skin folds showed weaker CPD signals than the surrounding tissue. NGFRp75 staining was successful revealing positive signals in parts of the basal layer as well as beneath the epidermis. In the magnified image these cells displayed clear CPD positivity (Figure 22, 'Thigh skin zoom', arrow). These cells were located beneath an epidermal protrusion with strong CPD signal intensity.

These CPD and NGFRp75 double-positive cells were also observed in foreskin (Figure 23, 'Foreskin zoom', arrow). As previously noted, foreskin samples contained substantially more NGFRp75-positive cells than the axillary and thigh skin samples. CPD signals were distributed throughout the epidermis and remained detectable within the upper dermis. Due to the high abundance of NGFRp75-positive cells, numerous cells co-expressing NGFRp75 and CPD were identified, particularly in the region immediately beneath the basal layer. A representative double-positive cell is shown in the magnified image. The control sample did not show any unusual artifacts although weak nuclear background signal was detected in the CPD channel. In addition to the NGFRp75-positive cells in the dermis, weak NGFRp75 staining was also observed within the basal layer.

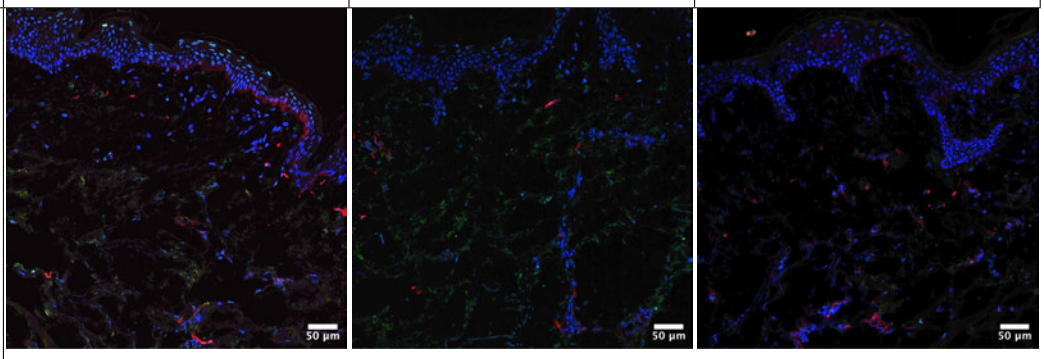
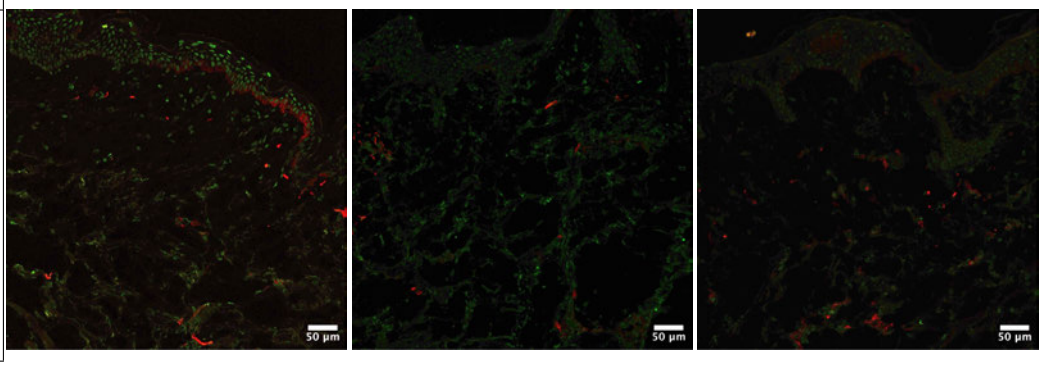
5.4.2.3 DNA Damage Repair after 24 and 48 Hours

To assess the repair of UV-induced CPDs, all investigated skin biopsy samples were incubated for an additional 24 and 48 hours after irradiation prior to freezing. The results obtained after 24 and 48 hours of post-irradiation incubation are shown in the following figures.

A	Axillary skin - Control

Channel	T0	T24	T48
RGB			
RG			

B	Axillary skin - 140 kJ/m^2 UVA

Channel	T0	T24	T48
RGB			
RG			

C	Axillary skin - 1500 J/m^2 UVB

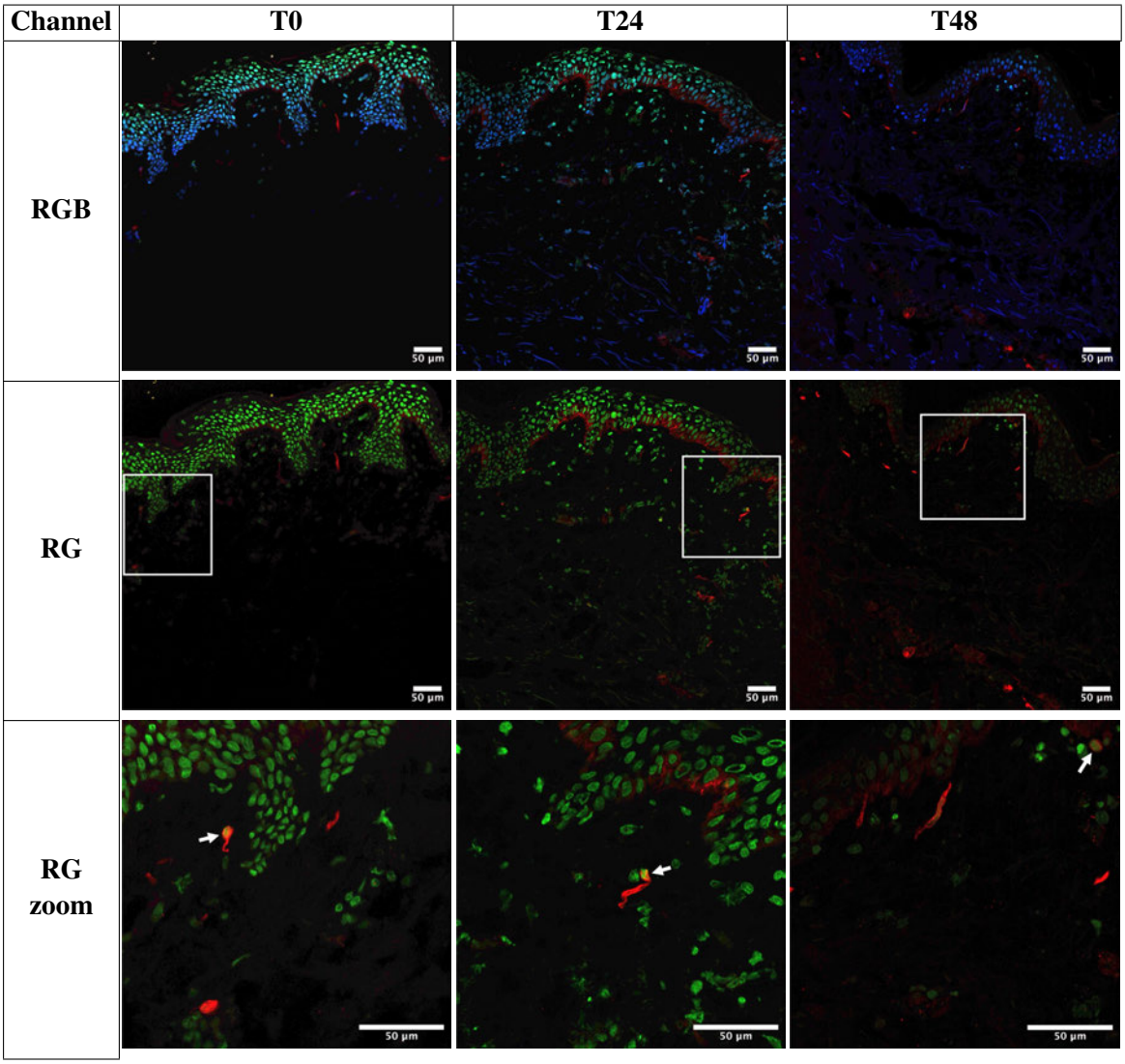
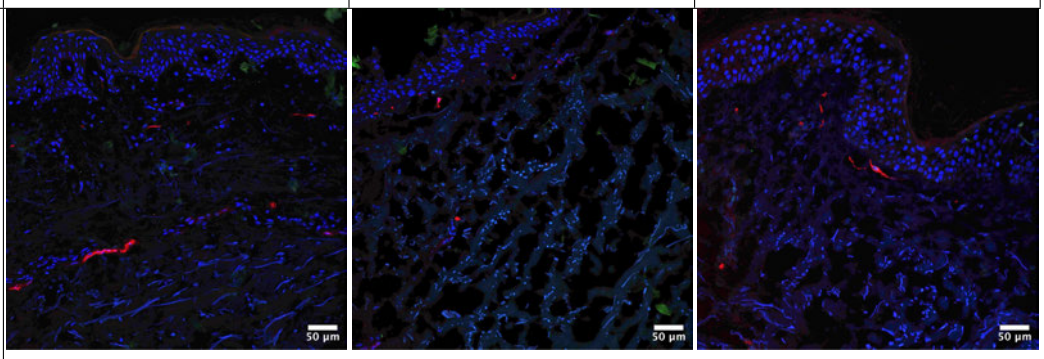
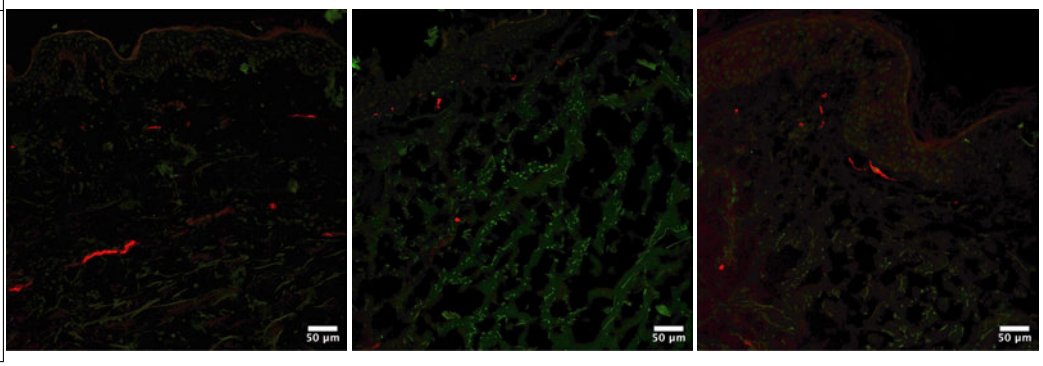
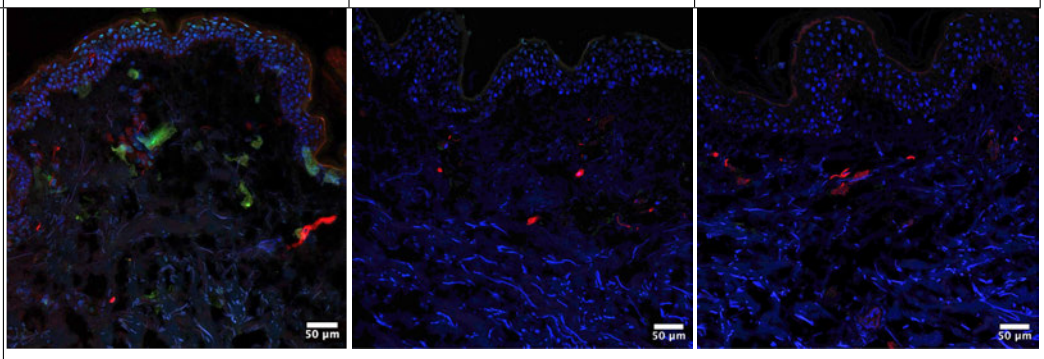
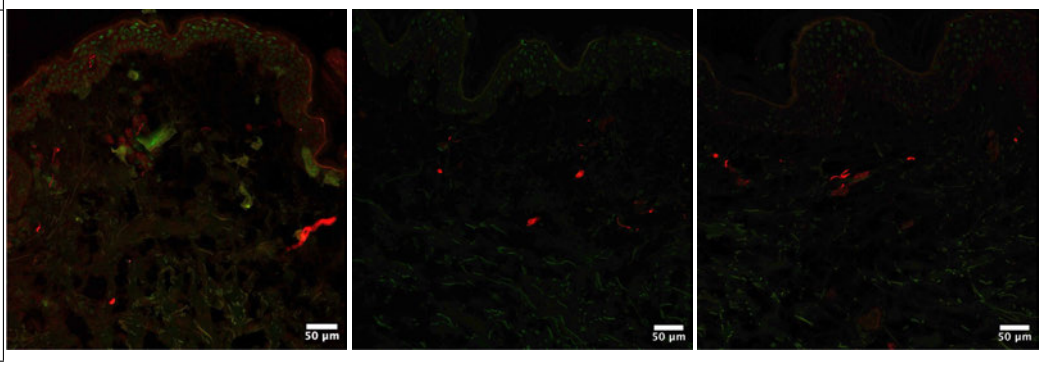


Figure 24. Axillary skin sections stained for CPDs and NGFRp75 at time points T0, T24, and T48 after UVA and UVB irradiation. Representative images of non-irradiated axillary skin (A), and axillary skin following UVA (B) or UVB (C) irradiation at time points T0, T24 and T48 and immunofluorescence staining for CPD and NGFRp75. The images show cells positive for NGFRp75 and CPD at all time points. Nuclei were stained with DAPI, which is shown in blue, CPDs are shown in green, and NGFRp75 is shown in red. The RG image represents the merged red and green channels, while the RGB image shows the overlay of all three channels (red, green and blue). Arrow = CPD-and NGFRp75-positive cell.

A	Thigh skin - Control

Channel	T0	T24	T48
RGB			
RG			

B	Thigh skin - 140 kJ/m^2 UVA

Channel	T0	T24	T48
RGB			
RG			

C	Thigh skin - 1500 J/m^2 UVB

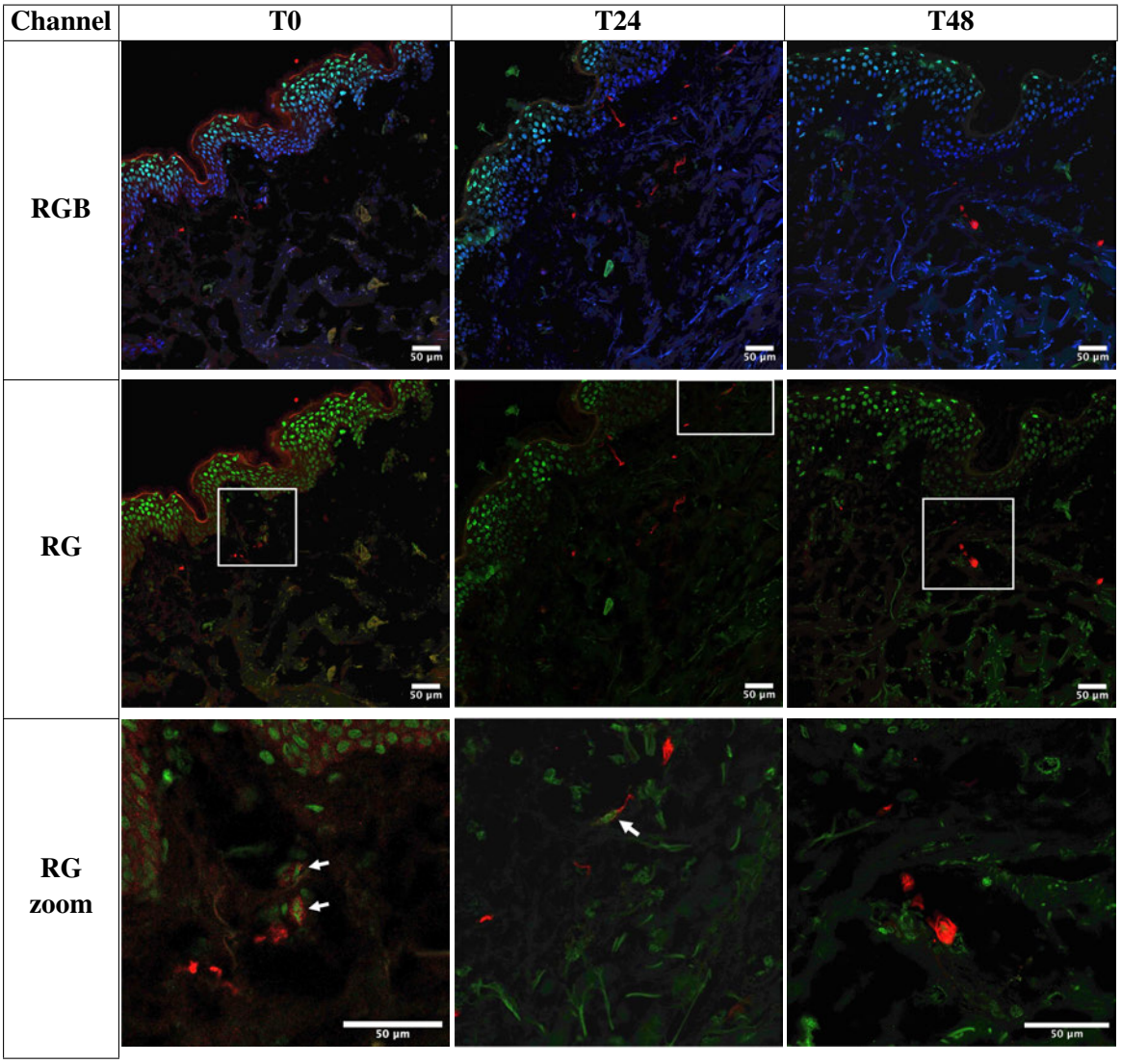
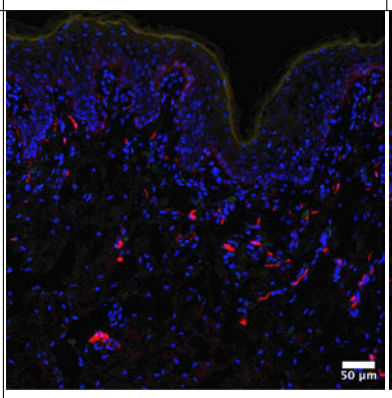
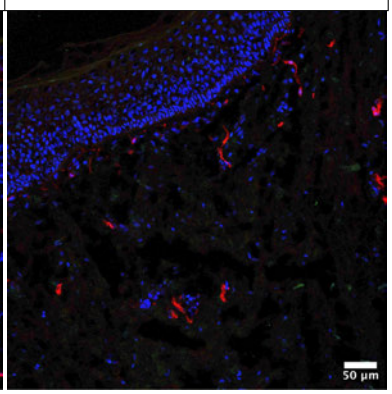
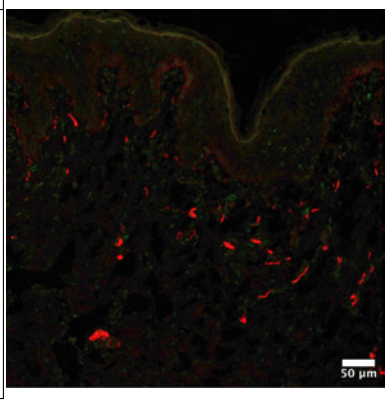
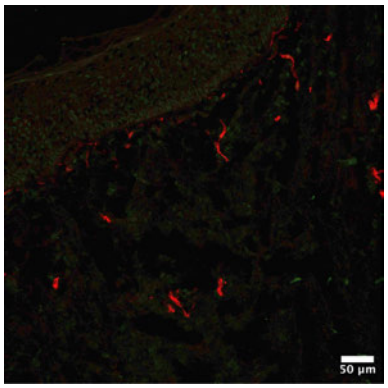
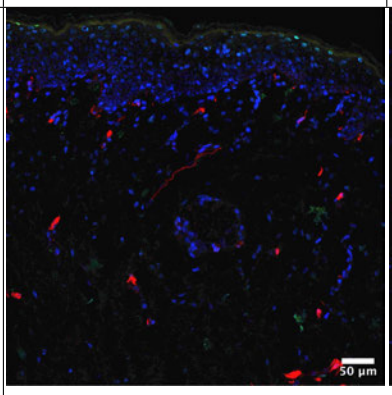
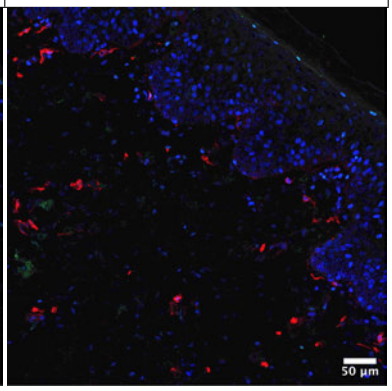
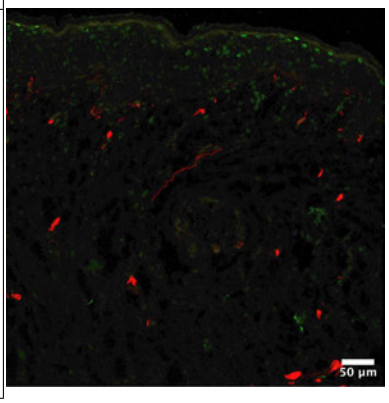
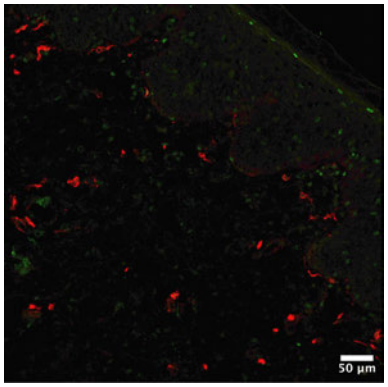


Figure 25. Thigh skin sections stained for CPDs and NGFRp75 at time points T0, T24, and T48 after UVA and UVB irradiation. Representative images of non-irradiated thigh skin (A), and thigh skin following UVA (B) or UVB (C) irradiation at time points T0, T24 and T48 and immunofluorescence staining for CPDs and NGFRp75. Time points T0 and T24 show NGFRp75 and CPD double-positive cells. Nuclei were stained with DAPI, which is shown in blue, CPDs are shown in green, and NGFRp75 is shown in red. The RG image represents the merged red and green channels, while the RGB image shows the overlay of all three channels (red, green and blue). Arrow = CPD-and NGFRp75-positive cell.

A	Foreskin - Control

Channel	T0	T24
RGB		
RG		

B	Foreskin - 140 kJ/m^2 UVA

Channel	T0	T24
RGB		
RG		

C	Foreskin - 1500 J/m^2 UVB

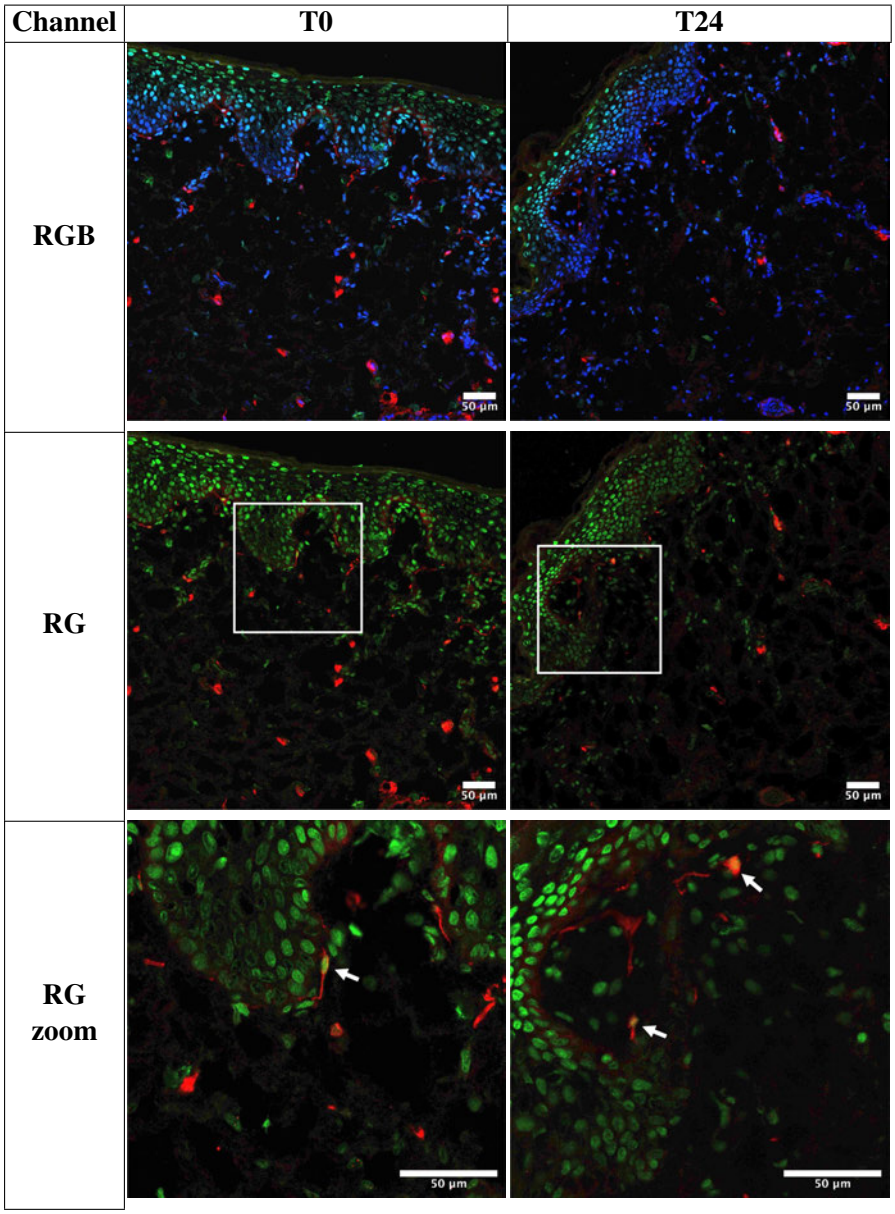


Figure 26. Foreskin sections stained for CPDs and NGFRp75 at time points T0 and T24 after UVA and UVB irradiation. Representative images of non-irradiated foreskin (A), and foreskin following UVA (B) or UVB (C) irradiation at time points T0 and T24 after immunofluorescence staining for CPDs and NGFRp75. Double-positive cells are shown in both time points. Nuclei were stained with DAPI, which is shown in blue, CPDs are shown in green, and NGFRp75 is shown in red. The RG image represents the merged red and green channels, while the RGB image shows the overlay of all three channels (red, green and blue). Arrow = CPD- and NGFRp75-positive cell.

Figure 24 illustrates the temporal dynamics of CPD repair following UVA and UVB irradiation. The time points analyzed were immediately after irradiation (T0), as well as 24 hours (T24) and 48 hours (T48) post-irradiation. The control samples showed comparable background signals at all time points, indicating that the background staining remained stable throughout the incubation period (Figure 24A). In all tissue sections, individual NGFRp75-positive cells were observed within the dermis, mainly in close proximity to the epidermis. Following UVA irradiation CPD signal decreased over time. After 24 hours, the majority of CPD lesions were removed, particularly within the epidermis

and no clear CPD-positive nuclei remained after 48 hours. In contrast, UVB irradiation resulted in substantially higher initial CPD levels at T0. Although CPD signal decreased over time, CPD-positive nuclei remained detectable after 24 hours, and further reduction was observed between T24 and T48. Notably, even after 48 hours of incubation, NGFRp75-positive cells showing detectable CPD signal were still present within the tissue sections (Figure 24C, T48, arrow).

Figure 25 shows the temporal dynamics of CPD lesions in thigh skin samples. The control samples showed only weak background staining at all analyzed time points, while dermal fibers exhibited intrinsic autofluorescence. NGFRp75-positive cells were detected in all analyzed tissue sections. Following UVA irradiation, CPD signal intensity decreased over time, similar to the pattern previously described for axillary skin. After 24 hours of incubation, CPD-positive nuclei were still detectable, particularly within the most superficial layers of the epidermis. After 48 hours, the CPD signal had decreased further, and only weak residual staining remained visible. In contrast, substantial CPD lesions were still detectable 48 hours after UVB irradiation. Cells positive for CPD and NGFRp75 were observed until T24 (arrows). After 48 h, the number of CPD-positive nuclei and the intensity of the CPD signal were reduced, but did not disappear completely.

Figure 26 shows the double immunofluorescence staining of CPDs and NGFRp75 in foreskin biopsies at T0 and T24. The tissue morphology remained largely unchanged at T0 and T24. However, after 48 hours of incubation, the foreskin tissue appeared swollen, resulting in a stretched epidermis with reduced nuclear density and loss of structural integrity (data not shown). This sample could not be reliably evaluated and was therefore excluded from further analysis. The control samples at T0 and T24 showed only weak background staining in the CPD channel. Numerous NGFRp75-positive cells were observed in all tissue sections. These cells were distributed throughout the upper dermis and along the basal layer. Following UVA irradiation, CPD-positive nuclei were detected within the epidermis. The intensity and extent of the CPD signal decreased with time. After 24 hours, CPD-positive nuclei remained barely detectable. UVB irradiation resulted in extensive CPD formation, extending from the epidermis into the dermis. A slight reduction in CPD signal was observed after 24 hours of incubation. The uniformity of the CPD staining pattern and the extent of CPD-positive signals in the dermis were slightly reduced compared to T0. However, intensely CPD-positive nuclei remained visible throughout the section. Several cells positive for CPDs and NGFRp75 were still observed after 24 hours (Figure 26C, T24, arrow).

In summary, human skin sections were successfully stained using the optimized immunofluorescence staining to investigate UV-induced CPDs. NGFRp75-positive cells were detected within the upper dermis, with a higher abundance observed in juvenile foreskin samples compared with adult skin samples. UV-irradiation resulted in the induction of CPDs, with the stronger signal observed after UVB irradiation, while UVA irradiation induced a weaker CPD staining. Although epidermal cells showed the most pronounced DNA damage response, UV-induced CPDs were also detected in dermal NGFRp75-positive cells. Following UVA irradiation, CPDs were almost completely removed within the investigated time period, whereas UVB-induced CPDs remained clearly detectable after 48 hours.

6 Discussion

Evaluation and Limitations of Markers for the Identification of Dermal Stem Cells in Human Skin

To date, no marker has been identified that specifically and exclusively labels extrafollicular DSCs in human skin. However, several proteins have been reported to be expressed by DSCs and can be used to distinguish them from other stem cell populations. Among these, NGFRp75 and Nestin are the most commonly described markers of DSCs [28, 29]. In addition, SOX10, a transcription factor associated with neural crest-derived cells, has also been suspected to be expressed in DSCs. However, SOX10 is not specific to DSCs, as it is also expressed by other neural crest-derived cell populations, including melanocytes and Schwann cells [52]. Therefore, these markers were combined and evaluated for the identification of DSCs in human skin sections. As NGFRp75 has been described as the most consistently expressed marker of DSCs, it was included in all co-immunofluorescence stainings. NGFRp75 is a low-affinity nerve growth factor receptor located on the cell surface. In addition to DSCs, it is also expressed by several neural cell populations within the skin, particularly Schwann cells [56]. Consequently, the detection of NGFRp75 alone is not sufficient to clearly identify DSCs in skin tissue. Pure DSC cultures were therefore used as positive controls to validate the staining procedures (Figure 4, Figure 8, Figure 10). Co-staining for SOX10 and NGFRp75 demonstrated a clear double-positive signal in every cell of the DSC cultures, confirming that cultured DSCs consistently express both markers. In both adult axillary skin and juvenile foreskin sections, cells positive for SOX10 and NGFRp75 were detected (Figure 5, Figure 6). The higher number of double-positive cells observed in juvenile foreskin may be associated with the enhanced regenerative capacity that has been observed in neonatal skin [57]. In both samples within the upper dermis, the majority of NGFRp75-positive cells also expressed SOX10, suggesting that SOX10 may represent a useful marker for the identification of DSCs. As expected, SOX10 additionally labeled melanocytes located along the epidermal basement membrane. These cells were negative for NGFRp75, consistent with the current understanding that mature melanocytes lose NGFRp75 expression during differentiation and contact with epidermal keratinocytes [29]. In contrast, several structures within the foreskin dermis exhibited NGFRp75 expression in the absence of SOX10 expression (Figure 7 'Foreskin dermis II'). Based solely on immunofluorescence staining, the identity of these structures could not be determined with certainty. To further characterize these structure, H&E staining was performed. Since all cells in the DSC control cultures exhibited double-positive staining, these NGFRp75-positive/SOX10-negative structures are unlikely to represent typical DSCs and may instead correspond to other neural or stromal cell populations [58]. Another prominent structure within the dermis, morphologically consistent with eccrine sweat glands, was surrounded by numerous SOX10- and NGFRp75-positive cells. This observation is in agreement with the findings of Zancanaro et al. [59], who demonstrated the presence of small nerve bundles in close proximity to human eccrine sweat glands. Consequently, in this case these SOX10- and NGFRp75-positive cells most likely represent Schwann cells associated with the peripheral nerve fibers rather than DSCs (Figure 7 ('Foreskin dermis I')).

Another known DSC marker is Nestin. Nestin was evaluated in combination with NGFRp75 using pure DSC cultures as positive controls. Similar to the SOX10 staining, all cultured DSCs showed

robust co-expression of Nestin and NGFRp75 (Figure 8), confirming that Nestin is expressed by DSCs, in agreement with previous studies [29]. In juvenile foreskin sections, Nestin staining revealed considerable background fluorescence throughout both the epidermis and dermis. Although most NGFRp75-positive cells also exhibited Nestin expression, numerous additional NGFRp75-negative cells were labeled by the anti-Nestin antibody. The extensive background staining substantially reduced the contrast between positive cells and surrounding tissue, making the reliable identification of Nestin-positive cells difficult. However, Nestin expression is not restricted to neural stem cells. In hairless skin, mesenchymal stem cell populations have been described as additionally expressing Nestin [60]. Therefore, the widespread Nestin positivity observed in the skin sections most likely reflects the limited specificity of this marker rather than the exclusive presence of DSCs. In addition, the large number of Nestin-positive cells suggests that the antibody may show a certain degree of non-specific binding. This effect may be further enhanced by the use of a polyclonal antibody, which generally recognizes multiple epitopes and therefore tends to produce higher background staining than monoclonal antibodies. Consequently, Nestin does not appear to be sufficiently specific for the reliable identification of DSCs in human skin.

As a third marker, co-immunofluorescence staining of βIII-Tubulin and NGFRp75 was performed. βIII-Tubulin was selected to visualize neuronal structures within the skin and thereby facilitate the distinction between peripheral nerve cells and DSCs. Surprisingly, the positive control consisting of pure DSC cultures exhibited clear co-expression of NGFRp75 and βIII-Tubulin in all cells (Figure 10). This finding was unexpected, as βIII-Tubulin is generally regarded as a marker of differentiated neurons, whereas undifferentiated DSCs would not be expected to express βIII-Tubulin [33]. The unexpected expression of βIII-Tubulin may reflect the neural crest origin of DSCs and their potential to differentiate into neuronal lineages, demonstrating the multipotent differentiation capacity of DSCs [29]. A comparable staining was observed in the juvenile foreskin sections (Figure 11). Most NGFRp75-positive cells also expressed βIII-Tubulin. In addition, a population of βIII-Tubulin-positive but NGFRp75-negative cells was detected, most likely representing mature neuronal structures that no longer express NGFRp75. These findings indicate that βIII-Tubulin cannot be used as an exclusion marker for neuronal structures when attempting to identify DSCs within human skin, as DSCs themselves appear to express this protein under the culture conditions used in this study.

Hematoxylin and eosin (H&E) staining was then performed to allow further interpretation of the immunofluorescence images by providing more detailed information on tissue morphology. The staining enabled the identification of characteristic anatomical structures based on their cellular organization and architecture. In particular, eccrine sweat glands could be readily identified, allowing several immunofluorescent signals to be assigned to defined tissue structures. Without the corresponding H&E sections, the interpretation of these structures would have been considerably more challenging. Nevertheless, the quality of the tissue morphology was partially compromised by the freezing procedure used during sample preparation. The skin biopsies were frozen at approximately –70 °C, resulting in relatively slow freezing of the tissue. Slow freezing promotes the formation of large intracellular and extracellular ice crystals, which disrupt cellular membranes and alter the native tissue architecture. Consequently, the dermis appeared structurally loose in several sections, making the identification of certain skin structures more difficult (Figure 12b, 12c, 13c). To improve tissue preservation in future studies, rapid freezing using nitrogen or dry ice should be considered. It sub-

stantially reduces ice crystal formation, thereby preserving tissue morphology, cellular integrity and antigen distribution, ultimately improving the quality of both histological and immunofluorescence analyses.

Overall, none of the investigated markers enabled the unequivocal identification of DSCs within human skin. Among the tested combinations, co-staining of SOX10 with directly conjugated NGFRp75 yielded the most promising results. Since SOX10 is localized to the nucleus, it simplifies the assignment of the membrane-associated NGFRp75 signal to individual cells, particularly in regions with extensive NGFRp75-positive staining. However, both SOX10 and NGFRp75 are also expressed by Schwann cells, preventing the clear distinction between Schwann cells and DSCs using these markers alone. Future studies should therefore aim to identify additional markers that specifically distinguish DSCs from Schwann cells. Alternatively, the inclusion of established Schwann cell-specific markers may allow these cells to be excluded during image analysis. Since mature melanocytes do not express NGFRp75, this marker was selected for the subsequent immunofluorescence stainings.

Optimization of CPD and NGFRp75 Immunofluorescence Co-Staining

The immunofluorescence staining protocol applied to UV-irradiated skin sections utilized the antibodies anti-CPD (TDM-2) and anti-NGFRp75. Prior to this study, the protocol had been established for the simultaneous detection of UV-induced DNA damage and the identification of DSCs [54]. As the original protocol exhibited several limitations, one objective of this study was to optimize the staining procedure. Optimization resulted in an adjusted primary antibody dilution, reducing antibody consumption while maintaining efficient and reproducible staining (Figure 15). In addition, an additional blocking step was incorporated into the protocol. The main limitation of the original staining protocol was the presence of an atypical CPD signal. Notably, CPD-positive signals were observed in the lower epidermis of both non-irradiated control skin samples and UV-irradiated skin samples (Figure 16). These signals were consistently confined to a distinct region and could readily be distinguished from genuine UV-induced CPDs based on their appearance and localization. This observation suggested the presence of nonspecific antibody binding despite the initial blocking step that was performed prior to primary antibody incubation. Based on experimental results, the secondary antibody could be excluded as the source of this background signal. To reduce this nonspecific binding, an additional blocking step was introduced immediately prior to incubation with the secondary antibody. This modification resulted in a lower CPD background. In a subsequent experiment, the dilution of the secondary antibody was additionally increased, however, this did not further reduce the nonspecific background staining. Therefore, only the additional blocking step was incorporated into the final staining protocol.

Detection and Repair of UV-Induced CPDs in NGFRp75-Positive Cells of Human Skin

UV-radiation represents one of the major environmental risk factors for the development of malignant melanoma. It primarily induces DNA damage in the form of CPDs, which are considered the most common UV-induced DNA lesions. The main objective of this study was to investigate whether DSCs, which are regarded as a potential precursor population for melanocytes, accumulate CPDs following UVA and UVB irradiation. Furthermore, the repair of these lesions was examined, as persistent DNA damage in DSCs may contribute to the accumulation of mutations and thereby increase the risk of malignant transformation. Anti-NGFRp75 was used as the primary marker for the iden-

tification of DSCs. The results demonstrate that NGFRp75-positive cells were consistently detected in all analyzed skin samples. In addition, CPD formation following UVA and UVB irradiation was successfully visualized, allowing the assessment of DNA damage and its repair in NGFRp75-positive cells.

For the investigation of UV-induced DNA damage in the form of CPDs, adult axillary skin, adult thigh skin, and juvenile foreskin were analyzed. Juvenile foreskin served as the primary experimental model because, as hairless skin, it contains extrafollicular DSCs, which are considered potential precursor cells of melanocytes. Furthermore, juvenile foreskin seems to contain substantially higher numbers of NGFRp75-positive cells than adult skin biopsies, most likely reflecting the age-dependent decline in both the number and functional capacity of stem cell populations previously observed [61]. Nevertheless, the inclusion of adult skin biopsies was essential, as adult skin has anatomical and structural characteristics that differ from juvenile tissue. The analysis of adult thigh and axillary skin allowed the comparison of UV-induced DNA damage between anatomically distinct skin sites with different epidermal thicknesses and tissue properties. The results show that both UVA and UVB irradiation induced CPD formation in skin cells. UVA (320 – 400 nm), owing to its longer wavelength, penetrates deeper into the skin than UVB (280 – 320 nm) and has been reported to reach the deep dermis, whereas UVB is generally considered to affect the epidermis and upper dermis [62]. The present results confirm that UVB-induced DNA damage also extends into the upper dermis (Figure 21 – 23). At time point T0, UVB-induced CPDs were detected throughout the epidermis and were additionally observed in cells located beneath the basement membrane. In contrast, despite its greater penetration depth, UVA-induced CPDs were mainly observed in the upper epidermis. These results are consistent with the known lower absorption efficiency of UVA by DNA. UVA induces CPDs considerably less efficiently than UVB, generating substantially lower levels of DNA damage in form of CPDs [44, 63]. Nevertheless, in axillary skin (Figure 18) and juvenile foreskin (Figure 20), magnified images also revealed some CPD signals within the upper dermis. Some NGFRp75-positive cells present in these regions showed distinct CPD-positive signals, indicating damaged DSCs. The UVB-induced CPD signals were stronger, due to the higher efficiency of UVB absorption by DNA and its greater capacity to induce CPD formation [44, 63]. No significant differences regarding the CPD staining were observed among the different skin biopsies. All UVB-irradiated samples showed strong CPD signals extending into the dermis (Figure 21 – 23), while the epidermis was almost entirely CPD-positive. The thigh skin biopsy had natural tissue folds that influenced the local UV dose by partially shielding areas of the epidermis from direct irradiation. This could explain the reduced CPD signal observed in some regions of the epidermis in the thigh skin biopsy. Since the CPD signal extended into the upper dermis, NGFRp75-positive cells located beneath the epidermis also showed distinct CPD staining, indicating that these cells sustained UVB-induced DNA damage. This was particularly evident in the magnified images. The visual detection of CPD-positive cells within the upper dermis suggests that all DSCs located in this region are exposed to the risk of acquiring UV-induced CPDs.

A further objective of this study was to examine the repair of CPDs after 24 and 48 hours. In all samples, CPD signals decreased over time, indicating successful activation of the NER pathway that is responsible for the removal of UV-induced DNA lesions [62]. Following UVA irradiation, most CPDs were repaired within 24 hours. The visible lesions in the upper epidermis appeared to be repaired more rapidly than the CPDs detected in the dermis. This was particularly evident in the axillary skin

(Figure 24B) and may indicate that keratinocytes repair UV-induced DNA damage more efficiently than cell populations located deeper within the skin. This is consistent with previous studies reporting cell-type-specific differences in the repair kinetics of UVB-induced CPDs [64, 65]. In cell cultures keratinocytes exhibit the highest DNA repair capacity, showing significantly faster CPD removal compared with other skin cell types such as melanocytes, fibroblasts, and DSCs [64]. After 48 hours, UVA-induced CPDs were barely detectable and could no longer be distinguished visually from the corresponding control samples (Figure 24B, 25B). Furthermore, CPD- and NGFRp75-double-positive cells, which were visible at T0, could not be reliably determined at later time points. To investigate the repair of DNA damage in NGFRp75-positive cells after UVA irradiation, more sensitive analytical approaches would be necessary. In contrast, UVB-irradiated skin tissues contained CPD-positive cells in both the epidermis and dermis at all examined time points up to T48. Although CPD signals decreased over time, indicating ongoing repair, CPD- and NGFRp75-double-positive cells remained detectable throughout the observed period (Figure 24C, arrow). These findings are of considerable relevance, as NGFRp75-positive cells are considered to represent DSC population,whose impairment may contribute to the initiation of MM [52]. In this context, reduced DNA repair capacity in these cells may allow the persistence and accumulation of mutagenic lesions, thereby promoting genomic instability and contributing to melanomagenesis.

A key limitation of this experimental model became evident in juvenile foreskin samples at T48 (data not shown). At this time point, the epidermis showed pronounced swelling and loss of structural integrity, indicating reduced tissue viability after prolonged incubation. In the corresponding T48 control CPD-positive staining was detected, raising concerns about the specificity and interpretability of the signal at this late time point. This observation indicates that extended incubation beyond 24 hours may introduce substantial confounding effects, including increased background staining and structural degradation, limiting the reliability of CPD assessment at later time points in this model.

An additional observation across several samples was NGFRp75-positive staining along the basement membrane (e.g. Figure 24B T0, T24; Figure 26C T0). Previous studies have reported p75NTR (NGFRp75) expression in a subset of basal keratinocytes involved in maintaining epidermal homeostasis, providing a plausible explanation for this staining pattern [66]. This finding has important implications for the interpretation of NGFRp75 as a marker for DSCs in human skin. Given their shared localization at or near the basement membrane, NGFRp75-positive basal keratinocytes may be difficult to distinguish from DSCs based on morphology and position alone, thereby posing a risk of misidentification. Consequently, reliance on NGFRp75 as a single marker may be insufficient for the specific identification of DSCs in situ. Future studies should consider incorporating additional markers or combinatorial staining approaches to improve cell-type discrimination and avoid confounding by basal keratinocyte populations.

In summary, the present study demonstrates that both UVA and UVB irradiation can induce CPD formation in NGFRp75-positive cells within an ex vivo human skin model. As NGFRp75 is a protein expressed by DSCs, a subset of the affected NGFRp75-positive cells may represent this cell population. DNA damage in DSCs may impair the regenerative capacity of the skin and, if not fully repaired, contribute to the accumulation of mutations. This is of particular relevance given the proposed role of DSCs as precursor cells of melanocytes and their potential involvement in melanoma development. The observed reduction in CPD signals at 24 and 48 hours indicates that DNA repair mechanisms

remain active following UV exposure. However, the persistence of CPDs at 48 hours suggests incomplete repair in a subset of cells, highlighting the need for extended observation periods to more accurately assess repair kinetics and completeness. At the same time, the limitations of the current experimental model must be considered. Prolonged incubation was associated with compromised tissue integrity and reduced staining reliability, which may complicate the interpretation of late time points. Future studies should therefore aim to optimize ex vivo culture conditions or complement this model with alternative approaches, such as advanced 3D skin models as described by Pavez Lorie and Boukamp [67], which could be further developed to include DSC populations. This could enable longer and more robust analyzes. Finally, the identification of DSCs based solely on NGFRp75 expression remains challenging. The validation of additional markers and the use of combinatorial staining strategies will be essential to improve the specificity of DSC detection and to more clearly define their role and niche within human skin.

Bibliography

[1] Lorenzo Cerroni et al., eds. *Histopathologie der Haut*. Berlin, Heidelberg: Springer Berlin Heidelberg, 2016, pp. 61–72. ISBN: 978-3-662-45132-8. DOI: 10.1007/978-3-662-45133-5.

[2] Seyed Jamaleddin Mostafavi Yazdi and Javad Baqersad. "Mechanical Modeling and Characterization of Human Skin: A Review". In: *Journal of Biomechanics* 130 (2022), p. 110864. ISSN: 0021-9290. DOI: 10.1016/j.jbiomech.2021.110864.

[3] Azar Nourian Dehkordi et al. "Skin Tissue Engineering: Wound Healing Based on Stem-Cell-Based Therapeutic Strategies". In: *Stem Cell Research & Therapy* 10.1 (2019), p. 111. ISSN: 1757-6512. DOI: 10.1186/s13287-019-1212-2.

[4] Helmut Hamm. "Grundlagen". In: *Basiswissen Dermatologie*. Ed. by Michael Goebeler and Helmut Hamm. Berlin, Heidelberg: Springer Berlin Heidelberg, 2017, pp. 3–15. ISBN: 978-3-662-52810-5. DOI: 10.1007/978-3-662-52811-2_1.

[5] Gerd Plewig et al., eds. *Braun-Falco's Dermatologie, Venerologie und Allergologie*. 7th ed. Berlin, Heidelberg: Springer Berlin Heidelberg, 2018, pp. 4–8. ISBN: 978-3-662-49544-5. DOI: 10.1007/978-3-662-49544-5.

[6] Mitchell F. Denning. "Epidermal Keratinocytes: Regulation of Multiple Cell Phenotypes by Multiple Protein Kinase C Isoforms". In: *The International Journal of Biochemistry & Cell Biology* 36.6 (2004), pp. 1141–1146. DOI: 10.1016/j.biocel.2003.12.005.

[7] Rutao Cui et al. "Central Role of p53 in the Suntan Response and Pathologic Hyperpigmentation". In: *Cell* 128.5 (2007), pp. 853–864. ISSN: 0092-8674. DOI: 10.1016/j.cell.2006.12.045.

[8] John D'Orazio et al. "UV Radiation and the Skin". In: *International Journal of Molecular Sciences* 14.6 (2013), pp. 12222–12248. ISSN: 1422-0067. DOI: 10.3390/ijms140612222.

[9] Kai-Lv Sun et al. "A Study of Normal Epidermal Melanocyte Distribution". In: *International Journal of Dermatology and Venereology* 4.1 (2021), pp. 32–35. DOI: 10.1097/JD9.0000000000000125.

[10] Mirosława Cichorek et al. "Skin Melanocytes: Biology and Development". In: *Advances in Dermatology and Allergology* 30.1 (2013), pp. 30–41. DOI: 10.5114/pdia.2013.33376.

[11] Devarati Mitra et al. "A UV-Independent Pathway to Melanoma Carcinogenesis in the Red Hair–Fair Skin Background". In: *Nature* 491.7424 (2012), pp. 449–453. DOI: 10.1038/nature11624.

[12] Marelize Snyman et al. "The metabolism of melanin synthesis—From melanocytes to melanoma". In: *Pigment Cell & Melanoma Research* 37.4 (2024), pp. 438–452. DOI: 10.1111/pcmr.13165.

[13] Maksim V. Plikus et al. "Fibroblasts: origins, definitions, and functions in health and disease". In: *Cell* 184.15 (2021), pp. 3852–3872. DOI: 10.1016/j.cell.2021.06.024.

[14] Richard O. Hynes and Alexandra Naba. “Overview of the Matrisome—An Inventory of Extracellular Matrix Constituents and Functions”. In: *Cold Spring Harbor Perspectives in Biology* 4.1 (2012), a004903. DOI: 10.1101/cshperspect.a004903.

[15] Manyam Ravikanth et al. “Heterogenecity of Fibroblasts”. In: *Journal of Oral and Maxillofacial Pathology* 15.2 (2011), pp. 247–250. DOI: 10.4103/0973-029X.84516.

[16] Joan Massagué. “TGFβce signalling in context”. In: *Nature Reviews Molecular Cell Biology* 13 (2012), pp. 616–630. DOI: 10.1038/nrm3434.

[17] C. H. Lim, Q. Sun, K. Ratti, et al. “Early Wnt signaling triggers anagen hair follicle regeneration after skin injury”. In: *Nature* 558 (2018), pp. 536–540. DOI: 10.1038/s41586-018-0242-x.

[18] Boris Hinz. “The myofibroblast: paradigm for a mechanically active cell”. In: *Journal of Biomechanics* 43.1 (2010), pp. 146–155. DOI: 10.1016/j.jbiomech.2009.09.020.

[19] Fanglong Wu et al. “Signaling pathways in cancer-associated fibroblasts and targeted therapy for cancer”. In: *Signal Transduction and Targeted Therapy* 6.1 (2021), p. 218. DOI: 10.1038/s41392-021-00641-0.

[20] Laure Rittié and Gary J. Fisher. “Natural and Sun-Induced Aging of Human Skin”. In: *Cold Spring Harbor Perspectives in Medicine* 5.1 (2015), a015370. DOI: 10.1101/cshperspect.a015370.

[21] Christos C. Zouboulis et al. “Human Skin Stem Cells and the Ageing Process”. In: *Experimental Gerontology* 68 (Aug. 2015), pp. 153–163. ISSN: 0531-5565. DOI: 10.1016/j.exger.2014.11.002.

[22] Kateri A. Moore and Ihor R. Lemischka. “Stem Cells and Their Niches”. In: *Science* 311.5769 (Mar. 2006), pp. 1880–1885. ISSN: 0036-8075. DOI: 10.1126/science.1110542.

[23] Thomas A. Rando. “Stem Cells, Ageing and the Quest for Immortality”. In: *Nature* 441.7097 (June 2006), pp. 1080–1086. ISSN: 0028-0836. DOI: 10.1038/nature04958.

[24] Xin Tang et al. “Epidermal Stem Cells: Skin Surveillance and Clinical Perspective”. In: *Frontiers in Cell and Developmental Biology* 10 (2022), p. 1030330. DOI: 10.3389/fcell.2022.1030330.

[25] Colin A. B. Jahoda et al. “Hair follicle dermal cells differentiate into adipogenic and osteogenic lineages”. In: *Nature* 423 (2003), pp. 1017–1021. DOI: 10.1038/nature01750.

[26] Jean G. Toma et al. “Isolation and characterization of multipotent skin-derived precursors from human skin”. In: *Stem Cells* 23.5 (2005), pp. 727–737. DOI: 10.1634/stemcells.2004-0134.

[27] Christin Starzonek et al. “Enrichment of Human Dermal Stem Cells from Primary Cell Cultures through the Elimination of Fibroblasts”. In: *Cells* 12.6 (2023), p. 949. ISSN: 2073-4409. DOI: 10.3390/cells12060949. URL: https://doi.org/10.3390/cells12060949.

[28] Ling Li, Mizuho Fukunaga-Kalabis, and Meenhard Herlyn. “Isolation, Characterization, and Differentiation of Human Multipotent Dermal Stem Cells”. In: *Human Embryonic Stem Cell Protocols*. Ed. by Kursad Turksen. Vol. 584. Methods in Molecular Biology. Totowa, NJ: Humana Press, 2010, pp. 63–77. DOI: 10.1007/978-1-60761-369-5_5.

[29] Ling Li et al. “Human dermal stem cells differentiate into functional epidermal melanocytes”. In: *Journal of Cell Science* 123.6 (2010), pp. 853–860. DOI: 10.1242/jcs.061598.

[30] Wenru Pan et al. “Characterization of p75 Neurotrophin Receptor Expression in Human Dental Pulp Stem Cells”. In: *International Journal of Molecular Sciences* 17.7 (2016), p. 1079. DOI: 10.3390/ijms17071079. URL: https://doi.org/10.3390/ijms17071079.

[31] Aurora Bernal and Lorena Arranz. “Nestin-expressing progenitor cells: function, identity and therapeutic implications”. In: *Cellular and Molecular Life Sciences* 75.12 (2018), pp. 2177–2195. ISSN: 1420-9071. DOI: 10.1007/s00018-018-2794-z. URL: https://doi.org/10.1007/s00018-018-2794-z.

[32] Veronique Pingault et al. “SOX10: 20 years of phenotypic plurality and current understanding of its developmental function”. In: *Journal of Medical Genetics* 59.2 (2022), pp. 105–114. DOI: 10.1136/jmedgenet-2021-108105.

[33] Heiko Locher et al. “TUBB3: Neuronal Marker or Melanocyte Mimic?” In: *Cell Transplantation* 23.4-5 (2014), pp. 675–691. DOI: 10.3727/096368913X674099.

[34] Yasuhiro Matsumura and Honnavara N. Ananthaswamy. “Toxic effects of ultraviolet radiation on the skin”. In: *Toxicology and Applied Pharmacology* 195.3 (2004), pp. 298–308. DOI: 10.1016/j.taap.2003.08.019.

[35] Carolyn J. Heckman et al. “Minimal Erythema Dose (MED) testing”. In: *Journal of Visualized Experiments* 75 (2013), e50175. DOI: 10.3791/50175.

[36] Marcelo de Paula Corrêa. “Solar ultraviolet radiation: properties, characteristics and amounts observed in Brazil and South America”. In: *Anais Brasileiros de Dermatologia* 90.3 (2015), pp. 297–313. DOI: 10.1590/abd1806-4841.20154089.

[37] International Agency for Research on Cancer (IARC). *IARC Monographs Hazard Classification*. World Health Organization. June 16, 2023. URL: https://www.iarc.who.int/infographics/iarc-monographs-classification/ (visited on 07/17/2026).

[38] The Skin Cancer Foundation. *UV-Strahlung*. The Skin Cancer Foundation. 2026. URL: https://www.skincancer.org/de/risk-factors/uv-radiation/ (visited on 07/17/2026).

[39] Oana Gag et al. “UVA/UVB Irradiation Exerts a Distinct Phototoxic Effect on Human Keratinocytes Compared to Human Malignant Melanoma Cells”. In: *Life* 13.5 (2023), p. 1144. DOI: 10.3390/life13051144.

[40] Brian L. Diffey. “Sources and measurement of ultraviolet radiation”. In: *Methods* 28.1 (2002), pp. 4–13. DOI: 10.1016/S1046-2023(02)00204-9.

[41] Louise Finlayson et al. “Depth Penetration of Light into Skin as a Function of Wavelength from 200 to 1000 nm”. In: *Photochemistry and Photobiology* 98.4 (2022), pp. 974–981. DOI: 10.1111/php.13550. URL: https://doi.org/10.1111/php.13550.

[42] Martina Hyeraci et al. “Systemic Photoprotection in Melanoma and Non-Melanoma Skin Cancer”. In: *Biomolecules* 13.7 (2023), p. 1067. ISSN: 2218-273X. DOI: 10.3390/biom13071067. URL: https://doi.org/10.3390/biom13071067.

[43] Gerd P. Pfeifer and Ahmad Besaratinia. “UV wavelength-dependent DNA damage and human non-melanoma and melanoma skin cancer”. In: *Photochemical & Photobiological Sciences* 11.1 (2012), pp. 90–97. DOI: 10.1039/C1PP05144J.

[44] Jean Cadet and Thierry Douki. “Formation of UV-induced DNA damage contributing to skin cancer development”. In: *Photochemical & Photobiological Sciences* 17 (2018), pp. 1816–1841. DOI: 10.1039/C7PP00395A.

[45] Nimrat Chatterjee and Graham C. Walker. “Mechanisms of DNA damage, repair, and mutagenesis”. In: *Environmental and Molecular Mutagenesis* 58.5 (2017), pp. 235–263. DOI: 10.1002/em.22087. URL: https://doi.org/10.1002/em.22087.

[46] S. Premi et al. “Chemiexcitation of Melanin Derivatives Induces DNA Photoproducts Long after UV Exposure”. In: *Science* 347.6224 (2015), pp. 842–847. DOI: 10.1126/science.1256022.

[47] Thierry Nouspikel. “DNA repair in mammalian cells: Nucleotide excision repair: variations on versatility”. In: *Cellular and Molecular Life Sciences* 66.6 (2009), pp. 994–1009. DOI: 10.1007/s00018-009-8737-y.

[48] Chih-Hung Lee et al. “Molecular Mechanisms of UV-Induced Apoptosis and Its Effects on Skin Residential Cells: The Implication in UV-Based Phototherapy”. In: *International Journal of Molecular Sciences* 14.3 (2013), pp. 6414–6435. DOI: 10.3390/ijms14036414.

[49] Bart Tummers and Douglas R. Green. “Caspase-8: regulating life and death”. In: *Immunological Reviews* 277.1 (2017), pp. 76–89. DOI: 10.1111/imr.12541.

[50] Dagmar Kulms and Thomas Schwarz. “Molecular mechanisms of UV-induced apoptosis”. In: *Photodermatology, Photoimmunology & Photomedicine* 16.5 (2000), pp. 195–201. DOI: 10.1034/j.1600-0781.2000.160501.x.

[51] International Agency for Research on Cancer. *Global Cancer Observatory: Non-melanoma Skin Cancer Fact Sheet*. Lyon, France, 2022. URL: https://gco.iarc.who.int/media/globocan/factsheets/cancers/17-non-melanoma-skin-cancer-fact-sheet.pdf (visited on 07/21/2026).

[52] James D. Hoerter et al. “Extrafollicular Dermal Melanocyte Stem Cells and Melanoma”. In: *Stem Cells International* 2012 (2012), p. 407079. DOI: 10.1155/2012/407079. URL: https://doi.org/10.1155/2012/407079.

[53] B. Plitta-Michalak et al. “Development and characterisation of an irradiation device for biomedical studies covering the solar spectrum with individual regulated spectral bands”. In: *Photochemical & Photobiological Sciences* 21.9 (2022), pp. 1701–1717. DOI: 10.1007/s43630-022-00252-w.

[54] Zireen Haj Abdo. “UV-induzierte DNA-Schäden und deren Reparatur in verschiedenen Hautzelltypen: Eine immunfluoreszenzbasierte Analyse von Hautbiopsien”. Bachelorarbeit. Hochschule für angewandte Wissenschaften Hamburg, 2025.

[55] Christopher J. Cold and John R. Taylor. “The Prepuce”. In: *BJU International* 83.Suppl. 1 (1999), pp. 34–44. DOI: 10.1046/j.1464-410x.1999.0830s1034.x.

[56] Kristján R. Jessen, Rhona Mirsky, and Alison C. Lloyd. “Schwann Cells: Development and Role in Nerve Repair”. In: *Cold Spring Harbor Perspectives in Biology* 7.7 (2015), a020487. DOI: 10.1101/cshperspect.a020487.

[57] Angela M. Montero and Alice H. Huang. “The Regenerative Capacity of Neonatal Tissues”. In: *Development* 149.12 (2022), dev199819. DOI: 10.1242/dev.199819.

[58] Kangkang Zha et al. “Nerve Growth Factor (NGF) and NGF Receptors in Mesenchymal Stem/Stromal Cells: Impact on Potential Therapies”. In: *Stem Cells Translational Medicine* 10.7 (2021), pp. 1008–1020. ISSN: 2157-6564. DOI: 10.1002/sctm.20-0290.

[59] Carlo Zancanaro et al. “Immunohistochemical evidence suggests intrinsic regulatory activity of human eccrine sweat glands”. In: *Journal of Anatomy* 194.3 (1999), pp. 433–444. DOI: 10.1046/j.1469-7580.1999.19430433.x.

[60] Katarzyna Nowogrodzka and Alina Jankowska-Konsur. “Emerging biomarker in carcinogenesis. Focus on Nestin”. In: *Advances in Dermatology and Allergology/Postępy Dermatologii i Alergologii* 39.6 (2022), pp. 1001–1007. DOI: 10.5114/ada.2022.122599.

[61] Alla Zorina et al. “Age-Related Changes in the Fibroblastic Differon of the Dermis: Role in Skin Aging”. In: *International Journal of Molecular Sciences* 23.11 (2022), p. 6135. DOI: 10.3390/ijms23116135.

[62] Sienny Muliaty Sumali. “A comparative study of UVA and UVB radiation: Mechanisms of DNA damage and repair”. In: *Indonesia Journal of Biomedical Science* 17.2 (2023), pp. 239–243. DOI: 10.15562/ijbs.v17i2.485.

[63] Stéphane Mouret et al. “Cyclobutane pyrimidine dimers are predominant DNA lesions in whole human skin exposed to UVA radiation”. In: *Proceedings of the National Academy of Sciences of the United States of America* 103.37 (2006), pp. 13765–13770. DOI: 10.1073/pnas.0604213103.

[64] Mouna Mhamdi-Ghodbani et al. “UVB damage response of dermal stem cells as melanocyte precursors compared to keratinocytes, melanocytes, and fibroblasts from human foreskin”. In: *Journal of Photochemistry and Photobiology B: Biology* 220 (2021), p. 112216. DOI: 10.1016/j.jphotobiol.2021.112216.

[65] Mariarosaria D’Errico et al. “Cell type and DNA damage specific response of human skin cells to environmental agents”. In: *Mutation Research/Fundamental and Molecular Mechanisms of Mutagenesis* 614.1–2 (2007), pp. 37–47. DOI: 10.1016/j.mrfmmm.2006.06.009.

[66] Francesca Truzzi et al. “p75 neurotrophin receptor mediates apoptosis in transit-amplifying cells and its overexpression restores cell death in psoriatic keratinocytes”. In: *Cell Death & Differentiation* 18.6 (2011), pp. 948–958. ISSN: 1476-5403. DOI: 10.1038/cdd.2010.162.

[67] Elizabeth Pavez Lorie and Petra Boukamp. “Cell-derived Matrices”. In: *Methods in Cell Biology*. Ed. by Francesco Pampaloni and Ernst H. K. Stelzer. Vol. 148. Academic Press, 2019, pp. 309–323. DOI: 10.1016/bs.mcb.2019.04.003.

Danksagung

Zunächst möchte ich mich bei Dr. Beate Volkmer und Dr. Rüdiger Greinert bedanken, die mir die Möglichkeit gegeben haben, den praktischen Teil meiner Masterarbeit in ihrem Labor durchzuführen und Teil ihres großartigen Teams zu werden. Für ihre Unterstützung, ihr Vertrauen und den wertvollen fachlichen Austausch während der gesamten Bearbeitungszeit bin ich ihnen dankbar. Mein weiterer Dank gilt Herrn Prof. Dr. Julien Béthune für die Übernahme der Betreuung und Begutachtung dieser Masterarbeit. Ein ganz besonderer Dank gilt meiner Betreuerin Dr. Mouna Mhamdi-Ghodbani, die mich während der gesamten Arbeit mit großem Engagement begleitet hat. Für ihre intensive Betreuung, ihre wertvollen Anregungen sowie ihre stets hilfsbereite Unterstützung möchte ich mich herzlich bedanken.

Ebenfalls möchte ich mich herzlich bei Dr. Sarah Degenhardt für den wissenschaftlichen Austausch und ihre große Unterstützung und die investierte Zeit in die Korrektur dieser Arbeit bedanken. Weiterhin gilt mein Dank Stefan Henning, Dr. I-Peng Chen und Dr. Marc Bender für ihre wertvollen Anmerkungen, konstruktiven Rückmeldungen und den wissenschaftlichen Austausch. Mein besonderer Dank gilt außerdem Huda Jama, die mich jeden Tag durch ihr Fachwissen und ihre hilfsbereite Art, sowohl im Labor als auch außerhalb unterstützt hat. Ebenson bedanke ich mich sehr bei Stefanie Balk, Rebecca Keck und Nadja Rogall für ihre stete fachliche und organisatoriche Unterstützung im Laboralltag.

Außerdem möchte ich mich herzlich bei meinen Freunden bedanken, die mich während dieser Zeit stets begleitet haben, immer ein offenes Ohr für mich hatten und mich jederzeit unterstützt haben. Abschließend gilt mein tiefster Dank meiner Familie für ihre bedingungslose Liebe, ihre Geduld und ihre stete Unterstützung über all die Jahre. Ohne sie wäre dieser Weg nicht möglich gewesen

Declaration on Oath / Eidesstaatliche Versicherung

I hereby declare that this thesis has been composed by me and is based on my own work, unless stated otherwise. All references and verbatim extracts have been quoted, and all sources of information have been specifically acknowledged. This work has not been submitted in the same or a similar version to any other examination board before.

Ich versichere hiermit, dass ich die vorliegende Masterarbeit eigenständig und ohne fremde Hilfe selbständig verfasst und nur die angegebenen Quellen und Hilfsmittel verwendet habe. Wörtlich oder dem Sinn nach aus anderen Werken entnommene Stellen sind unter Angabe der Quellen kenntlich gemacht. Ich versichere weiterhin, dass ich die Arbeit vorher nicht in einem anderen Prüfungsverfahren eingereicht habe.

Hamburg, July 28, 2026



Vivien Rerich